



รายงานวิจัยฉบับสมบูรณ์

โครงการ การก่อเกิดเฟสและการตรวจวิเคราะห์ผง γ-Al₂O₃ โดยการเผาผง nano-Boehmite ด้วยความร้อน

โดย รุ่งนภา ทิพากรฐิติกุล

กรกฎาคม 2552

สัญญาเลขที่ MRG5080038

รายงานวิจัยฉบับสมบูรณ์

โครงการ การก่อเกิดเฟสและการตรวจวิเคราะห์ผง γ -Al $_2$ O $_3$ โดยการเผาผง Nano-Boehmite ด้วย ความร้อน

รุ่งนภา ทิพากรฐิติกุล

มหาวิทยาลัยอุบลราชธานี

สนับสนุนโดยสำนักงานกองทุนสนับสนุนการวิจัย

(ความเห็นในรายงานนี้เป็นของผู้วิจัย สกว.ไม่จำเป็นต้องเห็นด้วยเสมอไป)

Abstract

Aluminium hydrate, Al(OOH), or boehmite was synthesized using AlN₃O₉,9H₂O and Na₂Al₂O₄ as the starting materials by the precipitation method. The obtained boehmite powders were in crystalline form with various crystallite sizes depending on pH of the solutions which were in range 8-11. Selected boehmite precursor with different crystallite sizes were subjected to heat treatment process as to produce γ -Al₂O₃. The investigation show that phase transformation from boehmite to γ -Al₂O₃ was readily occurred at temperature as low as 350°C. Increasing treatment temperature to about 750°C, other transitive alumina such as θ -Al₂O₃ were also found while transform to α -Al₂O₃ were found at 1000 °C. Crystallite sizes of the obtained α -Al₂O₃ increased with increasing treatment temperature and also dependent on crystallite size of boehmite precursor. Morphological studies with SEM and TEM revealed that a strong agglomeration were found for both boehmite and its relative α -Al₂O₃ phases. Appropriate α -Al₂O₃ characteristic is obtained by considering characteristic of used boehmite precursor and condition applied during heat treatment process.

บทคัดย่อ

อลูมิเนียมไฮเดรต หรือ โบฮิไมท์ (AIOOH) สังเคราะห์ชี้นด้วยวิธีการตกตะกอน โดยใช้ $AIN_3O_9.9H_2O$ และ $Na_2AI_2O_4$ เป็นสารตั้งต้น ผงผลึกโบฮิไมท์ที่เตรียมได้มีขนาดอนุภาค แตกต่างกัน ขนาดอนุภาคนี้ขึ้นอยู่กับตามเงื่อนไขค่าความเป็นกรด-ด่าง ซึ่งทำการเปลี่ยนค่า ความเป็นกรด-ด่างอยู่ในย่าน 8-11 จากนั้นเลือกผงผลึกโบฮิไมท์ที่มีขนาดอนุภาคแตกต่าง กันทำการเผาแคลไซน์เพื่อให้ก่อเกิดเฟสของ $\gamma-AI_2O_3$ พบว่าการเปลี่ยนเฟสจากผงผลึกโบฮิ ไมท์เป็น $\gamma-AI_2O_3$ เกิดขึ้นที่อุณหภูมิ 350 องศาเซลเซียส ซึ่งถือว่าเป็นอุณหภูมิที่ต่ำมาก เมื่อ ทำการพิ่มอุณหภูมิสูงขึ้นถึง 750 และ 1000 องศาเซลเซียส ผงโบฮิไมท์เปลี่ยนเฟสเป็น $\theta-AI_2O_3$ และ $\alpha-AI_2O_3$ ตามลำดับ จากนั้นนำพีคผลการตรวจวิเคราะห์ด้วยเทคนิค XRD มา คำนวณหาขนาดอนุภาคพบว่าขนาดอนุภาคของ $\alpha-AI_2O_3$ เพิ่มขึ้นตามอุณหภูมิในการผาแคล ไซน์ที่เพิ่มขึ้นและยังขึ้นกับขนาดอนุภาคผลึกผงโบฮิไมท์เมื่อตอนเริ่มต้น สำหรับสัญฐาน วิทยาของผงที่เตรียมได้ทั้ง ผงโบฮิไมท์และผง $\alpha-AI_2O_3$ ตรวจวิเคราะห์ด้วยเทคนิค SEM และ TEM พบว่าอนุภาคผงเกาะกันอย่างหนาแน่น ดังนั้นสรุปได้ว่าลักษณะเฉพาะของผง $\alpha-AI_2O_3$ ที่เตรียมได้นั้นขึ้นกับลักษณะเฉพาะของผง $\alpha-AI_2O_3$

Project Code: MRG5080038

(รหัสโครงการ)

Project Title : การก่อเกิดเฟสและการตรวจวิเคราะห์ผง γ -Al $_2O_3$ โดยการเผาผง nano-Boehmite ด้วย

ความร้อน

(ชื่อโครงการ)

Investigator : รุ่งนภา ทิพากรฐิติกุล มหาวิทยาลัยอุบลราชธานี

(ชื่อนักวิจัย)

E-mail Address : rungnapa@rocketmail.com

Project Period : 2 ปี (1 ธันวาคม 2549 – 1 ธันวาคม 2551)

(ระยะเวลาโครงการ)

Executive Summary

โครงการนี้มีวัตถุประสงค์เพื่อเตรียมผง γ -Al $_2$ O $_3$ จากผง Boehmite ขนาดนาโนเมตร ด้วย เทคนิคการตกตะกอนโดยปรับเงื่อนใขการเตรียมเช่น ค่า pH และอุณหภูมิ เพื่อให้ได้ขนาดอนุภาคผง Boehmite ที่เหมาะสม พร้อมทั้งศึกษาอิทธิพลของขนาดอนุภาคของ Boehmite ต่อการเกิดเฟสผง γ -Al $_2$ O $_3$ ซึ่งเป็นสารตั้งต้นของการเตรียมผง Na β'' -Al $_2$ O $_3$ ต่อไป

โครงการนี้ได้เริ่มต้นจากกาเตรียมผง Boehmite ด้วยวิธีการตกตะกอน ซึ่งทำการควบกุม อุณหภูมิตั้งแต่ 40-80 องศาเซลเซียส และค่า pH 7-11 จากผลการทดลองพบว่า ณ อุณหภูมิ 40 องศา เซลเซียสทุกเงื่อนไขค่า pH ไม่พบการเกิดเฟสของ Boehmite แต่จะก่อเกิดเฟสของ NaNO3 แทนทั้งหมด เมื่อเพิ่มอุณหภูมิขึ้นเป็น 60 และ 80 องศาเซลเซียสพบว่าสามารถตกตะกอนผง Boehmite ได้เกือบทุก เงื่อนไขของค่า pH ยกเว้นที่อุณหภูมิ 60 องศาเซลเซียส และค่า pH11 เท่านั้น ซึ่งพบการปะปนของเฟส Al(OH)3 จากผลการทดลอง XRD ของทุกเงื่อนไขที่สามารถตกตะกอนผง Boehmite ได้พบว่าลักษณะ พีคมีขนาดพีคกว้างซึ่งสามารถบ่งชี้ Crystallite size ซึ่งสามารถใช้สมการ Scherrer เพื่อคำนวณขนาด ผลึกได้ พบว่ามีขนาดอยู่ในย่านนาโนเมตร ตั้งแต่ 2.4 – 3.9 นาโนเมตร และยืนยันขนาดผลึกที่เล็กมากนี้ จากภาพถ่าย TEM

จากนั้นนำผง Boehmite ที่เตรียมได้ทดสอบการเปลี่ยนแปลงทางความร้อนด้วยเทคนิค TG/DTA และ FTIR พบว่ามีการเปลี่ยนแปลงทางความร้อนเกิดขึ้นอย่างชัดเจนที่อุณหภูมิ 100 350 1000 และ 1150 องศาเซลเซียส จากช่วงอุณหภูมิดังกล่าวจะเป็นย่านอุณหภูมิในการเผาแคลไซน์ผง Boehmite โดยเริ่มต้นที่อุณหภูมิ 350-1100 องศาเซลเซียส จากผลการตรวจวิเคราะห์ด้วยเทคนิค XRD พบว่า ช่วง อุณหภูมิ 350-1000 องศาเซลเซียส ก่อเกิดเฟส γ -Al $_2$ O $_3$ ที่มีขนาดผลึกตั้งแต่ 3.0-5.3 นาโนเมตร และการ ตรวจวิเคราะห์ด้วยเทคนิค TEM

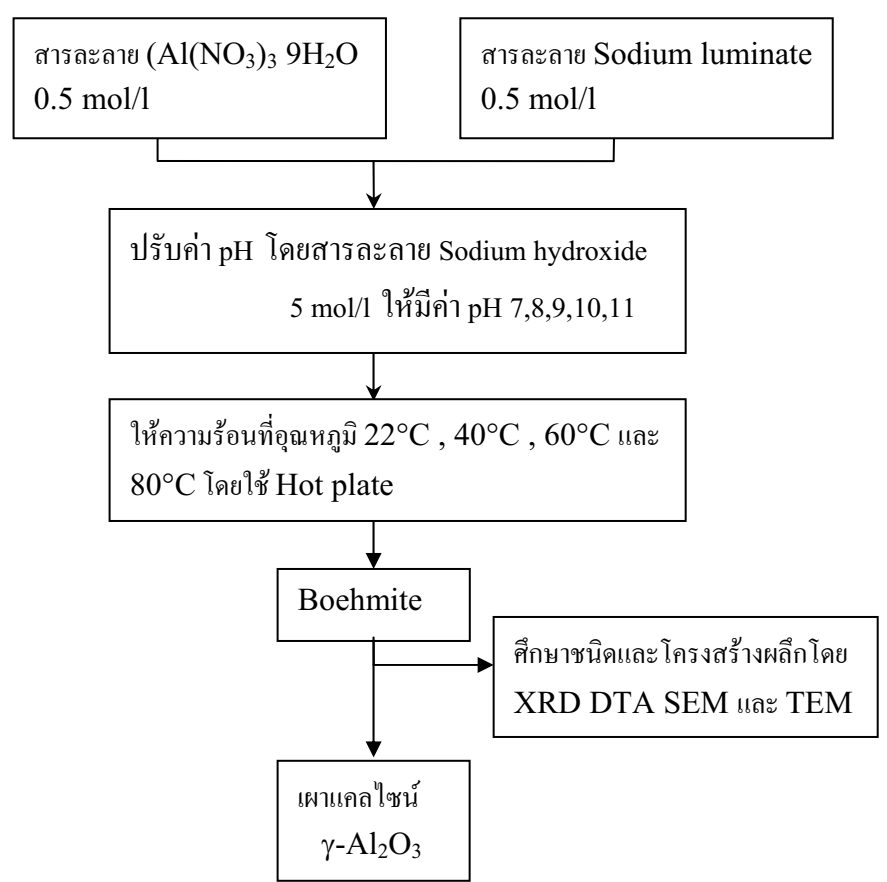
Keywords : Boehmite, Synthesis, Characterization and Beta-alumina (คำหลัก)

วัตถุประสงค์

1. เพื่อพัฒนากระบวนการเตรียมผง Boehmite โดยการหาเงื่อนไขการเผาแคลไซน์ และขนาดอนุภาคที่ เหมาะสมในการผลิตเฟสเคี่ยวของผง γ –Al $_{_1}$ O $_{_2}$

วิธีการทดลอง

สามารถเตรียมด้วยวิธีการตกตะกอน โดยการนำ Aluminium nitrate nanohydrate ((Al(NO₃)₃·9H₂O) ละลายในน้ำกลั่นให้มีความเข้มข้น 0.5 mol/l และ Sodium aluminate ละลายในน้ำ กลั่นให้มีความเข้มข้น 0.5 mol/l และ Sodium hydroxide (NaOH) ละลายในน้ำกลั่นให้มีความเข้มข้น 5 mol/l จากนั้นนำสารละลาย Aluminium nitrate nanohydrat ผสมกับสารละลาย Sodium aluminate และ ปรับค่า pH ของสารละลายดังกล่าวด้วย สารละลาย Sodium hydroxide ให้มีค่า pH 8 pH 9 pH 10 และ pH 11 โดยตรวจวัดค่า pH ด้วย pH meter จากนั้นให้ความร้อนแก่สารละลายผสมที่อุณหภูมิ 20 °C 40 °C 60 °C และ 80 °C เป็นเวลา 20 ชั่วโมง บันทึกการตกตะกอนของสารละลายผสม นำสารที่ ตกตะกอนล้างด้วยน้ำกลั่นจำนวน 5 ครั้ง และ ล้างด้วยเอททานอลจำนวน 1 ครั้ง นำสารละลายผสมเข้า เครื่อง Centrifuge เพื่อแยกชั้นของน้ำออกจากตกตะกอน นำสารละลายผสมอบในเตาอบที่อุณหภูมิ 60 °C เป็นเวลา 24 ชั่วโมง เพื่อกำจัดความชื้นออกจากตะกอน



รูปที่ 1 ขั้นตอนและกระบวนการเตรียมผง Boehmite และ γ -Al $_2$ O $_3$

ผลการเตรียมผง Boehmite

ผงที่ได้จากการตกตะกอนของสารละลาย Aluminium nitrate nanohydrate กับ Sodium aluminate ตาม เงื่อนไขของอุณหภูมิ และค่า pH ผ่านการตรวจวิเคราะห์ด้วยเทคนิค XRD ดังรูปที่ 2 ผลปรากฏว่าเกิด เฟสต่าง ๆ มากมาย สำหรับเฟส Boehmite เกิดขึ้นได้หลายเงื่อนไข ณ เงื่อนไขการตกตะกอนที่ 40 °C ค่า pH = 8-11 พบเฟสหลักของเกลือ NaNO3 ที่สอดคล้องกับ JCPDS หมายเลข 36-1474 ซึ่งมีโครงสร้าง rhombohedral ใน space group R3c(167) และหายไปเมื่ออุณหภูมิเริ่มสูงขึ้น ตั้งแต่ 60 °C เป็นต้นไป (ดัง รูปที่ 2(b)) ณ อุณหภูมิสูงกว่า 60 °C พบเฟสหลักของ boehmite (γ -AlOOH) ที่สอดคล้องกับ JCPDS หมายเลข 21-1307 ซึ่งมีโครงสร้าง rhombohedral ใน space group Amam(63) เมื่อค่า pH สูงขึ้นจาก 10-11 เฟส γ -AlOOH เปลี่ยนกลับเป็นเฟส Al(OH)3 เมื่อเพิ่มอุณหภูมิสูงขึ้นเป็น 80 °C เฟส γ -AlOOH ตกตะกอนในช่วง pH 8 ถึง 11 ดังรูปที่ 2(c) จากการวิเคราะห์ผลการทดลองสามารถอธิบายปฏิกิริยาเคมีได้ 2 แนวทาง ดังนี้

$$Al(NO3)3.9H2O+Na2Al2O4+NaOH \rightarrow 3NaNO3 + 3AlOOH + 8H2O$$
 (1)

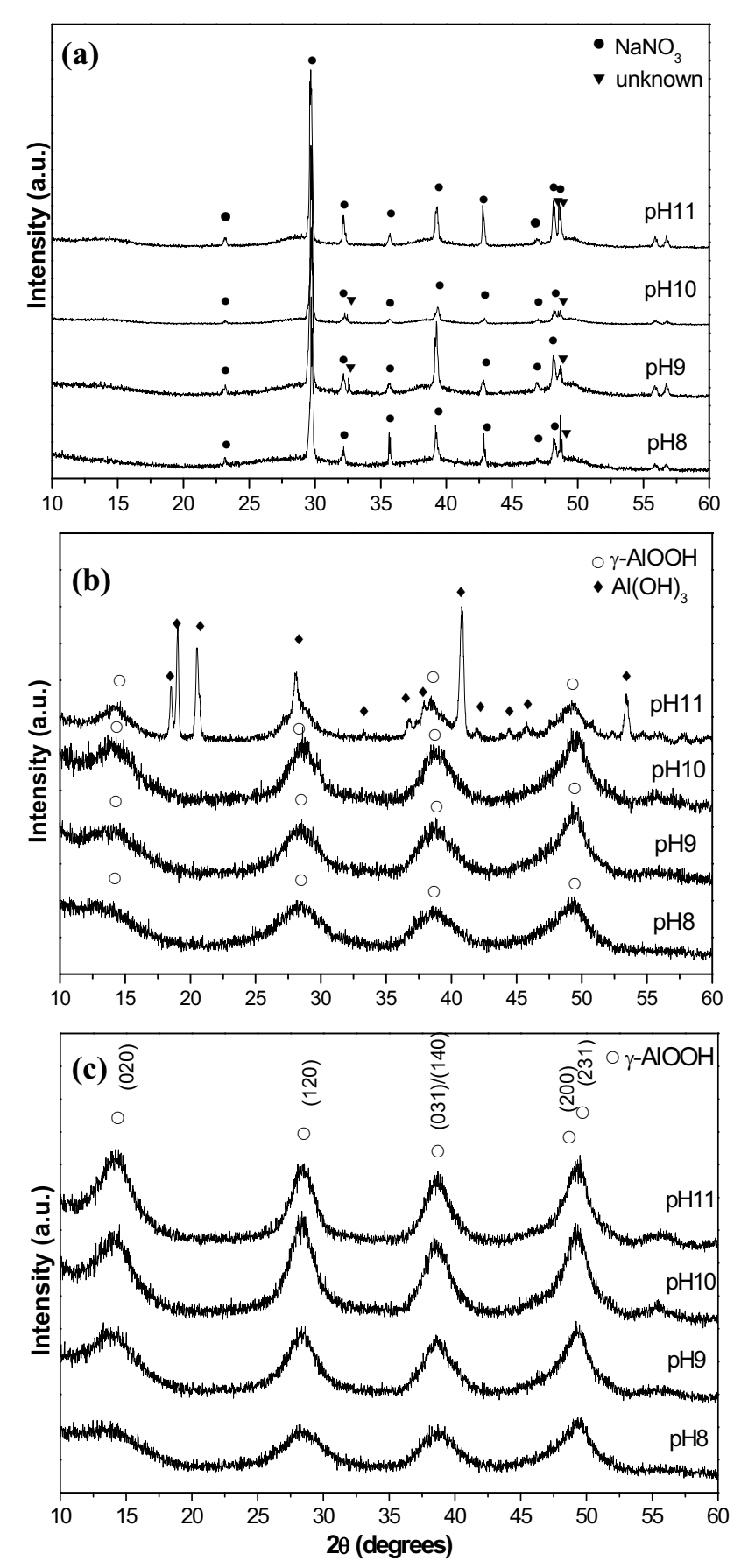
$$Al(NO_3)_3.9H_2O+Na_2Al_2O_4+NaOH \rightarrow AlOOH + 2Al(OH)_3 + 3NaNO_3 + 6H_2O$$
 (2)

จากพีก XRD สามารถคำนวณหาค่าขนาดผลึกเฉลี่ยได้จากความกว้างของพีกระนาบ (020) แสดงข้อมูล ในตารางที่ 1 พร้อมทั้งค่าร้อยละ โดยปริมาณของเฟส boehmite

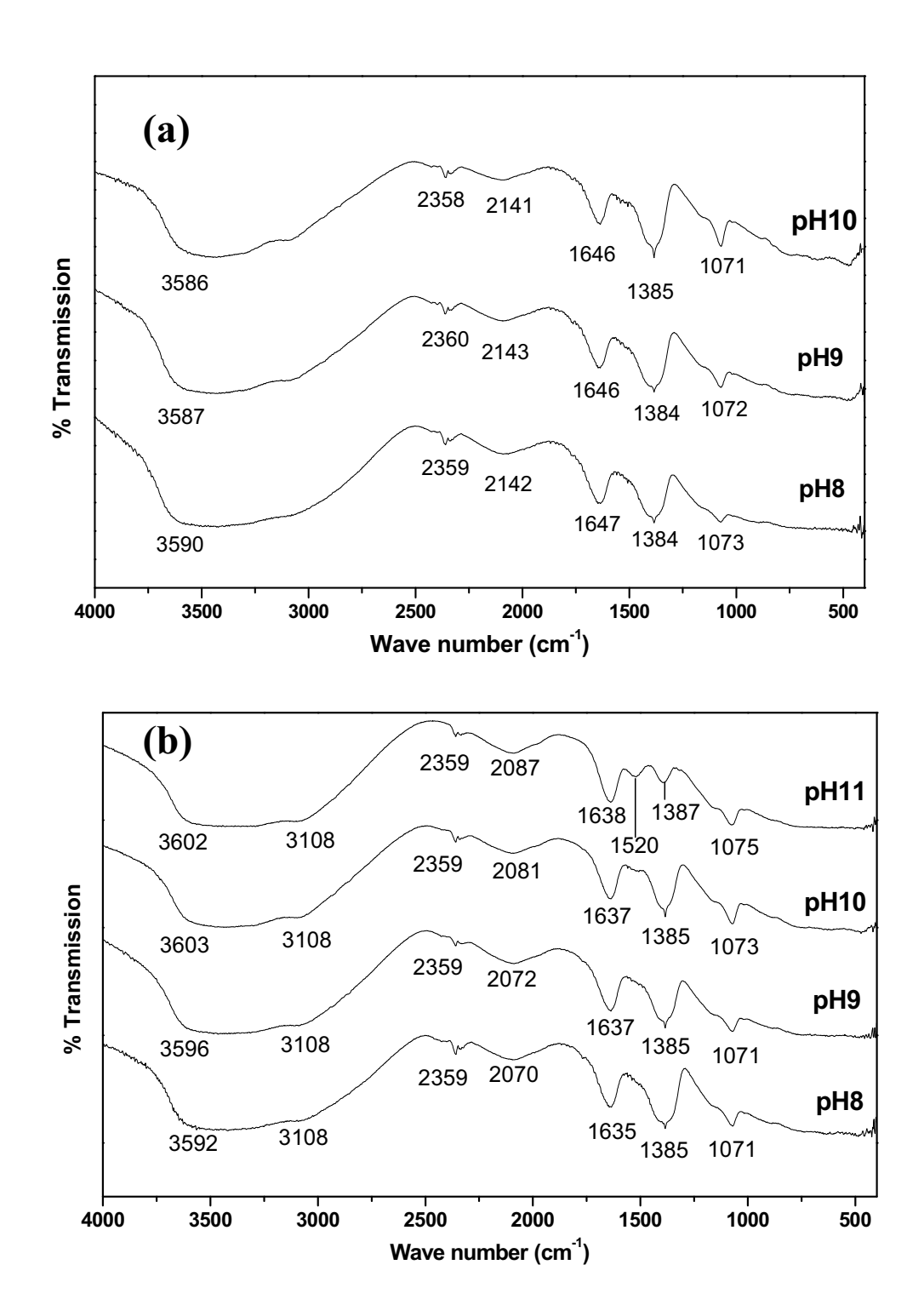
จากผลการทดลอง FT-IR ของผง boehmite ตกตะกอนที่อุณหภูมิ 60 และ 80 °C โดยมีการ ปรับเปลี่ยนค่า pH สรุปได้ดังรูปที่ 3 ผล FT-IR ของทุกค่า pH ณ อุณหภูมิ 60 °C แสดงดังรูปที่ 3 ผนบว่าตำแหน่งพืกที่ 2359, 1646, 1385 และ 1072 cm และมีบางพืกกว้างกว่าปกติที่ตำแหน่ง 2387 และ 2142 cm ตามลำดับ นอกจากนั้นแล้วยังพบพืกเล็ก ๆ ที่ตำแหน่ง 1160 และ 480 cm ผลการทดลองนี้ เมื่อเปรียบเทียบกับผลการทดลองของ Musić et. al. [12] อธิบายว่า พืกของผง boehmite ปรากฏที่ ตำแหน่ง 1075 และ 1153 cm ซึ่งเป็นตำแหน่งพันธะระหว่าง Al-OH เกิดการสั่น ซึ่งมีนักวิจัยท่านอื่น ให้ความเห็นว่า ความถี่การสั่นของหมู่ OH ควรอยู่ที่ 3278 และ 3084 cm สำหรับผลึกของเฟส pseudoboehmite จะแสดงพืกที่มีลักษณะฐานกว้างที่ตำแหน่ง 3460 cm ใ

ตารางที่ 1 ปริมาณเฟส Boehmite โดยน้ำหนัก (wt.%) และ ขนาดอนุภาคผง Boehmite (nm) ที่เตรียมได้ จากเงื่อนไขของ pH และ อุณหภูมิที่แตกต่างกัน

Precipitation conditions		Average Crystallite size (nm)	% Boehmite	Phase present
Temperature(°C)	рН	-		
40	7	-	-	NaNO ₃
40	8	-	-	NaNO ₃
40	9	-	74.59	$NaNO_3$, γ - $AlO(OH)$
40	10	-	64.89	$NaNO_3$, γ - $AlO(OH)$
40	11	-	67.89	$NaNO_3$, γ - $AlO(OH)$
60	7	-	61.57	γ -AlO(OH), Al(OH) ₃
60	8	2.5	74.09	γ -AlO(OH), Al(OH) ₃
60	9	2.7	100.00	γ-AlO(OH)
60	10	3.8	100.00	γ-AlO(OH)
60	11	-	87.16	γ -AlO(OH), Al(OH) ₃
80	7	-	73.32	γ-AlO(OH), Al(OH),
80	8	2.4	80.71	γ -AlO(OH), Al(OH) ₃
80	9	3.3	100.00	γ-AlO(OH)
80	10	3.7	100.00	· γ-AlO(OH)
80	11	3.9	100.00	· γ-AlO(OH)



รูปที่ 2 รูปแบบการเลี้ยวแบนรังสีเอ็กซ์ของผง boehmite ที่เงื่อนไขอุณหภูมิ (a) 40 (b) 60 และ (c) 80 $^{\circ}$ C

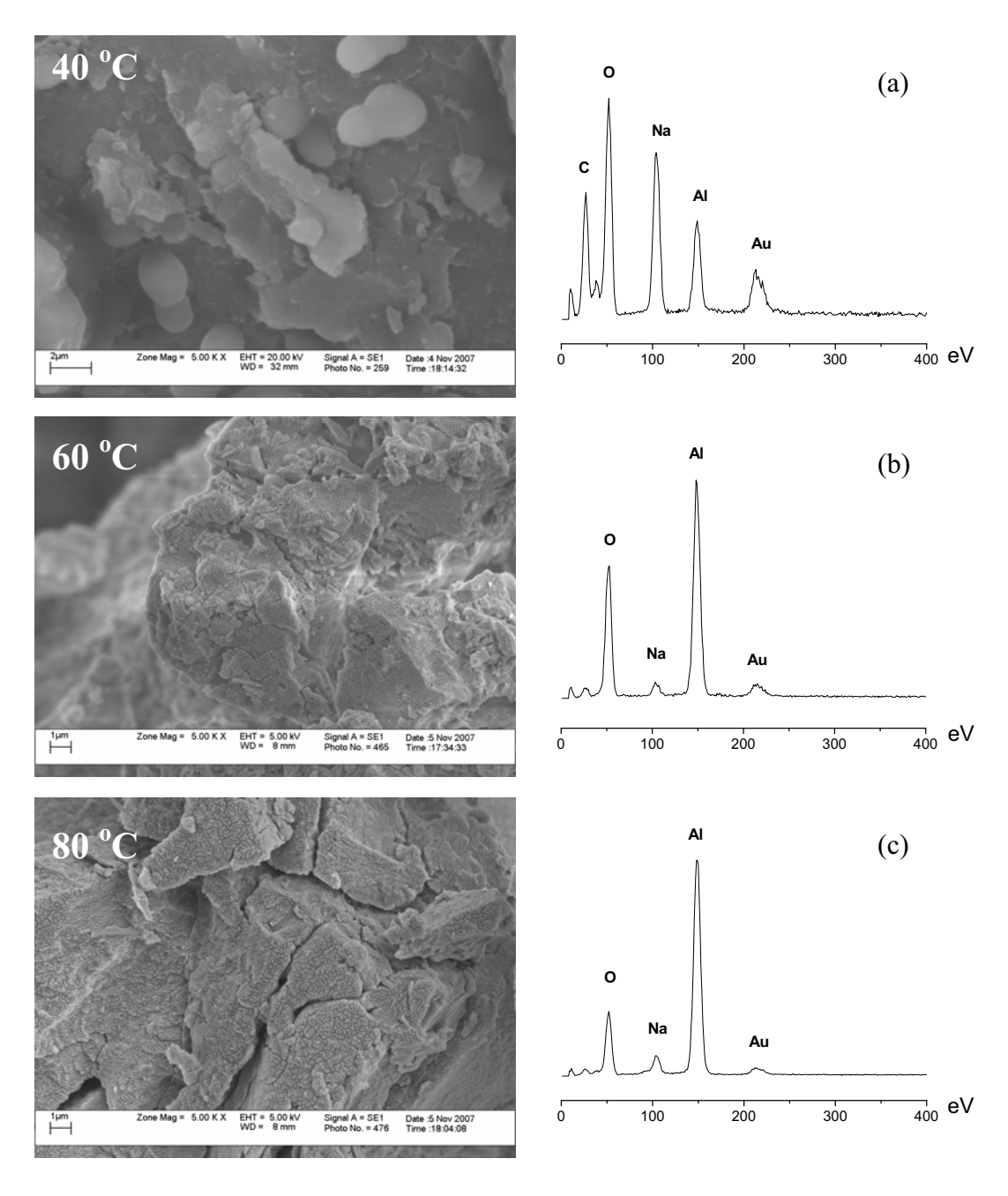


รูปที่ 3 FTIR ของผง boehmite ตกตะกอนที่เงื่อนไขอุณหภูมิ (a) 60 และ (b) 80 $^{\circ}$ C

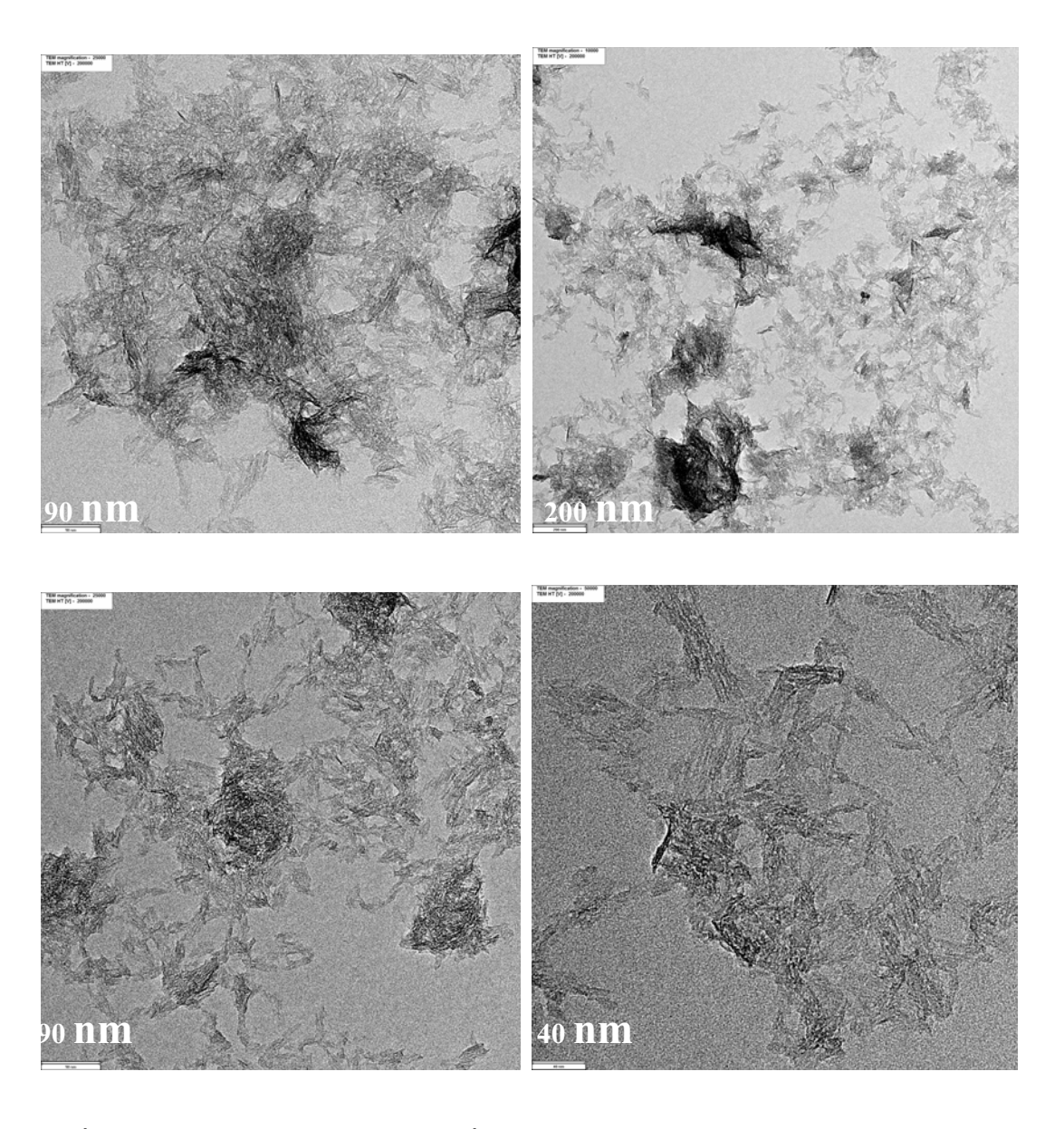
สัญฐานวิทยาของผงที่ตกตะกอนได้ถูกตรวจวิเคราะห์ด้วยกล้องอิเล็กตรอนแบบส่องกราด (SEM) โดยนำเอาผงที่เตรียมได้จากเงื่อนไข pH เดียวกัน (pH = 8) แต่อุณหภูมิต่างกัน ดังแสดงในรูปที่ 4 ผงที่ตกตะกอนที่อุณหภูมิ 40 $^{\circ}$ C อนุภาค NaNO $_{3}$ มีขนาดใหญ่ ซึ่งยืนยันผลการทดลองจากการตรวจ วิเคราะห์ด้วยเทคนิค XRD นอกจากนั้นแล้วจากภาพถ่ายที่ 4(a) แสดงลักษณะผลึกของ NaNO $_{3}$ ที่ดีทั้ง ขนาดอนุภาคและรูปร่างอนุภาคผง ทั้งยืนยันได้จากผลการตรวจวิเคราะห์ด้วยเทคนิค EDX ซึ่งมี

องค์ประกอบของ Na เป็นปริมาณมาก เมื่ออุณหภูมิสูงขึ้นเป็น 60 °C เริ่มก่อเกิดเฟสของ boehmite เห็น ได้ว่ามีการเกาะกลุ่มของผงขนาดนา โนเมตร และการเกาะกันเป็นกลุ่มนี้พบที่ผงตกตะกอนที่ 80 °C ด้วย ผลทั้งสองอย่างข้างต้นยืนยันด้วยการตรวจวิเคราะห์ด้วยเทคนิค EDX พบว่ามีปริมาณ Na ลดลง

ลักษณะสัญฐานวิทยาของผงที่เตรียมได้พบว่าในแต่ละเงื่อนไขไม่แตกต่างกันมากนักและยังให้ อนุภาคผง boehmite ขนาดนาโนเมตร มีการจัดเรียงตัวแบบสุ่ม อย่างไรก็ตามขนาดของผลึกผงมีขนาดที่ แตกต่างกันตามเงื่อนไขของการเตรียม ซึ่งได้รับการยืนยันจากรายงานวิจัยของ Hochepied et al [14] และ Shen et al [15]



รูปที่ 4 SEM แสดงสัญฐานวิทยาของผง boehmite ตกตะกอนที่อุณหภูมิต่างกัน พร้อมทั้งผล EDX



รูปที่ 5 TEM ของผง boehmite ตกตะกอนที่อุณหภูมิ 80 $^{\circ}$ C และค่า pH = 8

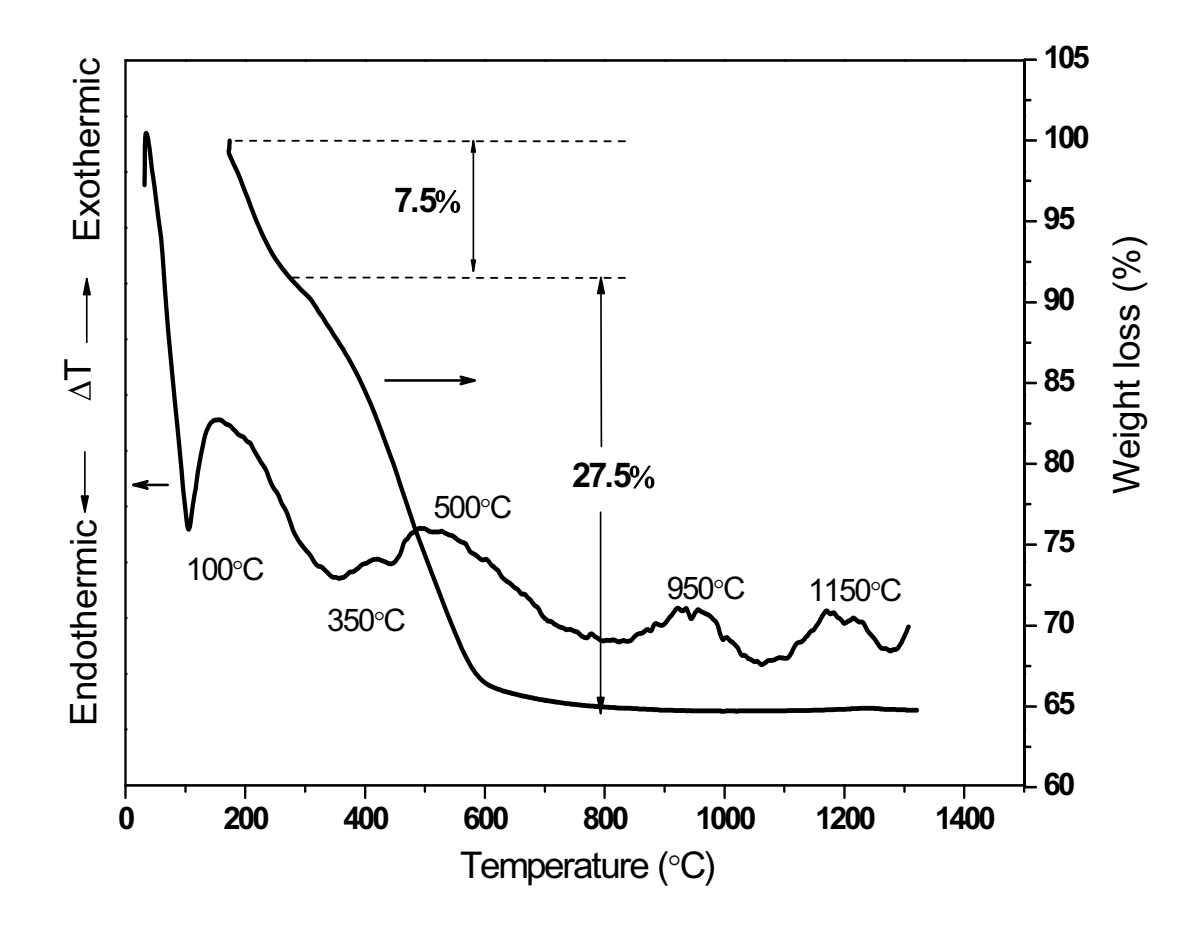
ผลการตรวจวิเคราะห์ผงที่เตรียมได้ด้วยเทคนิค TEM ดังแสดงในรูปที่ 5 พบว่าผลึกผง boehmite มีขนาดเล็กมาก น้อยกว่า 10 นาโนเมตร ต่อกันจนมีรูปร่างคล้ายเส้นใย อย่างไรก็ตามเส้นใยนี้ มีลักษณะเป็นเส้นสั้นๆ มีความหนาไม่สม่ำเสนอ และเกาะกันจนดูคล้ายว่าเป็นแผ่น

ผลการเตรียมผง γ-Al₂O₃ จากการเผาแคลใชน์ผง boehmite

พฤติกรรมการเปลี่ยนแปลงทางความร้อนของผง boehmite ตรวจวิเคราะห์ด้วยเทคนิค TG/DTA ดังรูปที่ 6 พบว่ามีพีค endothermic peak จากการสูญเสียน้ำหนักมวลสารจากผลการทดลองด้วย TGA ที่ อุณหภูมิประมาณ 250 350 และ 500 °C endothermic peak แรก ที่อุณหภูมิ 250 °C เป็นการระเหยไป

ของน้ำและเอลกอฮอล์ เมื่ออุณหภูมิสูงขึ้น ณ อุณหภูมิ 350 °C อาจเป็นการสลายตัวของหมู่ Hydroxyl สุดท้ายที่อุณหภูมิ 500 °C เป็นการเกิดผลึกของ alumina หรือการแปรสภาพของสารอินทรีย์ที่ได้จาก การสลายของหมู่ Hydroxyl ซึ่งจะเห็นได้ว่า น้ำหนักที่สูญเสียไปนั้นรวมร้อยละ 35 ของน้ำหนักเริ่มต้น โดยเฉพาะในขั้นตอนสุดท้ายที่สูญเสียน้ำหนักไปถึงร้อยละ 34.62 ของน้ำหนักเริ่มต้น ซึ่งส่วนใหญ่เกิด จากการเปลี่ยนโครงสร้างผลึกจาก bayerite เป็น γ -Al $_2$ O $_3$ ซึ่งควรจะเป็นดังสมการที่ (3)

$$2Al(OH)_3 \rightarrow Al_2O_3 + 3H_2O$$
 (3)



รูปที่ 6 TGA และ DTA ของผง boehmite

อย่างไรก็ตาม ในช่วงแรกที่มีการสูญเสียร้อยละโดยน้ำหนักประมาณ 7.5 นั้น ร้อยละ 10 อาจ เกิดจากการเผาใหม้ส่วนประกอบอื่น ๆ ที่ปะปนมาพร้อมกับกระบวนการ ball milling และอีกประมาณ ร้อยละ 17.5 ณ อุณหภูมิ $500~^{\circ}$ C เกิดขึ้นจากกระบวนการก่อเกิดเฟสของ γ -Al $_2$ O $_3$ เนื่องจากการ เปลี่ยนแปลงองค์ประกอบทางเคมีของ boehmite ซึ่งทำให้เกิดการสูญเสียร้อยละโดยน้ำหนักถึง 15 ดัง ปฏิกิริยาเคมีต่อไปนี้

Alooh
$$\rightarrow \gamma$$
-Al₂O₃ + H₂O (4)

เมื่อเปรียบเทียบระหว่างค่าการสูญเสียร้อยละ โดยน้ำหนักกับผลการทดลองสามารถอธิบายได้ดังนี้ ในช่วงแรกสารที่เตรียมได้มีการคูดซับน้ำและเอทธานอล จากนั้นเมื่ออุณหภุมิ 80 °C กลับพบว่าเฟส AI(OH), หายไป

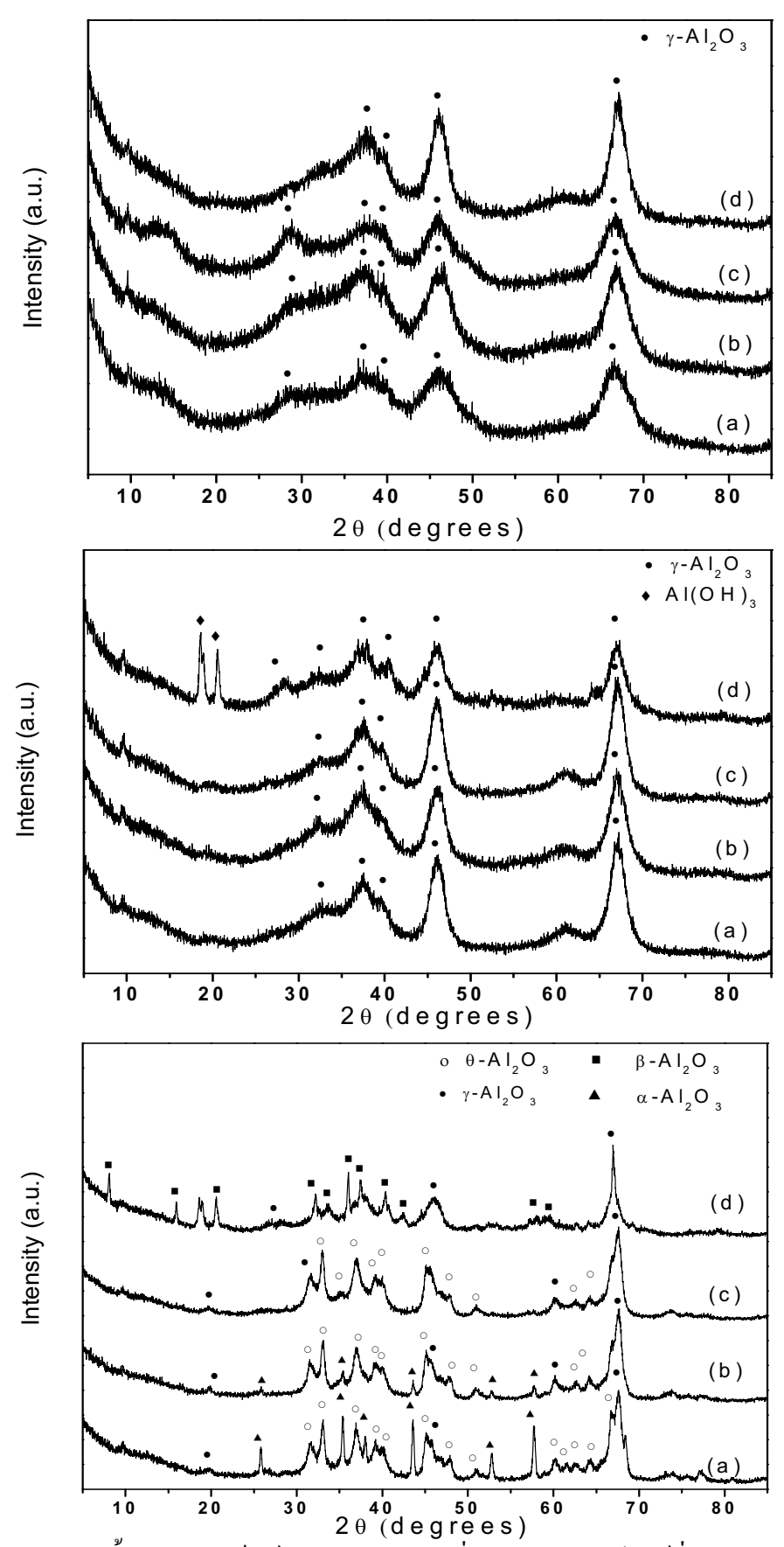
ผลการตรวจวิเคราะห์ผง boehmite ที่ผ่านการเผาแคลไซน์เพื่อก่อให้เกิดเฟส γ -Al $_2$ O $_3$ เริ่มต้นที่ อุณหภูมิ 350 $^{\circ}$ C เริ่มเกิดการเปลี่ยนแปลงเฟสที่อุณหภูมิ 500 $^{\circ}$ C ซึ่งสอดคล้องกับผลการตรวจวิเคราะห์ การเปลี่ยนแปลงทางความร้อน สังเกตุพบว่าขนาดผลึกของ γ -Al $_2$ O $_3$ เพื่อขนาดขึ้นเมื่อใช้ขนาดผลึกผง boehmite เพิ่มขึ้น ซึ่งทำให้เห็นความสัมพันธ์อย่างชัดเจนและสอดคล้องกับผลการทดลองของ Okada et al [11] จากรายงานการวิจัยของ Sharma et al [16] พบว่าในช่วงอุณหภูมิระหว่าง 700-1000 $^{\circ}$ C สังเกต พบการเปลี่ยนเฟสของผงอลูมิน่าเป็นลำดับดังนี้

Boehmite
$$\rightarrow \gamma \rightarrow \delta \rightarrow \theta \rightarrow \alpha\text{-Al}_2O_3$$

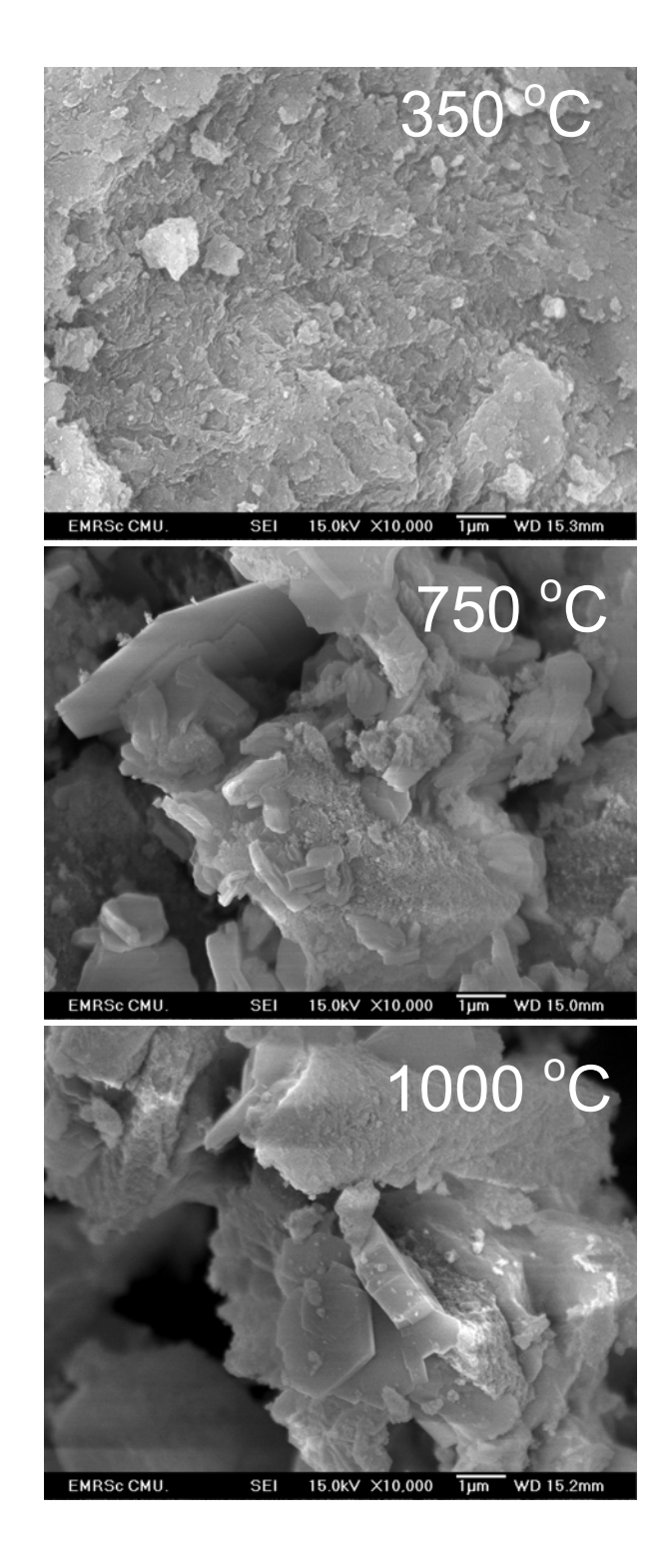
สำหรับเฟส δ -Al $_2$ O $_3$ ตรวจไม่พบอาจเนื่องจากช่วงอุณหภูมิที่ใช้ในการเผาแคลไซน์ไม่ เหมาะสมสำหรับการเกิดเฟสนี้ ดังนั้นสรุปได้ว่าเฟสหลักที่พบที่อุณหภูมิ 1000° C เป็นเฟส θ -Al $_2$ O $_3$ และมีลำดับการเปลี่ยนแปลงเฟสดังต่อไปนี้

Boehmite
$$o heta o lpha o eta$$
-Al $_2$ O $_3$ ตามลำดับ

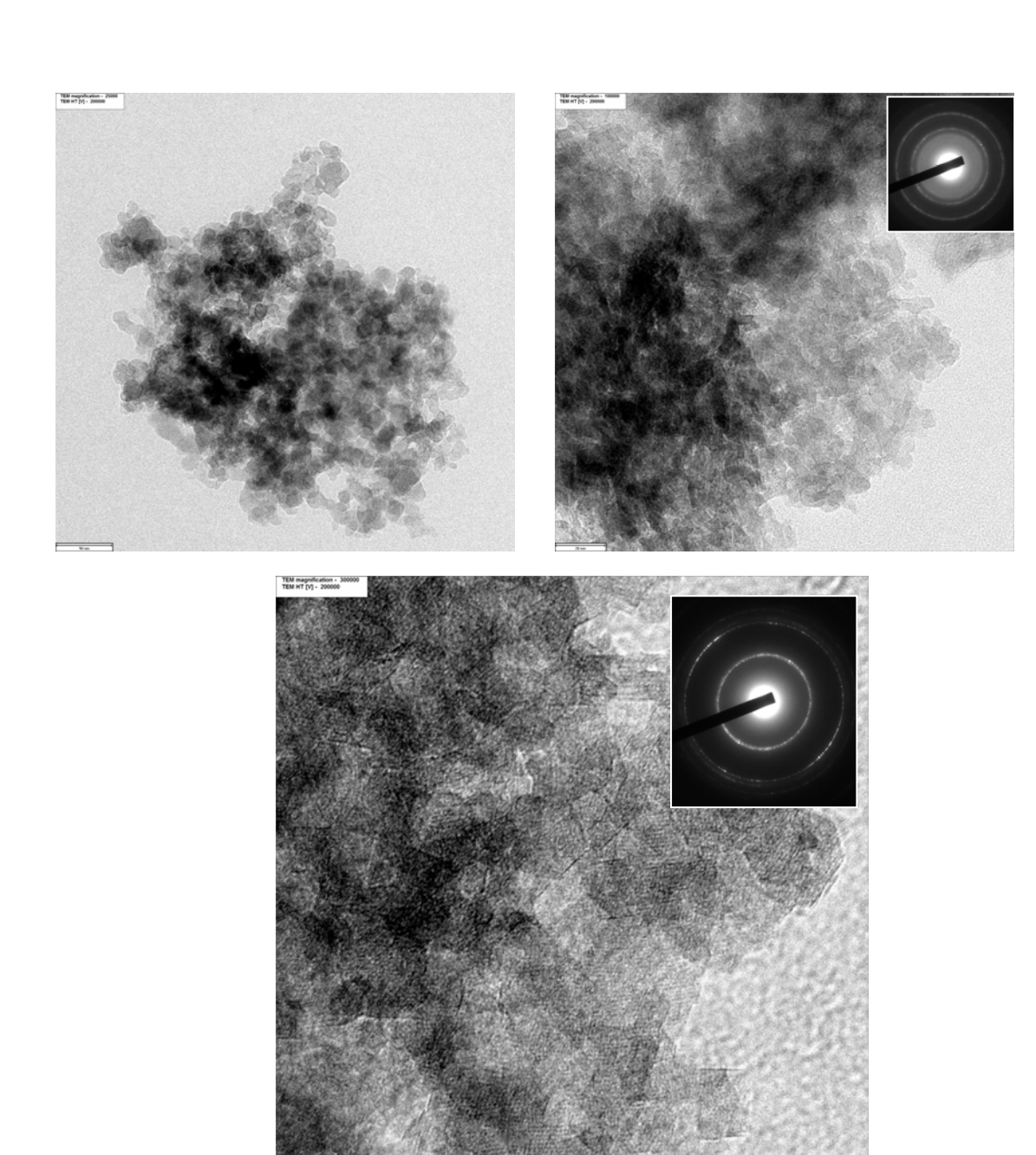
การก่อเกิดเฟส γ -Al $_2$ O $_3$ ภายใต้การเผาผง boehmite นี้ทำให้เกิดการก่อตัวของรูพรุนใหม่ [17] เนื่องจาก อนุภาคผงของ γ -Al $_2$ O $_3$ มีขนาดเล็กระดับ ไมครอนและเกาะกลุ่มกันคล้ายกับอนุภาคผง boehmite แต่จากผลการทดลองเปรียบเทียบกับผลการเตรียม γ -Al $_2$ O $_3$ จากวิธีการอื่นแล้ว ซึ่งรายงาน โดย Okada et al. พบว่ากล ใกการเปลี่ยนเฟสที่กล่าวข้างต้นนั้นเชื่อว่ามาจากการตรวจวิเคราะห์ โดยเฉพาะการตรวจวิเคราะห์รูพรุน ซึ่งอธิบายโดย Hwang et al [17] ผลของการทดลองนี้บ่งชี้ให้เห็น ความสัมพันธ์ระหว่างผง γ -Al $_2$ O $_3$ ที่ได้จากการเริ่มต้นเตรียมผง boehmite ตัวอย่างเช่น ขนาดผลึก γ -Al $_2$ O $_3$ ที่ได้นั้นขึ้นกับการเลือกขนาดผง boehmite เมื่อเริ่มต้น อีกนัยหนึ่งอาจบอกว่า การเลือกเงื่อนใข การเตรียมผง boehmite ส่งผลถงลักษณะเฉพาะและสมบัติของผง γ -Al $_2$ O $_3$ ที่เตรียมได้



รูปที่ 7 รูปแบบการเลี้ยวเบนรังสีเอ็กซ์ของผง boehmite ที่ผ่านการเผาแคล ใชน์ที่อุณหภูมิ (a) 350 (b) 750 และ (c) $1000\,^{\circ}\mathrm{C}$



รูปที่ 8 สัญฐานวิทยาของผง boehmite ขนาดผลึก 2.4 นาโนเมตร ที่ผ่านการเผาแคล ใชน์ที่อุณหภูมิ (a) 350 (b) 750 และ (c) 1000 $^{\circ}$ C



รูปที่ 9 TEM ของผง γ -Al $_2$ O $_3$ จากการเผาผง boehmite ที่อุณหภูมิ 750 $^{\circ}$ C

ตารางที่ 2 ขนาดผลึก boehmite เงื่อนไขการเผาแคลไซน์ สัมพันธ์กับขนาดผลึกของผง γ-Al₂O₃

Crystallite size of	Calcination	Crystallite size	Phase present
Boehmite (nm)	temperature (°C)	of γ-Al ₂ O ₃ (nm)	
2.4	350	2.8	γ-Al ₂ O ₃
	750	4.8	γ -Al ₂ O ₃
	1000	-	θ -Al ₂ O ₃ , α -Al ₂ O ₃ and
			γ -Al ₂ O ₃
2.7	350	3.2	γ-Al ₂ O ₃
	750	4.4	γ -Al ₂ O ₃
	1000		γ -Al ₂ O ₃
3.3	350	2.6	γ-Al ₂ O ₃
	750	4.8	γ -Al ₂ O ₃
	1000	-	$\theta\text{-}Al_2O_3$ and $\gamma\text{-}Al_2O_3$
3.9	350	3.8	γ-Al ₂ O ₃ and NaNO3
	750	4.4	γ -Al ₂ O ₃ and Al(OH)3
	1000	-	β -Al ₂ O ₃ and γ -Al ₂ O ₃

สรุปผลการทดลอง

ในการทดลองนี้เราได้แสดงให้เห็นถึงการเตรียมผง boehmite ขนาดเล็กระดับนาโน โดยวิธีการ ตกตะกอน ซึ่งเริ่มต้นจากสารตั้งต้นอย่างง่าย ความสัมพันธ์ระหว่างขนาดผลึกผง boehmite และเงื่อนไข การเตรียมเป็นปัจจัยควบคุมขนาดผลึกจากการปรับค่า pH และอุณหภูมิ ผง boehmite ที่เตรียมได้ ตกตะกอนและเกาะกันเป็นกลุ่มเนื่องจากอนุภาคมีขนาดเล็กมาก นอกจากนั้นแล้วเมื่อนำผง boehmite ผ่านการเผาแคลไซน์ที่เงื่อนไขของอุณหภูมิและเวลาที่แตกต่างกัน ทำให้ได้ผง γ -Al $_2$ O $_3$ ที่มีขนาดผลึก ในย่านนาโนเมตรที่แตกต่างกันด้วย ดังนั้นเพื่อให้ได้ผง γ -Al $_2$ O $_3$ ที่มีขนาดเล็ก ควรเผาแคลไซน์ที่ อุณหภูมิไม่เกิน 750 $^{\circ}$ C

Output จากโครงการวิจัยที่ได้รับทุนจาก สกว.

- P. Pimsorn, R. Tipakonthitikul, A. Niyompan, N. Kanchanarat and T. Tunkasiri, Preparation of Nano-crystalline Boehmite as a Gamma-Alumina Source for the Production of Na.Beta-Al₂O₃ Solid Electrolyte. *Advanced Materials Research*, 55-57 (2008) 653-656.
- 2. **R. Tipakontitikul**, A. Niyompan and T. Tunkasiri, Formation and characterization of γ-alumina obtained via heat treatment of nano-boehmite precursor (2009) (submitted in Materials Chemistry and Physics)
- 3. **R. Tipakontitikul**, A. Niyompan, K. Srisurat, N. Kanchanarat and T. Tunkasiri, Effect of pH on Phase Formation and Morphology of the Nanocrystalline Boehmite Powder Prepared by A Precipitation Method. *Journal of Microscopy Society of Thailand*, **22** (2008) 20-22.

ภาคผนวก

Preparation of Nano-Crystalline Boehmite as a Gamma-alumina Source for the Production of Na.beta-Al₂O₃ Solid Electrolyte

P. Pimsorn¹, R. Tipakonthitikul^{1, a}, A. Niyompan^{1, b}, N. Kanchanarat ² and T. Tunkasiri ³

Keywords: boehmite, precipitation, beta-alumina, preparation and characterization

Abstract. Nano-crystalline boehmite (AlOOH) proposed as a precursor for γ -Al₂O₃ production was prepared using precipitation process. The mixture of two starting solutions of AlN₃O₉.9H₂O and Na₂Al₂O₄ was formed and NaOH was used as pH adjustment. Various preparation conditions, starting pH and temperatures were applied. The results suggested that high purity AlOOH powder could be obtained at solution temperature above 60°C and starting pH was in range 7-11. Their crystalline size increased from 2.4 to 3.9 nm with increasing pH. According to the results, AlOOH from pH 8 and temperature 80°C was selected for producing the γ-Al₂O₃ by calcination in the temperature range of 350°C-1100°C. Transformation from AlO(OH) to γ-Al₂O₃ could be readily observed from the whole temperature range and γ-Al₂O₃ crystalline size was increased with increasing calcination temperature. After the temperature reached 1100°C, transformation to α- and θ- phases were also found. Morphology of γ-Al₂O₃ powder shows a strong aggomeration.

Introduction

Boehmite (γ-AlOOH) is widely used as a precursor for producing γ-Al₂O₃ one of the technological importance substance for several applications. Using γ -Al₂O₃ as a starting material in production of mechanical parts, refractors, insulator or even solid electrolyte has been known for a several decades [1] and it has been know that morphology and crystalline size of the γ-Al₂O₃ are very much sensitive to characteristic of boehmite [2]. The structure of boehmite consists of Al(OOH)₆ octahedral layers and it crystalinity is known to be related to preparation condition [3]. Generally, boehmite of lower crystalinity is named pseudoboehmite. However, there is no significant structural difference between these two forms of the boemite [4]. Since boehmite is prepared from liquid phase by precipitation or hydrothermal method, experimental conditions such as the aluminium source, precipitant, solution pH, temperature, aging and drying conditions are thought to influence the crystalline size of the boehmite product [5]. The γ -Al₂O₃ obtained in this work is used as a raw material for produce the Na.β"-Al₂O₃ solid electrolyte which is an important part of battery technology. Since the final product of Na.β"-Al₂O₃ is also depended on crystalline size and morphology of γ-Al₂O₃. Thus, in order to obtain desired Na.β"-Al₂O₃, selection of γ-Al₂O₃ crystalline size and morphology has to be taken into account and these are controlled by boehmite preparation condition.

The main goal of the present study is to investigate the effect of pH solution and temperature on phase formation, crystalline size and morphology of boehmite. The investigation will be extended to that of resulting calcined γ -Al₂O₃. In this study, boehtmite and γ -Al₂O₃ phase formations are determined using XRD technique with CuK α radiation. Line broadenings of XRD peaks are also



¹ Department of Physics, Faculty of Science, Ubonratchathani University, Ubonratchathani 34190, Thailand.

² National Metal and Materials Technology Center, 114 Thailand Science Park, Pathumthani 12120, Thailand

³Department of Physics, Faculty of Science, Chiang Mai University, Chiang Mai 50200, Thailand ^arungnapa@rocketmail.com, ^banuson@rocketmail.com

used for crystalline size determination. Finally, the powder morphology is studied by SEM. Then the effect of pH solution on characteristics of boehmite and γ -Al₂O₃ are discussed.

Experimental

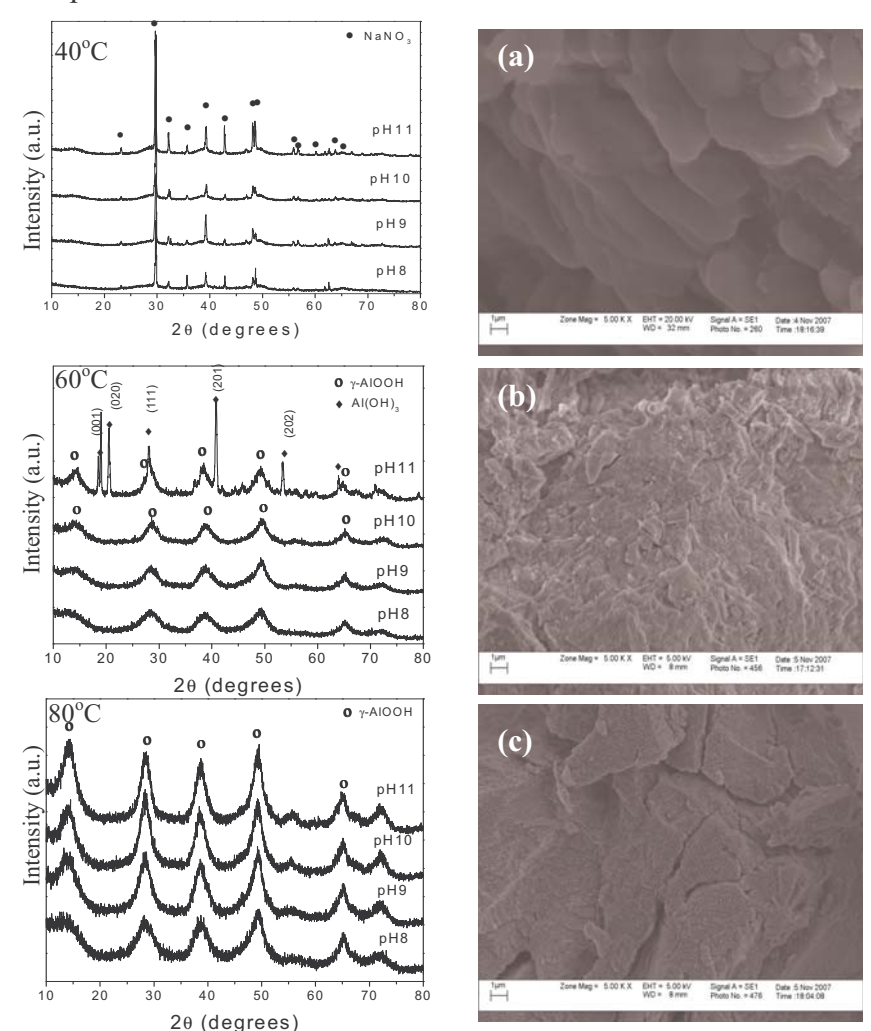
Aluminum nitrate nanohydrate (AlN₃O₉.9H₂O), sodium aluminate (Na₂Al₂O₄) and sodium hydroxide (NaOH) were used as starting materials for production of boehmite. Required quantity of AlN₃O₉.9H₂O and Na₂Al₂O₄ were dissolved in distilled water (1 molar). The mixture was stirred for 20 h at room temperature. A stoichiometric amount of dilute sodium aluminate was added to the mixture with simultaneous stirring. Desired pH value was adjusted by sodium hydroxide. The solution was heated in the temperature range 40°C -80°C and was refluxed for 6 h after the precipitate was initially formed. Finally, the white precipitate was filtered, washed with distilled water and then dried in an oven. To produce γ -Al₂O₃, obtained AlOOH with smallest crystalline size was selected and subjected to different calcination temperatures. The samples were characterized by X-ray diffraction (XRD: X'Pert X-ray diffractometer) and scanning electron microscopy (SEM: JEOL JSM-6300). The XRD patterns of the nanoparticles were verified by comparison with the JCPDS data. Broadening of the peak was related to the average diameter (*L*) of the particle according to Scherrer's formula, i.e. $L = 0.89\lambda/\Delta\cos\theta$ where λ is X-ray wavelength, Δ is line broadening measured at half-height and θ is Bragg angle of the particles.

Results and Discussion

Precipitation from solutions of aluminum nitrate nanohydrate and sodium aluminate mixtures was observed at 40, 60 and 80°C due to the decomposition of NaOH. Fig.1 shows XRD patterns of the precipitated phase after washing and drying. The powder precipitates at 40°C for pH = 7-11 were found to be identified as crystalline NaNO₃. However, this NaNO₃ phase completely disappeared after being heated up to 60 and 80°C, as shown in Fig. 1. At the same temperature, the γ-AlOOH crystals are gradually formed (pH = 7-11). Linewidth of all patterns indicate that all precipitated powders are characterized by nano-size crystals. The main diffraction peaks can be indexed within the experimental error as boehmite y-AlOOH (JCPDS file No. 21-1307) which has orthorhombic structure in space group Amam (63) with lattice parameters a = 3.700, b = 12.227 and c = 2.868 Å. In detailed investigation, at pH 7 to 8, pseudoboehmite or gelatinous boehmite were also found while at higher pH, i.e. 9-11, well-crystallized boehmite was formed. To observe the difference, crystalline size of all powders were determined via calculation by means of diffraction peak broadening according to the Scherrer equation. Broadenings due to instrumental effects were eliminated before peak analysis. The result of calculation using reflection from (120) plane are summarized in Table 1. According to phase formation, it can be seen that the related crystalline size of pseudobomite seem to decrease but those of normal boehmite increased with increasing pH. Formation of these two forms of boehmite from different pH range may correspond to different rate of Al-OH interaction as pointed out by Bokhimi et al. [6] that the smaller boehmite crystalline size is the higher Al-OH reaction. This is also consistent with the report of Okada et al. [1] which suggested that at temperature 60°C, the boundary of gel-like state and crystalline boehmite is situated between pH 7 to 8. The same suggestion was also expressed by Panias and Krestou [7]. The gel-like state is in fact characterized by a higher degree of short-range order arrangement. For the diffraction patterns of precipitate obtained from pH 7 and 8, lower peaks relative intensities couple with a broader linewidth are clearly evidenced the observation of such gel-like state with considerable in a larger proportion. At pH value exceeded 8, the precipitate went across that boundary and readily form well-defined crystalline boehmite and their crystallite size increased with the pH value. The same observation was also reported by Okada et al [1]. This effect can be explained as enhancement of the dissolution-reprecipation reaction by a higher pH and giving a larger crystalline size. SEM micrographs of four precipitate are shown by Figure 1(a-c). It can be seen that the microstructure of sample precipitated at 40°C and pH 6 exhibited a less well-defined



shape of NaNO₃ with lower porosity and the larger aggromeration was also observed. For other temperature conditions



with higher pH, boehmite particles higher aggromeration clearly seen. This is because boehmite itself show a layered structure which each layer linked by H-bond. Thus aggromeration of those layers could form easily. In fact, the mechanism of crystal growth for boehmite and the effect of pH on the particle morphology are not well understood. It has been proposed that the different morphologies observed correspond to different growth mechanisms; direct crystal growth from solution produce particles with a welldefined growth morphology while a particle coagulation mechanism produces particles of variable morphology [8, 9]. After calcination of boehmite powder at 350-1100°C for 4 hr. with heating rate of 5°C/min, the calcined powders were investigated in terms of phase formation and morphology.

Fig. 1 XRD patterns of samples prepared with initial pH of 7, 8, 9, 10 and 11 at the temperature in the range of 40–80°C and SEM micrographs of sample precipitated at (a) 40°C, (b) 60°C and (c) 80°C, respectively.

Fig. 2 shows XRD patterns of calcined transition alumina produced from four boehmites obtained from four different pH conditions. All XRD patterns can be identified as γ -Al₂O₃ phase with strongest reflection at $2\theta = 68^{\circ}$, (100). Formation of α -Al₂O₃ phase is also found at 1000° C. Though, they produced from different boehmite morphology and crystalline size but there were no significant distinctive. However, with detailed observation, it is suggested that at the same heating temperature, boehmite of larger crystalline size provided sharper and more intense γ -Al₂O₃ XRD peaks. The present study is consistent with one that reported by Okada et al. [10]. The morphology of γ -Al₂O₃ still very much like that of boehmite which strong aggromeration is also found and this also seen in the line shape of the XRD peaks.

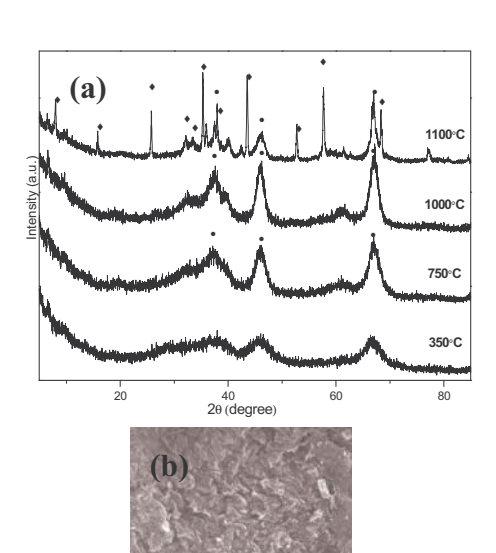
Summary

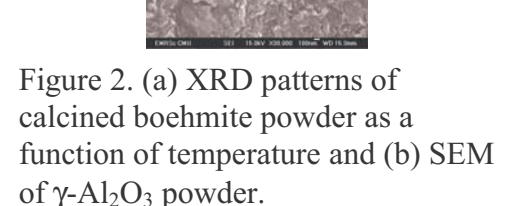
Crystalline size and morphology of boehmite are sensitive to precipitation conditions. This is especially pH of the starting solution and temperature. The higher pH value gives a larger crystalline size with stronger aggromeration. Two forms of boehmite i.e, pseudobomite and crystalline boehmite, were found after precipitation completed. Transformation of boehmite to produce γ -Al₂O₃ occurred at 350-1000°C for 4 h, the aggromeration was found and their morphologies very much the same as that of boehmite precipitated from pH 8-11 with 60 and 80°C.



Table 1 Effect of pH and temperature conditions on crystalline size of boehmite powder.

Precipitation c	onditions	Crystalline size	Phase
Temperature	рН	(nm)	
(°C)			
40	7	-	$NaNO_3$
40	8	-	$NaNO_3$
40	9	-	$NaNO_3$
40	10	-	$NaNO_3$
40	11	-	$NaNO_3$
60	7	-	NaNO ₃ , γ-AlO(OH)
60	8	2.5	γ-AlO(OH)
60	9	2.7	γ-AlO(OH)
60	10	3.8	γ-AlO(OH)
60	11	-	$Al(OH)_3$
80	7	-	NaNO ₃ / γ-AlO(OH)
80	8	2.4	γ-AlO(OH)
80	9	3.3	γ-AlO(OH)
80	10	3.7	γ-AlO(OH)
80	11	3.9	γ-AlO(OH)





Acknowledgements

This research was supported by The Thailand Research Fund (TRF) and National Research Council of Thailand. P. P. would like to thankful to The Young Scientist and Technologist Program (YSTP).

References

- [1] K. Okada, T. Nagashima, Y. Kamishima, A. Yasumori, and T. Tsukada: J. Colloid. Interf. Sci. Vol. 253 (2002), p. 308.
- [2] H. S. Potdar, K-W. Jun, J. W. Bae, S-M. Kim and Y-J. Lee: Appl. Catal. A-Gen. Vol. 321 (2007), p. 109.
- [3] M. Machida, M. Takenami and H. Hamada: Solid State Ionics Vol. 172 (2004), p. 125.
- [4] P. Alphonse and M. Courty: Thermochim. Acta. Vol. 425 (2005), p. 75.
- [5] R. Petrovic, S. Milonjic, V. Jokanovic, Lj. Kostic-Gvozdenovic, I. Petrovic-Prelevic and Dj. Janackovic: Powder Technol. Vol. 133 (2003), p. 185.
- [6] Bokhimi, J. A. Toledo-Antonio, M. L. Guzman-Castillo and F. Hernandez-Beltran: J. Solid State Chem. Vol. 159 (2001), p. 32.
- [7] Panias and A. Krestou: Powder Technol. Vol. 175 (2007), p. 163.
- [8] J.C. Hulling and G.L. Messing: J. Non-Cryst. Solids Vol. 147 (1992), p. 213.
- [9] C. Kaya, J. Y. He, X. Gu, and E. G. Butler: Micropor. Mesopor. Ma. Vol. 54 (2002), p. 37.
- [10] K. Okada, T. Nagashima, Y. Kameshima and A. Yasumori: J. Colloid Interf. Sci. Vol. 248 (2002), p. 111.





JOURNAL OF

MICROSCOPY SOCIETY OF THAILAND

AN OFFICIAL PUBLICATION OF MICROSCOPY SOCIETY OF THAILAND

Volume 22 ISSN 0857-5285 February 2008

CONTENTS

Defects in Multiple InGaN/GaN Quantum Wells and Structure of High Density InGaN Quantum Dots
Influence of the <i>Broussonetia papyrifera</i> (L.) Vent Pulp to Control the Size of SnO ₂ Nanoparticles by Precipitation Coupling with Thermal Decomposition Methods
Effect of Ru on Photocatalytic Activity of TiO ₂ Nanoparticles
Surface Image of Charcoal and Activated Charcoal from Banana Peel
Effect of pH on Phase Formation and Morphology of the Nanocrystalline Boehmite Powder Prepared by A Precipitation Method
Electron Microscopy and Optical Spectroscopy Analyses of Carbon Nanotube Composite Electrodes for Dye-Sentisized Solar Cells
A Microstructural Investigation of Al-doped ZnO films Prepared by Spray Pyrolysis
Phase Formation and Microstructure of Ba(Zr _{0.20} Ti _{0.80})O ₃ Ceramics Prepared via Solid State Reaction Method
Microstructures of Dip-coated TiO ₂ Thin Film Capacitor
Collagen Measurement and Staining Pattern of Wound Healing Comparison with Fixations and Stains37 S. Ukong, S. Ampawong, and K. Kengkoom
Effect of Polysaccharide from <i>Phellinus ignarius</i> (L.) Quél. on Hematological Values and Blood Cell Characteristics in Diabetic Rats
Microscopy and Image Analysis Techniques for Quality Control in Food Industry: A Case Study of Wheat Grain Cooking Process

Neuronal Sprouting Following Spared Nerve Injury in Rats Studied by Cholera Toxin B Subunit Immunoreactivity)
S. Chompoopong, K. Bamrungsuk, K. Tilokskulchai and T. Wongtawatchai	
Light and SEM Studies on Leaf Litter Fungi56 L. Manoch, O. Jeamjitt, A. Eamvijarn, T. Dethoup, J. Kokaew, Y. Paopun, P. Poochinya and P. Umrung	,
Diversity of Arbuscular Mycorrhizal Fungi in Forest Restoration Area of Doi Suthep-Pui National Park, Northern Thailand	1
Some Hematological Values and Ultrastructure of Blood Cells in <i>Piper sarmentosum</i> Roxb. and <i>Tinospora crispa</i> Miers ex Hook. F & Thoms. Treated Diabetic Rats	
Hematological Values and Morphological Observation of Blood Cells in Balloon Frog, <i>Glyphogloossus molossus</i>	
Morphological Changes of Rice Starch During Grain Development	



JOURNAL OF

MICROSCOPY SOCIETY OF THAILAND

AN OFFICIAL PUBLICATION OF MICROSCOPY SOCIETY OF THAILAND

EDITORIAL BOARD

Editor-in-chief

Sukumal Chongthammakun

Associate Editors

Pansiri Phansuwan
Prapee Sretarugsa
Wandee Apinhasmit
Chanchana Thanachayanont
Thoranin Chairoungsri
Amporn Wiengmoon

International Advisory Board

Chris Boothroyd, Singapore Makoto Shiojiri, Japan Tae-Yeon Seong, Korea Samual Sam-Wah Tay, Singapore Hiang Lian Hing, Malaysia Kei-Ichi Hirai, Japan

Defects in Multiple InGaN/GaN Quantum Wells and Structure of High Density InGaN Quantum Dots

J.R. Yang¹, W.C. Li¹, J.T. Hsu² and M. Shiojiri³*

¹Institute of Materials Science and Engineering, National Taiwan University, Taipei, Taiwan 106, Republic of China

²Electronics and Optoelectronics Research Laboratories, Industrial Technology Research Institute, Hsinchu, Taiwan 310, Republic of China

³Kyoto Institute of Technology, Kyoto 606-8585, Japan

*Present address: 1-297 Wakiyama, Enmyoji, Kyoto 618-0091, Japan

E-mail: shiojiri@pc4.so-net.ne.jp

Abstract

InGaN-based multiple quantum wells (MQWs) used in light emitting diodes and laser diodes exhibit extraordinary high light emission efficiency despite high defect density. The mechanism of the high photoemission is still not fully understood. Here, we deal with this problem, reviewing some recent investigations on In-rich regions and V-defects in the MQW active layer. We also show a structural investigation of three dimensional high-density quantum dots fabricated, instead of QWs, in the active layer. The shape and size of the InGaN quantum dots and the SiN_x masks for the growth of the dots have been revealed using high-angular annular dark field scanning transmission electron microscopy, energy dispersive X-ray spectroscopy nanoanalysis and high-resolution transmission electron microscopy.

Background

InGaN/GaN quantum well (QW) structures have been widely produced for light emitting diodes (LEDs) and laser diodes (LDs) over a range of visible and ultraviolet wavelengths [1]. This is due to exceptionally high photoemission efficiency from In_xGa_{1-x}N QWs despite quite a few threading dislocations involved. We previously reviewed our structure investigations on the InGaN/GaN multiple quantum well (MQW) active layers and on the strain AlGaN/GaN superlattice cladding layers [2, 3]. We were the first to establish the structure of Vshape (V) defects with thin sidewalls of InGaN/GaN QWs which are different from the main c-plane QWs, although it had been predicted by Wu et al. [4]. High-angle annular dark field scanning transmission electron microscopy (HAADF-STEM) [5-7] and field emission scanning electron microscopy led to this evidential result [3]. Then, we proposed a formation mechanism of the V defects, taking into account the growth kinetics of the GaN crystal and the masking effect of In atoms on the analogy of the epitaxial lateral overgrowth (ELOG) [2].

An atomic resolution HAADF-STEM imaging, which provides simultaneously the precise position of the atomic columns and the clearly Z-dependent contrast (where Z means atomic number), allows us to map quantitatively both the strain field and In atom distribution in the InGaN QWs. We showed thereby that the lattice expanded largely along the c axis but hardly in the c plane, in the In_{0.25}Ga_{0.75}N QWs [3]. The maps directly led to results that there is a local fluctuation of In atoms in the InGaN layers, and that the In-rich regions, considered to be quantum dots (QDs), corresponding to lattice

expansion along the c axis. This was the first direct evidence of local phase separation or QDs. Several reports, including the paper by Y. Narukawa et al. [8] who first proposed the QDs for explanation of the high light emission efficiency, had assumed indirectly the In concentration from the lattice strain only using the Vegard law approximation. However, the mechanism of the high emission of InGaN-based LEDs and LDs has not been fully understood, at the present becoming more and more confused. The first part of this paper reviews investigations on the emission mechanism relating with the defects mentioned above.

It was believed that the carriers deeply localized in the QDs and hindered from migrating toward dislocations in QWs cause the photoluminescence (PL) surprisingly unaffected by numerous dislocations [8]. Therefore, it was expected that the performance of LDs might be improved if the density of QDs would be made much higher than that of dislocations. The structures comprising three-dimensional QDs, instead of QWs, in the active layer, have been fabricated. Next, we report on our structural investigation of a multiple stack of ultra-high density InGaN QDs that was prepared as a trial [9].

Light Emission and Structural Defects in InGaN MOWs

It was shown from cross-sectional TEM and energy-dispersive X-ray (EDX) microanalysis that the deep localization of excitons (or carriers) originates from the In-rich regions acting as QDs [8]. Then, the high emission efficiency of InGaN-based LED was explained to be mostly due to the

large localization of excitons because the pathways of nonradiative recombination are hindered once the excitons are captured in a small volume. As mentioned above, we showed an evidential observation of the In-rich regions by HAADF-STEM [3].

Wu et al. [4] correlated the long-wavelength shoulder feature in the bulk PL and cathodoluminescence spectra with the V-defects,

proposing the {1011} side-wall QW structure of the V defect, and concluded that the V defect is associated with a localized exciton recombination process. They suggested that either the formation of QD-like structures at the apex of the V defect with each InGaN QW or the luminescence of Inrich pyramid side walls is regarded as the source of the long-wavelength shoulder emission. confirmed, by HAADF-STEM, the In-rich regions at the apices of the V defects [2], which were regarded as the masks for the V-defect formation. Then, we also concluded that these side-wall InGaN/GN QWs originate additional wavelength small emissions like the emissions between 416 nm and 417 nm appearing in the emission spectrum of our 415.5-nm MQWs.

Recently, Smeeton et al. [10], have reported that such dotlike structures may be artifacts due to radiation damage during TEM observation. Their HRTEM images that were acquired immediately after first irradiating QW indicated no gross fluctuations of In content in the InGaN alloy. Only period of irradiation brief introduced inhomogeneous strain, which was very similar to that expected from genuine nanometer-scale In composition fluctuations. Then, they suggested the possibility of falsely detecting In-rich "clusters" in a homogeneous OW. Referring this experiment, Hangleiter et al. [11] described that the unexpectedly high emission efficiency of GaInNbased LEDs relies on self-screening of defects rather than random localization since V-shape pits decorating every threading dislocation can be forced to exhibit sidewall QWs with reduced thickness and higher band gap thus leading to a potential barrier around every defect, which keeps carriers from recombining nonradiatively at the defect. They showed that the spectra from areas close to defects exhibited, besides the main emission at 430 nm, additional emission peaks in the 380-410 nm range ascribed to the narrow QWs

on the {1011} side-walls. However, the situation seems to have become more confused. Smeeton *et al.* did not indicate confidently what the damage mechanism was, although they supposed simply that the localized contrast may be the result of point defect generated by ionization damage of bulk type knock-on displacement of nitrogen (Frenkel pair creation). They touched on nothing about In

distribution in the electron beam irradiated QWs, although EDX microanalysis [8] and HAADF-STEM observations [2, 3] certainly had shown the local fluctuation of In atoms. The image recorded within ~20 s in Ref. 10 exhibited very weak contrast with almost the same feature as that in the image recorded after a few minutes of exposure. One possibility is that the weak contrast occurred during the expose of 20 s. The other is that the strain in the In-rich region was only disclosed by electron beam irradiation, which may relax the lattice in small In-rich region, restrained to fit with the lattices of the enclosure. Therefore, direct composition analysis is still necessary to prove that there are not any In-rich regions to be acting as QDs in the undamaged InGaN QWs and the In-rich regions are caused by electron beam irradiation. The additional short-wavelength emission peaks

[11] would be plausibly ascribed to the thin {1011} side-wall QWs, but it may note that the observed long-wavelength peaks or shoulder [4] may also not originate regardless of them.

Ultrahigh Density InGaN Quantum Dots

One approach for fabricating the 3D InGaN QDs was the deposition of silicon anti-surfactant or SiN_r nano-masks, which altered the morphology of the InGaN films from that of step flow to that of a three-dimensional island. We have observed a similar sample [9] to the ultra-high density InGaN QDs samples that were prepared by Tu et al. using the SiN_x nano-mask and exhibited strong PL emission at room temperature (RT) as shown in figure 1 [12]. The structure is schematically shown, together with growth condition, in figure 2. Masking with a rough SiN_r layer was formed on the GaN:Si underlying layer, at flow rates of 5 slm for NH₃ and 50 sccm for diluted Si₂H₆. The deposition of a pair of the SiN_x and In_xGa_{1-x}N was repeated using a spacer of the GaN:Si barrier layer deposited at 1000°C, and finally the last In_xGa_{1-x}N layer was capped with an un-doped GaN layer. All the layer thicknesses shown in figure 4 are nominal values. The specimens for cross-sectional EM nanoanalysis were prepared by mechanical polishing, followed by ion milling. HAADF-STEM, HRTEM and EDX nanoanalysis were performed in a Tecnai 30, equipped with a lens of Cs=1.2 mm, operated at 300 keV. The HAADF-STEM images were recorded in a detector range of D=36~181 mrad using a convergent electron probe with a semiangle of 15 mrad.

Figure 3a shows a low magnified HAADF-STEM image of the specimen. Figure 3b is EDX spectrum in the area P, which comprises emissions from In, Ga, N, and Si. Therefore, the bright area along C-D in the HAADF-STEM image might be a layer containing InGaN QDs (QDs layer). From

figure 3d the width of this layer is estimated to be \sim 15 nm. The In-L $_{\beta}$ intensity profile in figure 3f indicates that very roughly estimated width of the QDs is 10 nm on the C-D.

Figure 4a shows a HAADF-STEM image near the top of the specimen. The dark line is identified, due to the small thermal diffuse scattering crosssection of Si^{14} (and N^7), as the projection of a layer composed of SiN_x mask islands. The height of the SiN_r masks is roughly estimated to be less than 2 nm from the thickness of the dark line. The $In_x^{49}Ga_{1-x}^{31}N^7$ QDs are observed as bright triangles, which look peaks in a mountain chain, in the QDs layer between two-dotted lines in the HAADF-STEM image. Figure 4b shows an HRTEM image near the specimen edge, where a part of the capping layer was removed during the ion-milling. Quite high QDs (indicated by arrowheads) are seen on the SiN_x mask layer. The lattices of the SiN_x are heavily strained. We could not determine the crystal structure and the composition x of the SiN_x. The dark contrast for the ODs may be caused by diffraction effect of the high structure amplitude of In and large lattice strain. The lattices of the InGaN crystals are strained compared with the underlying and the capping GaN lattices, although contacting with the lattice of the GaN in the coherent relation. The QDs can be regarded as nanoisland crystals with the {1011} side walls and a height of several nanometers (a height as high as 20 nm in this layer). This crystal habit can be understood in taking account of ELOG or the crystal growth through masks at lower reactor temperature [2]. Thus, we can propose the structure for this threedimensional InGaN quantum dots as the inset in figure 2. Further spectroscopic and structural analyses of such high density QDs may lead to a solution for whether the high emission efficiency of InGaN-based devices is ascribed to QDs or not.

Investigation presented in this section has been made with the collaboration of Dr. H.L. Tsai and Dr. T.Y. Wang, National Taiwan University, and Dr. T.C. Wang, Industrial Technology Research Institute, Taiwan.

References

 Nakamura S, Senoh M, Nagahara S, Iwasa N, Yamada T, Matsushita T, Kiyoku H, Sugimoto Y, Kozaki T, Uemoto H, Sano M, and Chocho K. InGaN/GaN/AlGaN-based laser diodes with modulation-doped strained-layer superlattices grown on an epitaxially laterally overgrown GaN substrate. *Appl. Phys. Lett.* 1998; 72: 211-213.

- 2. Yang J R and Shiojiri M. Electron microscopy studies of GaN-based violet laser diodes II. *J. Micros. Soc. Thailand* 2007; 21: 1-7.
- 3. Shiojiri M and Saijo H. Electron microscopy studies of GaN-based violet laser diodes. *J. Micros. Soc. Thailand* 2005; 19: 1-10.
- Wu X H, Elsass C R, Abare A, Mack M, Keller S, Petroff P M, DenBaars S P, Speck J S, and Rosner S J. Structural origin of Vdefects and correlation with localized excitonic centers in InGaN/GaN multiple quantum wells. *Appl. Phys. Lett.* 1998; 72: 692-694.
- Shiojiri M. Electron microscopy studies of ceramics. J. Micros. Soc. Thailand 2004; 18: 1-11.
- Shiojiri M and Watanabe K. Atomic resolution high-angle annular dark field scanning transmission electron microscopy and its application to materials characterization II. *J. Electron Micros. Soc. Thailand* 2002; 16: 34-36
- 7. Shiojiri M, Yamazaki T, Kawasaki M, and Watanabe K. Atomic resolution high-angle annular dark field scanning transmission electron microscopy and its application to materials characterization. *J. Electron Micros. Soc. Thailand* 2001; 15: 11-13.
- Narukawa Y, Kawakami Y, Funato M, Fujita S, Fujita S, and Nakamura S. Role of selfformed InGaN quantum dots for exciton localization in the purple laser diode emitting at 420 nm. *Appl. Phys. Lett.* 1997; 70: 981-983.
- 9. Tsai H L, Wang T Y, Yang J R, Wang T C, Hsu J T, and Shiojiri M. Observation of ultrahigh density InGaN quantum dots. *J. Appl. Phys.* 2007; 102: 013521 (4 pages).
- Smeeton T M, Kappers M J, Barnard J S, Vickers M E, and Humphreys C J. Electronbeam-induced strain within InGaN quantum wells: False indium "cluster" detection in the transmission electron microscope. *Appl. Phys. Lett.* 2003; 83: 5419-5421.
- Hangleiter A, Hitzel F, Netzel C, Fuhrmann D, Rossow U, Ade G, and Hinze P. Suppression of nonradiative recombination by V-shaped pits in GaInN/GaN quantum wells produces a large increase in the light emission efficiency. *Phys. Rev. Lett.* 2005; 95: 127402 (4 pages).
- 12. Tu R C, Tun C J, Chuo C C, Lee B C, Tsai C E, Wang T C, Chi J, Lee C P, and Chi G C. Ultra-high-density InGaN quantum dots grown by metalorganic chemical vapor deposition. *Jpn. J. Appl. Phys.* 2004; 43: L264-L266.

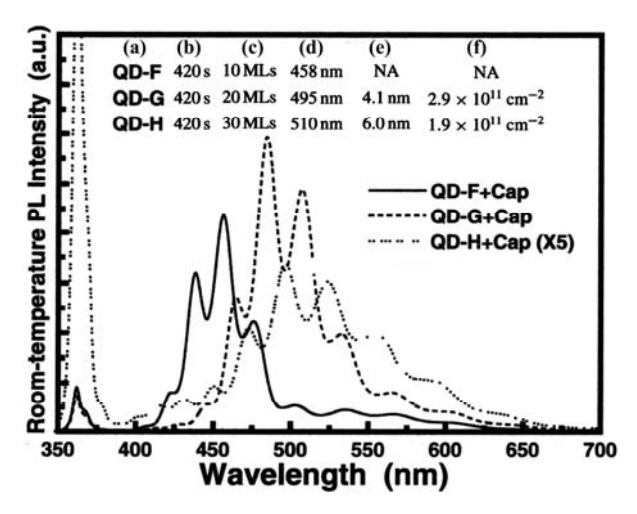


Fig. 1 RT PL spectra of the InGaN quantum dots (QDs) prepared different conditions. (a) sample number, (b) SiN_x treatment time, (c) monolayer number of deposited InGaN (20 MLs correspond to 5 nm thick) (d) PL peak wavelength (with 10 nm GaN cap), (e) QD's height estimated from atomic force microscopy, (f) QD's density. [12]

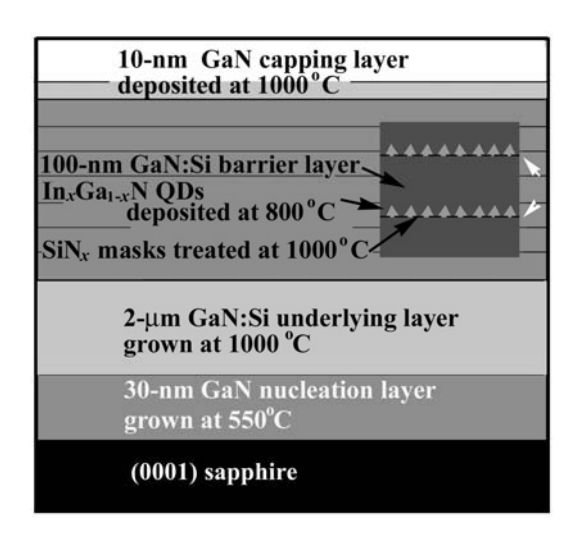


Fig. 2 Structure and growth condition of ultra-high density InGaN QDs used in the present experiment. [9]

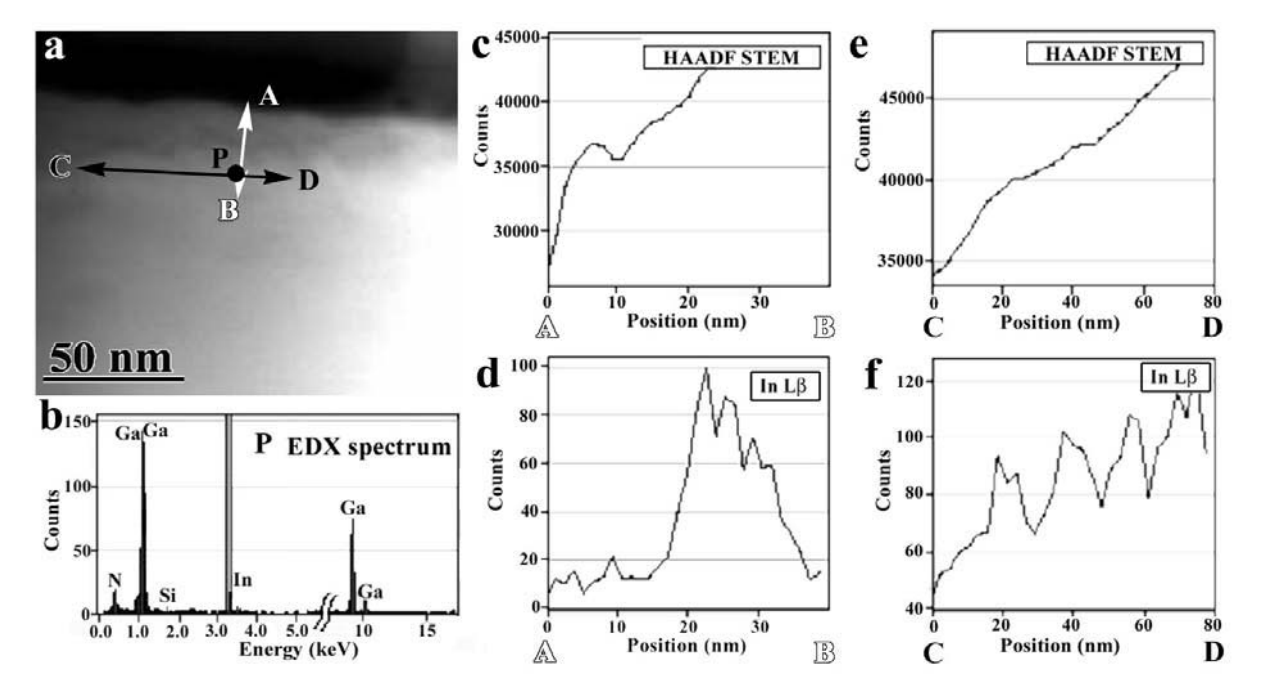


Fig. 3 (a) HAADF-STEM image in which the areas for EDX analysis are indicated. (b) EDX spectrum in the area P (a probe size of \sim 0.5 nm). (c), (d) HAADF-STEM intensity profile and indium L_β intensity profile in EDX analysis, along the line A-B (\sim 1 nm wide). (e), (f) HAADF-STEM intensity profile and indium L_β intensity profile, along the line C-D.

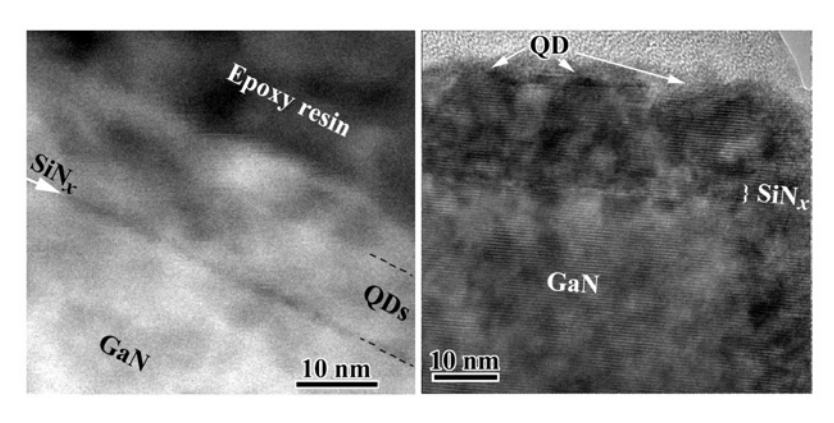


Fig. 4 (a) HAADF-STEM image near the top of the specimen. The layer of SiN_x masks appears as a dark line. The area between two dotted lines is a QDs layer which comprises the InGaN QDs and is capped with GaN. (b) HRTEM image, where the capping GaN layer was almost removed during the ion-milling and InGaN QDs are visible, accordingly.

Influence of the *Broussonetia papyrifera* (L.) Vent Pulp to Control the Size of SnO₂ Nanoparticles by Precipitation Coupling with Thermal Decomposition Methods

R. Janmanee 1*, P. Pirakitikulr², C. Liewhiran³ and S. Phanichphant 1,4

Abstract

 SnO_2 nanoparticles were successfully synthesized with the presence (PS) and absence (NPS) of the *Broussonetia papyrifera* (L.) Vent pulp as the dispersant by precipitation coupling with thermal decomposition methods using tin tetrachloride pentahydrate ($Sn_4Cl.5H_2O$) and ammonium hydroxide (NH_4OH) as the starting material and precipitant, respectively. The pulp was soaked in $SnCl_4$ solution and NH_4OH was slowly added dropwise. The white gelable precipitate of $Sn(OH)_4$ was obtained. Afterwards, the white precipitate was filtered and washed until chloride was removed. The mixtures were dried at $80^{\circ}C$ for 24h. The resulting samples were calcined for 1h at 600, 650, and 700°C. The morphologies and chemical compositions of the pulp were evaluated by low vacuum-scanning electron microscopy (LV-SEM) and energy-dispersive X-ray spectrometry (EDS) elemental mapping, respectively. The resulting SnO_2 nanopowders were further analyzed by XRD, TEM, and BET analyzers. The accurate crystallite sizes of SnO_2 nanoparticles with the presence and absence of the pulp were found to be ranging from 5-15 nm and 5-30 nm, and the specific surface area (SSA_{BET}) were 62.53 m^2/g and $26.60 m^2/g$, respectively.

Background

The synthesis of nanosized-particles materials has generated the interest of many researchers, due to their higher active surface area than the same materials with larger particle sizes. Controlling the morphological properties of materials during synthesis is very important. Moreover, properties of the materials can be improved by doping with small amount of transition metals such as Pd, Pt, Au, Mo, In and Ru [1-5].

Tin dioxide (SnO_2) is one of the most important multifunctional oxide materials, as a wide-band gap and n-type semiconductor with band gap of to 3.6 eV [4-11]. SnO₂ nanoparticles have been extensively used in many areas and utilized for its unique electrical, luminescence, and catalytic properties [11-13]. Nano-sized SnO₂ materials have specific properties and advantages of high sensitivity, conductivity, transparency in the visible region, with addition in mechanical and chemical stabilities. They are used in many applications. such as ceramic materials [13, 14], lithium batteries [15], catalysis [16], transistors [12], electrodes [16], solar cells [10], microelectronics [10], biomedicines [14], photocatalystes [17-18] and gas sensors [19-20].

Synthesis of nanometerials with well-controlled size, morphology and chemical composition may open opportunity in exploring new properties. The crystalline structure, the size and shape of the particles are highly dependent on the method of synthesis. Thus, it is necessary to adjust the synthesis method of the nanoparticles to assure high quality materials. Properties of nanoparticles related to size uniformity, particles morphology, purity and chemical homogeneity are critical during the processing and sintering steps in order to determine the macrostructure of material and the final properties of the resulting material. Several methods have been developed to prepare the SnO₂ nanoparticles, including sol-gel [9, 17], gas phase condensation [6], precipitation [9], hydrothermal [13], mechanochemical [11] and thermal decomposition [21]. All methods have their own limitations in controlling the structures of SnO₂ nanoparticles with different shapes, size and morphology.

This present study describes the precipitation coupling with thermal decomposition method performing at relatively low temperature to produce the desired SnO₂ nanoparticles. In these methods, SnO₂ nanoparticles synthesized with and without a pulp as a dispersant were prepared.

¹ Nanoscience Research Laboratory (NRL), Department of Chemistry, Faculty of Science, Chiang Mai University, Chiang Mai, Thailand 50200

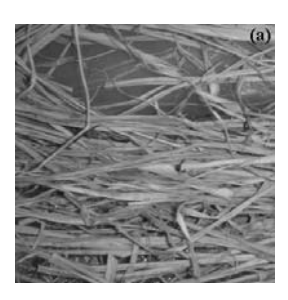
² Faculty of Pharmacy, Payap University, Chiang Mai, Thailand 50000

³ Department of Physics, Faculty of Science, Chiang Mai University, Chiang Mai, Thailand 50200

⁴ NANOTEC Center of Excellence, Chiang Mai University, Chiang Mai, Thailand 50200 e-mail: joy rapiphun@yahoo.com

Broussonetia papyrifera (L.) Vent pulp was shown in figure 1. It was specifically chosen because it is a local and common plant in Thailand. It is inexpensive and readily available especially in the Northern part of Thailand. It is the most common material in making rice paper. Scientifically, Broussonetia papyrifera (L.) Vent is classified in Kingdom Plantae, Division Spermatophyta, Class Angiospermae, Subclass Dicotyledonae, Order Urticales, Family Moraceae, Genus Broussonetia, and Species papyrifera [22,23]. In Thailand, it is known as the Por-Saa (figure 1(a)). In English, it is usually called paper mulberry. We believe that the fiber chains of the pulp play an important role in controlling the size of the SnO₂ particles by providing a template for the particle formation. The pulp also serves as a dispersant to separate SnO₂ particles. SnO₂ nanoparticles can be easily prepared, and well controlled for particles size, morphology, phase homogeneity resulting in an increase of SSA_{BET} and non-agglomeration of the particles.

In this work, SnO₂ nanopowders were further characterized by using a low vacuum-scanning electron microscopy (LV-SEM), energy-dispersive X-ray spectrometry (EDS), X-ray diffraction (XRD), transmission electron microscopy (TEM) nitrogen adsorption (BET) analysis, respectively. LV-SEM and EDS were used to analyze the fibers morphology and chemical compositions of the pulp. XRD was used to confirm the phase and crystalline structure of the SnO₂. TEM was selected to determine the accurate size and morphology. BET was a method of choice to evaluate the specific area of SnO₂ nanoparticles.



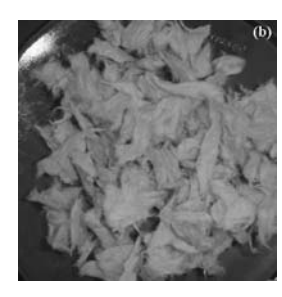


Fig. 1 (a) The dried.L) Broussonetia papyrifera) Vent pulp, and (b) the tissue membrane of pulp was used as a dispersant

Materials and Methods

1. Preparation of $Broussonetia\ papyrifera\ (L.)\ Vent\ Pulp$

At room temperature, 1.25 M sodium hydroxide (NaOH) solution was prepared by dissolving 25 g of NaOH in 1000 mL of distilled water. 500 mL of the solution was added to 15 g of dry pulp. The mixture was soaked for 24h and boiled for 5h at 100-120°C. The tissue membranes of a pulp were

washed in water until the pH was approximately neutral. The tissue membranes were then blended for 1h using an Imaflex IF-300 Super Blender. The resulting paste was dried at 80°C for 72h in an oven as shown in figure 1(b).

2. Preparation of Nano-sized SnO₂ Powders

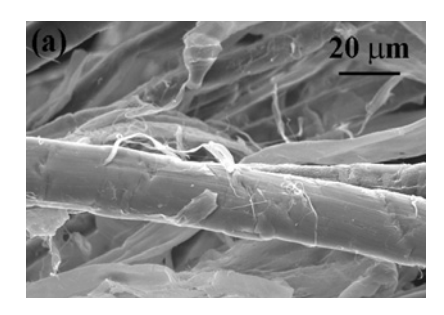
At room temperature, 11.6 g of tin tetrachloride pentahydrate (SnCl₄.5H₂O) was stirred and dissolved in 700 mL DI water. 2.9 g of dried tissue membranes of the pulp was added into tin tetrachloride solution. Precipitation step was also performed at room temperature by using 15 mL NH₄OH as a precipitant, which was slowly added dropwise into tin tetrachloride solution until the pH was approximately 9. The white gelable precipitate of Sn(OH)₄ was obtained. The white precipitate was filtered and washed thoroughly until free of chloride by testing the filtrate with silver nitrate solution. A parallel synthesis was also performed but this time without the pulp membrane. The mixtures were dried at 80°C for 24h in an oven, and then ground. The resulting mixture was calcined at 600, 650, and 700°C. Nano-sized SnO2 powders were obtained after calcination of the product for 1h in all samples.

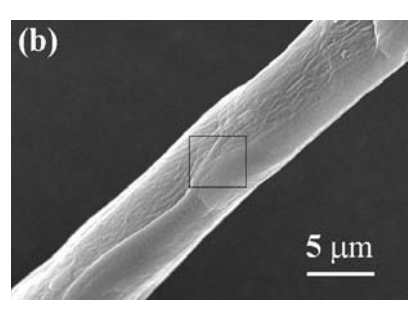
3. Nanopowders characterizations

The morphology of nanostructure in fiber chains and chemical compositions of the pulp were observed and analyzed by a low vacuum-scanning electron microscopy (LV-SEM) [JSM-5910LV, JEOL] and energy-dispersive X-ray (EDS) spectrometry [JSM-5910LV, JEOL], respectively. For XRD analysis, the phase and crystallinity of SnO₂ synthesized with and without the pulp of nanopowders were analyzed by XRD [Bruker D8 advance diffractometer, operated at 40 kV, 40 mA] using CuK α radiation at $2\theta = 20-80^{\circ}$ with a step size of 0.06° and a scanning speed of 0.72°/minute.The fundamental parameter approach and Rietveld method [53], were used to calculate the crystallite size of particles. The phase and the corresponding sizes were calculated using the TOPAS software. The morphology and accurate particle sizes of SnO₂ nanopowders were analyzed by transmission electron microscopy (TEM) [JSM-2010, JEOL]. The specific surface areas were analyzed from BET measurements [Micromeritics Tristarl. The specific surface areas of SnO₂ nanoparticles with the presence and absence the pulp as a dispersant were calculated and the approximate particle sizes (d_{BET}) were determined by 5-point nitrogen adsorption from the Bruneauer-Emmett-Teller (BET) measurements at 77 K. All samples were controlled with degassing at 150°C for 1 h prior to analysis.

Results and Discussion

The morphology of fibers and chemical composition of the pulp were shown in figures 2 (a), (b), and (c). They were observed and analyzed by SEM and EDS elemental mapping. A surface morphology like natural cellulose can be clearly seen in figure 2 (a). The sizes of fibers were found to be in the micrometer range. Figure 2 (b) shows the region analysis. The square emphasized the selected area which was investigated for the elemental compositions. Figure 2(c) gives the elemental composition signals of the elemental region as indicated in figure 2 (b). Signals corresponding to C (0.3 KeV) and O (0.55 KeV) were elements observed. These elemental compositions of the pulp generally correspond to those of natural cellulose.





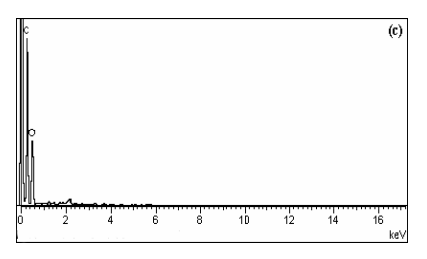


Fig. 2 (a), (b) SEM images of the morphology of the tissue membrane of the *Broussonetia papyrifer* (L.) Vent pulp with different magnifications, and (c) EDS elemental mapping of the tissue membrane of the pulp. The square emphasized the selected area which investigated for the elemental compositions.

X-ray diffraction patterns of SnO₂ nanopowders synthesized with the presence (line (a)-(c)) and absence (line (d)-(e)) *Broussonetia papyrifera* (L.) Vent pulp as a dispersant at 600, 650, and 700°C for 1 h were shown in figure 3. All diffraction peaks can be confirmed to be the tetragonal rutile

phase of SnO₂, which is in good agreement with the reference pattern of SnO₂ (JCPDS No. 41-1445). In the presence of the pulp, the diffraction peak for sample calcined at 600°C (line (a)) was broadest as compared to other patterns, suggesting relatively crystallites. As a comparison with the same calcination temperatures in the absence of the pulp, the diffraction peak (line (d)) was sharper, suggesting relatively larger crystallites than SnO₂ diffraction peak for sample calcined at 600°C with the pulp. As the calcination temperatures increased, all peaks sharpen and increased in intensity, indicating that the particles were more crystalline at higher calcination temperatures.

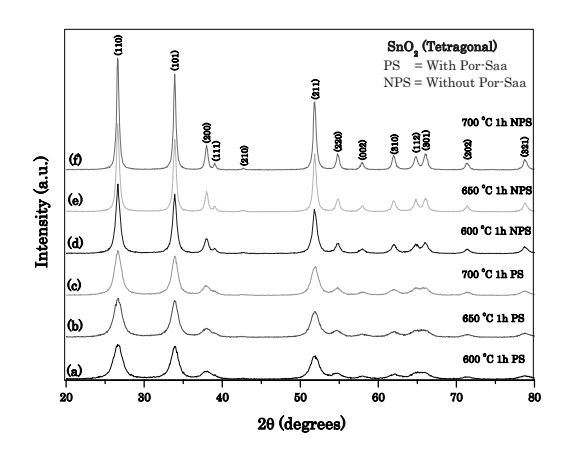
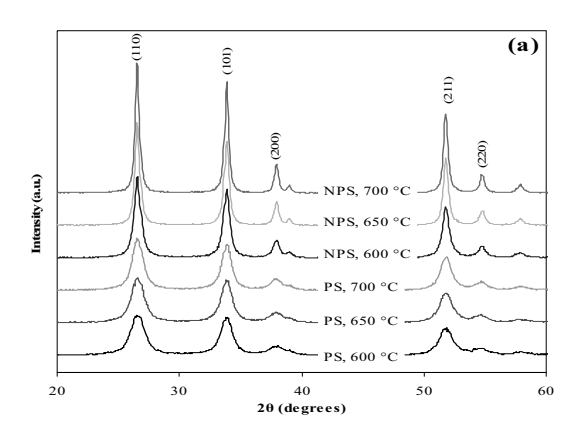


Fig. 3 X-ray diffraction patterns of SnO₂ nanoparticles calcined at (a) 600°C, (b) 650°C, and (c) 700°C for 1h with the presence and absence of the pulp as a dispersant.

Moreover, the (110) $(2\theta = 26.60)$, (101) $(2\theta = 33.98)$, (200) $(2\theta = 38.12)$, (211) $(2\theta = 51.92)$, and (220) $(2\theta = 54.80)$ peaks fitting were approached to obtain the particles size in the range of peak at $2\theta = 23.9-29.2$, 31.5-36.0, 37.0-38.7, 50.0-53.7, and 53.7-55.80, respectively as shown in figure 4 (a). It can be clearly seen in figures 4 (b) and (c) that the d_{XRD} average sizes calculated using conspicuous 5 peaks fitting were found to be almost the same range of 5-11 nm with the presence of the pulp and 14-30 nm with the absence of the pulp as a dispersant.

Figure 5 shows the comparison of SSA_{BET} and $d_{\rm BET}$ as a function of calcinations temperatures. It can be clearly seen that the trend of the particles size calculated by BET measurement using SSA_{BET} decreased with increasing the SSA_{BET} both with the absence of the pulp. presence and corresponding d_{XRD} was calculated conspicuous 5 peaks fitting with the fundamental parameter approach and Rietveld method as shown in figures 5 (a) and (b) and compared with d_{BET} average size. In presence and absence of the pulp, the range of particle sizes calculated was higher values than crystallite size as shown in figure 6. It can be assumed that the nanoparticles were rather agglomerated when degassing at 150°C. The BET powder-SSA of SnO₂ nanoparticles calcined at 600, 650, and 700°C were measured by nitrogen adsorption methodology after degassing the sample at 150°C, with the presence of pulp as a dispersant were 62.53, 59.20, and 49.94 m²/g, respectively. The SSA of the SnO₂ nanoparticles calcined at 600, 650 and 700°C with the absence of pulp was 26.60, 24.32, and 15.47 m²/g, respectively. From these data, it can be summarized that as the calcination temperature increased, the SSA gradually the larger decreased, indicating particles. Nevertheless, the accurate sizes were clearly confirmed by TEM bright-field images.



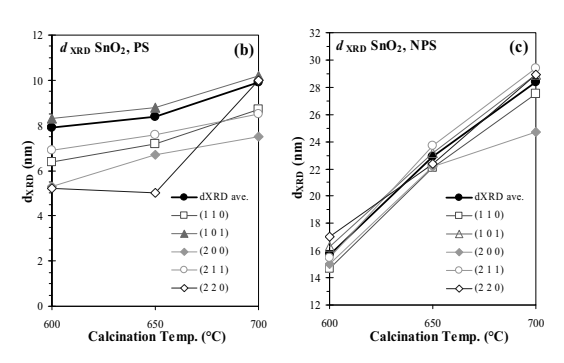


Fig. 4 (a) Crystallite size analysis of SnO_2 nanoparticles synthesized with the (b) presence and (c) absence the pulp as a dispersant. The corresponding average d_{XRD} sizes and the particles sizes calculated using the (110), (101), (200), (211), and (220) conspicuous (hkl) plane of XRD patterns were found to be almost in the same range.

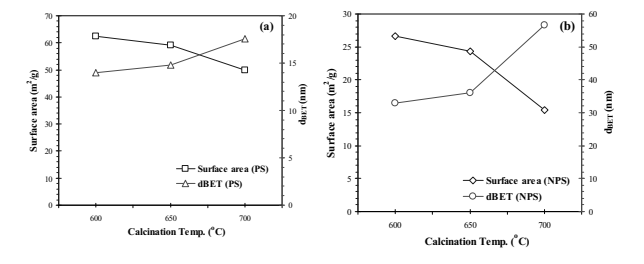


Fig. 5 The d_{BET} -dependent on SSA_{BET} of SnO_2 nanoparticles synthesized with (a) the presence and (b) absence of the pulp as a dispersant

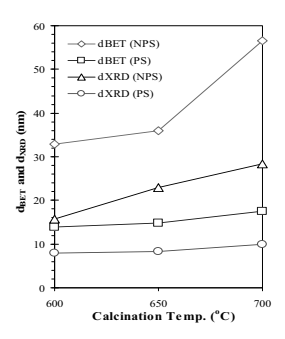
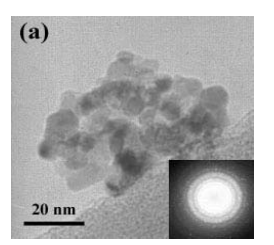
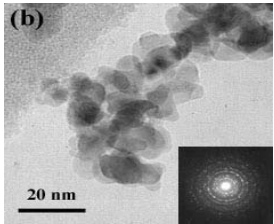


Fig. 6 Comparison of d_{BET} and d_{XRD} of SnO_2 nanoparticles synthesized with the presence (PS) and absence (NPS) of the pulp as a dispersant.

The accurate sizes of all samples were confirmed by TEM bright-fields images. Figures 7(a), (b), and (c) show the bright-field TEM images of the SnO₂ nanoparticles calcined at 600, 650, and 700°C, respectively using the pulp as the dispersant. Figure 8(a), (b), and (c) show brightfield TEM images of the SnO₂ nanoparticles calcined at 600, 650, and 700°C with the absence of The pulp, respectively. corresponding diffraction patterns are shown in the insets. All diffraction patterns illustrating the spot patterns of the tetragonal phase of SnO2 indicated that the SnO₂ nanoparticles are highly crystalline. This trend generally corresponds to the peaks which shown in the XRD patterns. In the presence of the pulp, SnO₂ nanoparticles calcined at 600°C were loosely agglomerated and well dispersed, and in the range of 5-10 nm in diameter. For the samples calcined at 650 and 700°C, the accurate sizes were clearly seen, and found to be in the range of 7-10 nm and 5-15 nm, respectively. For the absence of the pulp, the sample calcined at 600°C, the sizes of SnO₂ nanoparticles were found to be within the range of 5-15 nm. For the samples calcined at 650°C, better defined and rather dispersed crystals were observed, and it was found that the average particles sizes are ranging from 7-20 nm, and subsequently the samples which calcined at 700°C, the SnO₂ nanoparticles were highly crystalline as well corresponding to the XRD pattern and diffraction pattern, with diameters ranging from 10-30 nm. These studies demonstrated that the sizes of the SnO₂ nanoparticles increased with increasing calcination temperatures and were influenced by the pulp. The differentiability accurate sizes of the particles were clearly seen through out the same calcination temperatures. From these data, the particles sizes when observed from the TEM bright- field images (d_{TEM}) corresponded with average d_{XRD} calculated from the peaks fitting based on the Sherrer's equation.





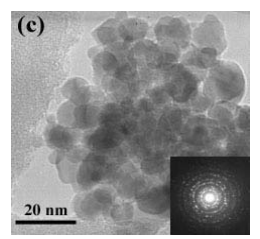
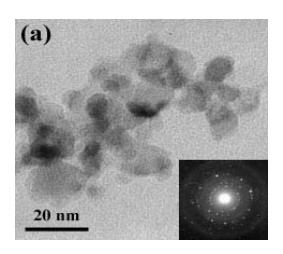
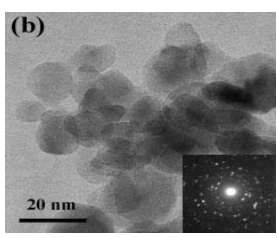


Fig. 7 TEM bright-field images of crystalline $\rm SnO_2$ nanoparticles calcined at (a) 600°C, 650°C, and (c) 700°C for 1h synthesized with the presence of the pulp as a dispersant. Insets show the corresponding diffraction patterns of the particle, which confirmed to the tetragonal phase and crystallinity.





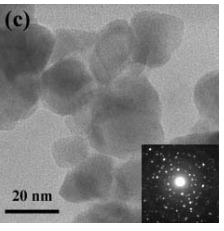


Fig. 8 TEM bright-field images of crystalline $\rm SnO_2$ nanoparticles calcined at (a) 600°C, (b) 650°C, and (c) 700°C for 1h synthesized with the absence of the pulp as a dispersant. Insets show the corresponding diffraction patterns of the particles, which confirmed to the tetragonal phase and crystallinity.

Conclusion

With the presence and absence of *Broussonetia* papyrifera (L.) Vent pulp as the dispersant, SnO₂ nanopowders were successfully prepared by the precipitation and thermal decomposition methods. The morphology and elemental compositions of the pulp were analyzed by LV-SEM and EDS elemental mapping. The resulting nanopowders were analyzed by XRD, BET, and TEM. The XRD patterns showed that the particles corresponded to the tetragonal rutile phase of SnO₂. The SSA_{BET} of nanopowders decreased with increasing calcination temperatures, and also depended on the presence or the absence of the pulp as a dispersant. In the presence and absence of the pulp, the accurate sizes of the SnO₂ nanoparticles were clearly observed by

TEM bright-field images and found to be in the range of 5-15 nm, and 5-30 nm, respectively. It can be clearly seen that the particles sizes increased with increasing calcination temperature and were influenced by the pulp as the dispersant. Therefore, the morphology and size of the SnO₂ nanoparticles can be controlled using the pulp as the dispersant and calcination temperatures. This present study showed a relatively simple co-method to control the morphology and sizes of the SnO₂ nanoparticles by using the pulp as the dispersant and the appropriate calcination temperatures.

Acknowledgment

The authors gratefully acknowledge the financial support from the Chiang Mai University Graduate School; Center for innovation in Chemistry: Postgraduate Education and Research Program in Chemistry (PERCH-CIC); The National Nanotechnology Center (NANOTEC), NSTDA, Ministry of Science and Technology, through its program of Center of Excellence Network; The Nanoscience Research Laboratory (NRL), Department of Chemistry, Faculty of Science and Chiang Mai University, Thailand. The special thanks should be given to Mrs. Boosabong Kanthalue for LV-SEM facilities and TEM.

- Pang, G.; Chen, S.; Koltypin, Y.; Zaban, A.; Feng, S.; Gedanken, A. Controlling the particle size of calcined SnO₂ nanoparticles. *Nano Lett.* 2001, 1: 723-726.
- Skála, T.; Veltruská K.; Moroseac, M.; Matolínová, I.; Cireca, A.; Matilín V. Redox process of Pd-SnO₂ system. Surf. Sci. 2004, 566-568: 1217-1221.
- 3. Tsang, S. C.; Bulpitt, C. D. A.; Mitchell P. C. H.; Ramirez-Cuesta, A. J. Some new insights into the sensing mechanism of palladium promoted Tin (IV) Oxide sensor. *J. Phys. Chem. B* 2001, 105: 5737-5742.
- 4. Feng, Y.; Yao, R.; Zhang, L. Synthesis and sensitivity properties of Pd-doped tin oxide nanoparticles dispersed in mesoporous silica. *Mater. Chem. Phys.* 2005, 89: 311-314.
- Morales, J.; Sáncez, L. Electrochemical behaviour of SnO₂ doped with boron and indium in anodes for lithium secondary batteries. Solid State Ionics 1999, 126: 219-226.
- 6. Yang, H.; Hu, Y.; Tang, A.; Jin, S.; Qiu, G. Synthesis of tin oxide nanoparticles by mechanochemical reaction. *J. Alloys Compd.* 2004, 363: 271-274.
- Amalric-Popescu, D.; Bozon-verduraz, F. Infrared studies on SnO₂ and Pd/SnO₂. *Catal. Today* 2001, 70: 139-154.
- 8. Kőrösi, L.; Papp S.; Meynen, V.; Cool P.; Vansant, E. F.; Dékány I. Preparation and

- characterization of SnO₂ nanoparticles of enhanced thermal stability: The effect of phosphoric acid treatment on SnO₂ nH2O. *Colloids Surf.*, A 2005, 268: 147-154.
- Ibarguen C. A.; Mosquera, A.; Parra, R.; Castro, M. S.; Rodríguez-Páez, J. E. Synthesis of SnO₂ nanoparticles through the controlled precipitation route. *Mater. Chem. Phys.* 2007, 101: 433-440.
- 10. Ahmed, J.; Vaidya, S.; Ahmad, T.; Devi, P. S.; Das, D.; Ganguli, A. K. Tin dioxide nanoparticles: Reverse micellar synthesis and gas sensing properties. *Mater. Res. Bull.* 2007, In press.
- 11. Cukrov, L.M.; Tsuzuki, T.; McCormick, P.G. SnO₂ nanoparticles prepared by mechanochemical processing. *Scripta Mater*. 2001, 44: 1787-1790.
- 12. Gu, F.; Wang, S.F.; Song, C.F.; Lü, M.K.; Qi, Y.X.; Zhou, G.J.; Xu, D.; Yuan, D.R. Synthesis and luminescence properties of SnO₂ nanoparticles. *Chem. Phys. Lett.* 2003, 372: 451-454.
- 13. He, Y.; Li, Y.; Yu, J.; Qian, Y. Chemical control synthesis of nanocrystalline SnO₂ by hydrothermal reaction. *Mater. Lett.* 1999, 40: 23-26.
- Toledo-Antonio, J.A.; Baez, R.G.; Sebastian, P.J.; Vázquez, A. Thermal stability and structural deformation of rutile SnO₂ nanoparticles. *J. Solid State Chem.* 2003, 174: 241-248.
- 15. Melghit, K.; Mohammed, A. K.; Al-Amri, I. Chimie douce preparation, characterization and photocatalytic activity of nanocrystalline SnO₂. *Mater. Sci. Eng., B* 2005, 117: 302-306.
- 16. Acarbaş, Ö.; Suvaci, E.; Doğan, A. Preparation of nanosized tin oxide (SnO₂)

- powder by homogeneous precipitation. *Ceram. Int.* 2007, 33: 537-542.
- Erkan, A.; Bakir, U.; Karakas, G. Photocatalytic microbial inactivaion over Pd doped SnO₂ and TiO₂ thin films. *J. Photochem. Photobiol.*, A 2006, 184: 313-321.
- 18. Wang, C.; Xu, B. Q.; Wang, X.; Zhao, J. Preparation and photocatalytic activity of ZnO/TiO₂/SnO₂ mixture. *J. Solid State Chem.* 2005, 178: 3500-3506.
- Hülser, T.P.; Wiggers, H.; Kruis, F.E.; Lorke, A. Nanostructured gas sensors and electrical characterization of deposited SnO₂ nanoparticles in anbient gas atmosphere. Sens. Actuators, B 2005, 109: 13-18.
- Diéguez, A.; Romano-Rodríguez, A.; Morante, J.R.; Weimar U.; Achweizer-Berberich, M.; Göpel, W. Morphological analysis of nanocrystalline SnO₂ for gas sensor applications. Sens. Actuators, B 1996, 31: 1-8.
- Menezes, D. C.; Lima, G. M.; Porto, A.O.; Donnici, C. L.; Ardisson, J. D.; Doriguetto, A. C.; Ellena, J. Preparation and characterization of SnO₂ nanorods by thermal decomposition of SnC₂O₄ precusor. *Polyhedron* 2004, 23: 2103-2109.
- Liewhiran, C.; Seraphin, S.; Phanichphant, S. Synthesis of nano-sized ZnO powders by thermal decomposition of zinc acetate using (.L) *Broussonetia papyrifera* Vent pulp as a dispersant. *Curr. Appl. Phys.* 2006, 6: 499-502.
- Benson, L. Plant Classification; D. C. Heath, Massachusetts 1959.

Effect of Ru on Photocatalytic Activity of TiO₂ Nanoparticles

K. Wetchakun 1* and S. Phanichphant 2,3

Abstract

Pure ${\rm TiO_2}$ was synthesized by the modified sol-gel method. Titanium tetraisopropoxide (TTIP) precursor was mixed with absolute ethanol. The mixture was loaded into a pouch type cellophane membrane. The membrane pouch was placed in the solution of absolute ethanol containing with 1:1 (v/v) ratio and then distilled water with 0.5-1.0 % concentrated ammonia solution for 1h. The mixture was dried at 100 °C for 48 h. Finally, the powders was calcined at 400 °C for 3 h. Ru-doped ${\rm TiO_2}$ with metal loading of 0.1, 0.2, 0.5, 1.0 and 2.0 at.% were synthesized by impregnation method. Phase composition of Ru-doped ${\rm TiO_2}$ was examined by X-ray Diffraction (XRD), Scanning Electron Microscopy (SEM) and Transmission Electron Microscopy (TEM). The photocatalytic activities of Ru-doped ${\rm TiO_2}$ samples were evaluated by studying the mineralization of sucrose, glucose, oxalic acid and formic acid under UVA irradiation.

Background

The degradation of organic pollutants in water by photocatalysis, using the wide optical band gap material (TiO₂), has attracted extensive attention during recent 20 years [1]. Titanium dioxide is widely used as a semiconductor photocatalyst in light of the fact of its long term stability, no good photocatalytic toxicity and activity. Futhermore, it is well known that nanometer-sized anatase particles with high crystallinity have a high photocatalytic activity [2,3]. However, there is still a problem that photocatalytic efficiency is not high because recombination of photogenerated electronhole pairs influences low photo quantum efficiency. In recent years, metalization of TiO₂ by noble metal has been extensively investigated as a technique to increase the quantum efficiency of TiO₂ for the fermi levels of these noble metals are lower than that of TiO2, while photo-generated VB holes remain on the TiO2. These activities greatly reduce the possibility of electron-hole recombination, resulting in efficient separation and stronger photocatalytic reactions [4,5]. Moreover, the activity of TiO2 is influenced by several factors such as crystallinity of anatase phase, particles size, surface area and the method of preparation [6].

Noble metals, including Pt, Au, Pd and Ag, have been reported to be very effective for enhancement of TiO₂ photocatalysis [5]. Accordingly, we expected Ru that is one of noble metal can also increase ability of TiO₂ photocatalysis as last research with regard to Rudoped TiO₂ catalysts following Ranjit et al. [7] who reported that Ru-loaded TiO₂ catalysts can be

advantageously used for hydrogenation/ photocatalytic reduction of nitrite and nitrate ions to ammonia. Sasirekha et al. [8] showed that TiO₂ particles with Ru ions have higher photocatalytic activity than pure TiO₂ and the optimum Ru loading was found to be 0.5 wt.%. The driving force may be the separation of charge carriers due to the formation of schottky barrier. Jin et al. [9] demonstrated that dye-sensitized M/TiO₂ (M = Pt, Ru and Rh) could be used as photocatalysts for hydrogen production from a DEA-H₂O mixture with high quantum efficiencies and had good stability under visible light irradiation in the presence of electron donors. triethanolamine, acetonitrile and triethylamine, etc.

In this research study, we use Ru-doped TiO_2 in order to degrade organic pollution. TiO_2 nanoparticles and Ru-doped TiO_2 were synthesized using the modified sol-gel method and impregnation method, respectively. The photocatalytic activities of samples were evaluated by studying the mineralization of sucrose, glucose, oxalic acid and formic acid under UVA irradiation.

Materials and Methods

Synthesis of Pure TiO₂

Pure TiO_2 nanopowders were synthesized from titanium tetraisopropoxide (TTIP) in absolute ethanol by the modified sol-gel method. The mixture of TTIP and absolute ethanol was loaded into a pouch type cellophane membrane and placed in a clear solution containing 1:1 (v/v) ratio of absolute ethanol and distilled water with 0.5-1.0 %

¹ Department of Physics, Faculty of Science, Chiang Mai University, Chiang Mai 50200, Thailand

² Department of Chemistry, Faculty of Science, Chiang Mai University, Chiang Mai 50200, Thailand

³ NANOTEC Center of Excellence at Chiang Mai University, Chiang Mai 50200, Thailand e-mail: to khatcharin@hotmail.com

concentrated ammonia solution for 1h. After the dialysis process was complete, the mixture was then dried in an oven at $100~^{\circ}\text{C}$ for 48 h. The powder was finally calcined in an oven at a temperature of $400~^{\circ}\text{C}$ for 3 h.

Preparation of Ru-doped TiO₂

Ru-doped TiO_2 with metal loading amount of 0.1, 0.2, 0.5, 1.0 and 2.0 at.% were prepared by impregnation method. Ruthenium acetylacetonate was dissolved in toluene and the solution was, then pipeted into TiO_2 nanoparticles. The resulting slurry was continuously stirred at room temperature and dried in an oven at 80 °C for 24 h. The solid obtained after drying was crushed and calcined in air at 400 °C for 3 h.

Characterization Methods

X-ray diffraction (XRD) patterns of pure TiO_2 and Ru-doped TiO_2 were obtained from a diffractometer using Cu K_α radiation over the scan range of 2θ between $10\text{-}90^\circ$.

The surface morphology of all the catalysts was observed by scanning electron microscope (SEM). Catalysts were dispersed in ethanol and the suspension was dropped onto the copper tape. The specimen was then coated with gold using sputtering technique and examined under JEOL JSM-6335F coupled with an energy dispersive spectroscopy (EDS) accessory.

The topography and particle size of Ru-doped ${\rm TiO_2}$ was measured using JEOL JEM-2010 transmission electron microscopy (TEM). Before the analysis, the catalyst sample ultrasonically dispersed in a solvent and dropped on a copper grid. The sample was allowed to dry before TEM analysis.

Photocatalytic Eexperiments

A 50 mL photocatalyst of (1 g/L) was prepared and its pH was adjusted to 3.0 by using 0.1 M perchloric acid. The suspended particles were dispersed in an ultrasonic bath for 20 min before charging into the spiral photoreactor. The photocatalytic activity of the prepared samples was compared on the basis of the rate of carbon dioxide generation or mineralization. Commercially available Degussa P25 (predominantly anatase with a specific surface area of 50 m²/g) was designed as a benchmark for comparison study. The carbon dioxide generated from the mineralization of sucrose, glucose, oxalic acid and formic acid was determined from a calibrated conductivity meter. Oxidation experiments were carried out by illuminating the system with an ultraviolet in the presence of the photocatalyst.

Results and Discussion

Characterization of Ru-doped TiO₂

The crystallinity of the prepared samples was examined by XRD analysis. XRD patterns of pure and 0.1, 0.2, 0.5, 1.0 and 2.0 at.% Ru-doped TiO2 were shown in figure 1. The 2θ values of peaks confirmed that the particles polycrystalline with an anatase structure (JCPDS, No. 86-1157) corresponding to the diffractions of (101), (004), (200), (105), (211), (204), (116), (220), (215) and (224), respectively. It was observed that the XRD patterns of the all doped sample showed no signals originated the presence of doped metal. The absence of metal peaks could come from their ultra fine dispersion on TiO2 particles as very small clusters or due to very low metal content.

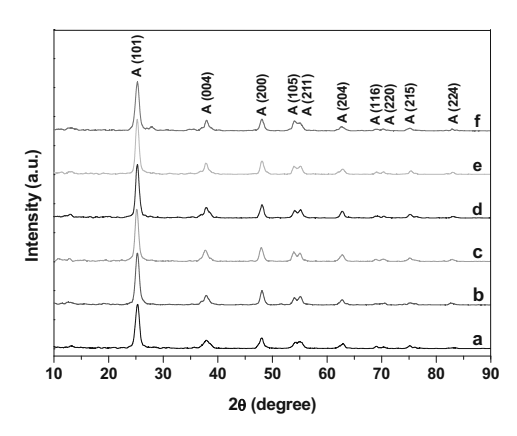


Fig. 1 XRD patterns of (a) TiO₂, (b) 0.1 at.% Ru/TiO₂, (c) 0.2 at.% Ru/TiO₂, (d) 0.5 at.% Ru/TiO₂, (e) 1.0 at.% Ru/TiO₂ and (f) 2.0 at.% Ru/TiO₂.

The surface morphology of sample was examined by SEM and figure 2 illustrates a SEM micrograph and EDS analysis of 0.1, 0.5 and 1.0 at.% Ru/TiO2. Ru-doped TiO2 was observed as spherical aggregates of small sub-particles. Clusters of the synthesized catalysts have sizes in the range of 0.1-1.0 µm. Figure 3 shows subparticles size of 0.1 at.% Ru/TiO₂ less than 100 nm that was confirmed by TEM micrographs shown in figure 4. EDS analysis provides information on chemical comparison of samples. Figure 2 shows that the prepared sample is mainly composed of Ti and O with a trace amount of Ru that increases with an increase number of loading. Ru L peak was found but peak of Ru K can not be detected because low electron accelerating voltage was applied.

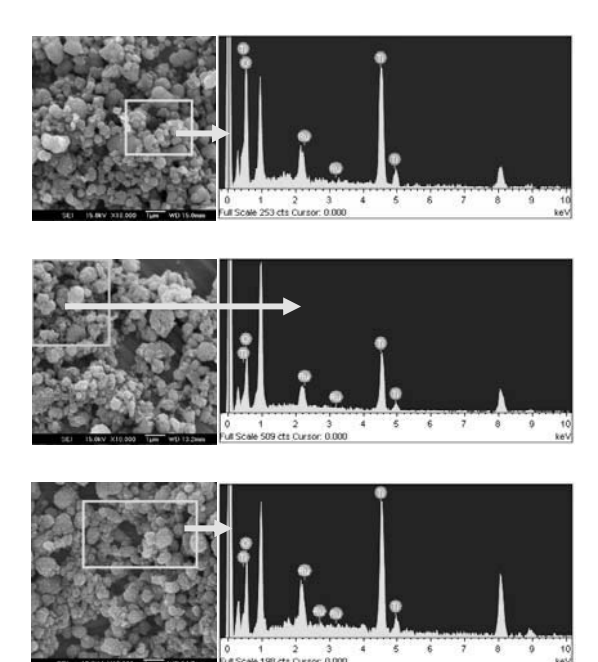


Fig. 2 SEM micrographs and EDS analysis of (a) 0.1 at.% Ru/TiO₂, (b) 0.5 at.% Ru/TiO₂ and (c) 1.0 at.% Ru/TiO₂.

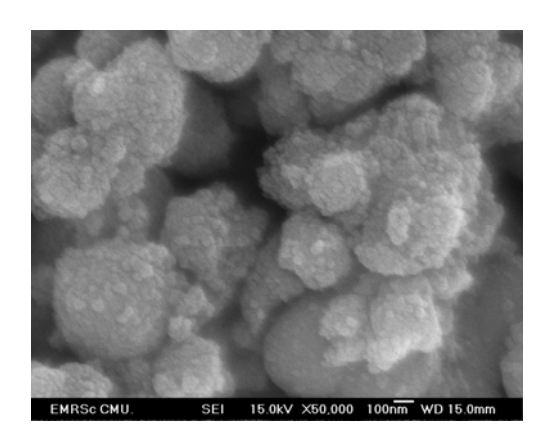


Fig. 3 SEM micrograph of 0.1 at.% Ru/TiO₂ at \times 50,000 magnification.

The crystal morphology of the particles as shown in figure 4 exhibited rectangle shape in agreement with the tetragonal crystal structure of the particles indicated by the XRD result. Even though no direct evidence for Ru phase occurrence can be observed from the SEM micrograph, Ru was directly observed by TEM micrograph for 2.0 at.% Ru/TiO₂ as shown in figure 4 (c) in circle dash line. However, Ru phase did not appear in the TEM micrograph of 0.1 at.% Ru/TiO2 shown in figure 4 (b) because too little content of Ru loading. The TEM micrograph of pure TiO₂ is shown in figure 4 (a). An average crystallite size of TiO2 is approximately 12 nm. Diffraction patterns of pure TiO₂, 0.1 at.% Ru/TiO₂ and 2.0 at.% Ru/TiO₂ demonstrated that these samples polycrystalline materials.

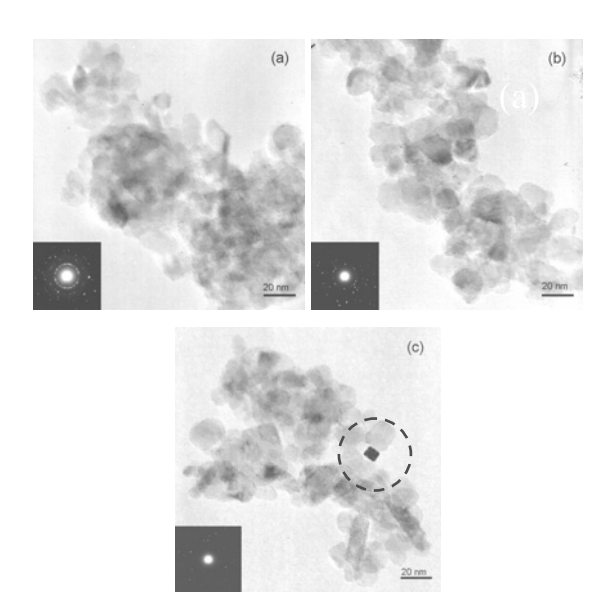


Fig. 4 TEM micrographs of (a) Pure TiO_2 , (b) 0.1 at.% Ru/TiO_2 and (c) 2.0 at.% Ru/TiO_2 .

Photocatalytic activity studies

The photocatalytic activities of the Ru/TiO₂ samples, TiO₂ and Degussa P25 were evaluated by mineralization of sucrose, glucose, oxalic acid, and formic acid under UVA irradiation as shown in figure 5. All Ru/TiO₂ revealed higher photoactivity than pure TiO2 in mineralizing formic acid and oxalic acid may be due to Ru deposition on the surface of TiO2 and acted as active sites of the photocatalytic reaction and may favour separating efficiently, charge carrier inhibiting recombination of electron-hole pairs, ultimately causing the enhancement of the reactivity [7]. P25 and pure TiO₂ showed higher photoactivity than all Ru/TiO2 based on the fact that the efficiency of the noble-metal modified photocatalytic process was strongly dependent on the nature of the substrates followed Husfschmidt et al. (2002) research as it is important to investigate whether the modified catalyst is suitable for the photodegradation of the investigated substrates [4]. The optimum content of Ru loading for formic acid and oxalic acid degradation is 0.1 at.% Ru/TiO₂.

Conclusion

Pure TiO₂ and Ru-doped TiO₂ have been successfully prepared by the modified sol-gel and the impregnation methods, respectively. The XRD patterns of synthesized catalysts indicate anatase crystal structure. The EDS analysis and TEM micrograph shows that the existence of Ru in TiO₂. Under UVA-illumination, it was found that TiO₂ doped with 0.1 at.% Ru shows the highest activity for mineralizing formic acid.

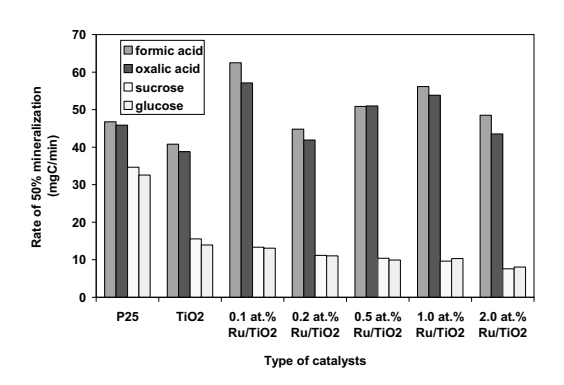


Fig. 5 Mineralization of oxalic acid, formic acid, sucrose and glucose 500 μg of carbon using Degussa P25, pure TiO₂ and 0.1-2.0 at.% of Ru/TiO₂ under UVA irradiation.

Acknowledgment

The authors would like to thank Nanoscience Research Laboratory, Department of Chemistry, Faculty of Science, Chiang Mai University; Graduate School, Chaing Mai University; The National Nanotechnology Center (NANOTEC), NSTDA, Ministry of Science and Technology, through its program of Center of Excellence Network, Thailand.

- Li, X.Z., Li, F.B., Yang C.L. and Ge W.K., Photocatalytic activity of WO_x-TiO₂ under visible light irradiation. *J. Photochem. Photobiol. A: Chem.* 2001, 141: 209-217.
- Yang, Y., Li, X.-J., Chen, J.-T. and Wang , L.-Y., Effect of doping mode on the photocatalytic activities of Mo/TiO₂. *J. Photochem. Photobiol. A: Chem.* 2004, 163: 517-522.
- 3. Baiju, K.V., Sibu, C.P., Rajesh, K., Krishna Pillai, P., Mukundan, P., Warrier, K.G.K. and Wunderlich, W., An aqueous sol–gel route to synthesize nanosized

- lanthana doped titania having an increased anatase phase stability for photocatalytic application. *Mater. Chem. Phys.* 2005, 90: 123–127.
- 4. Timothy, T. Y., Photocatalytic Reduction of Selenate and Selenite: Water/Wastewater Treatment and The formation of Nano-Selenium Compounds, A thesis for the degree of Doctor of Philosophy, The University of New South Wales, 2003, 27-30.
- Ni, M., Leung, M.K.H., Leung, D.Y.C. and Sumathy, K., A review and recent developments in photocatalytic watersplitting using TiO₂ for hydrogen production. *Renew. Sustain. Energy Rev.* 2007, 11: 401–425.
- Senthilkumaar, S., Porkodi, K., Gomathi, R., Maheswari, A. G. and Manonmani, N., Sol-gel derived silver doped nanocrystalline titania catalysed photodegradation of methylene blue from aqueous solution. *Dyes Pigments*. 2006, 69: 22-30.
- Ranjit, K.T., Varadarajan, T.K. and Viswanathan, B., Photocatalytic reduction of nitrite and nitrate ions on Ru/TiO₂ catalysts. *J. Photochem. Photobiol. A:* Chem. 1995, 89: 67-68.
- 8. Sasirekha, N., Basha, S.J.S. and Shanthi, K., Photocatalytic performance of Ru doped anatase mounted on silica for reduction of carbon dioxide. *Appl. Catal. B: Environ.* 2006, 62: 169–180.
- Jin, Z., Zhang, X., Lu, G. and Li, S., Improved quantum yield for photocatalytic hydrogen generation under visible light irradiation over eosin sensitized TiO₂—Investigation of different noble metal loading. *J. Mol. Catal. A:* Chem. 2006, 259: 275–280.

Surface Image of Charcoal and Activated Charcoal from Banana Peel

S. Mopoung

Department of Chemistry, Faculty of Science, Naresuan University, Phitsanulok, Thailand e-mail: sumritm@nu.ac.th

Abstract

In this research, the results of the SEM morphology and XRD pattern studies of charcoals and activated charcoals prepared from banana peel are used to describe the effects of pyrolysis temperature and the mass ratios of KOH. In the carbonization process, banana peel charcoal carbonized at 300° C to 400° C has incomplete carbonization and the cell structure is maintained. Complete pore evolution occurred at temperatures of 500° C. The surface image of activated carbon from banana peel charcoal obtained at a pyrolysis temperature between 500° C and 700° C and with mass ratios between 1:2 and 1:5 showed increased porosity with increasing temperature. Increase KOH ratios slightly raised the pore size and porosity of activated charcoals. The change of pyrolysis temperature from 500° C to 700° C for ratios ranging between 1:2 and 1:4 has a big effect on the pore size. However, the 1:5 ratio of activated charcoal suppressed the pore size. This result showed that the over KOH ratio resulted in an insulating layer, covering the particles of banana peel charcoal. The XRD pattern showed that the constituents of banana peel activated charcoal were probably graphite, amorphous C, amorphous SiO₂, K₂O, K and K₂CO₃.

Background

Organic matter may be converted by controlled decomposition into carbon. mechanisms involved in the conversion of organic matter to carbon are: (1) desorption of adsorbed water up to 150°C, (2) splitting of matter structure water between 150°C and 260°C, (3) chain scissions, or depolymerization, and breaking of C-O and C-C bonds within ring units evolving water, CO and CO₂ between 260°C and 400°C, (4) aromatization forming graphitic layers above 400°C, and (5) above 800°C, the thermal induced decomposition and the rearrangement reaction are almost terminated leaving a carbon template structure. The major components of organic matter break down in a stepwise manner at 200-800°C (hemicellulose), 260-350°C (cellulose) and 280-500°C (lignin). Between 260°C and 400°C almost 80% of the total weight loss occurs which may vary between 40% (lignin) to about 80% (cellulose) due to evolution of H₂O, CO₂, and volatile hydrocarbon species from fragmentation reactions of the polyaromatic constituents [1]. Chemical activation of carbons is a very common method for obtaining activated carbons with very high surface areas. KOH is one of the most effective agents employed for organic materials. KOH might be more selective in the activation process, causing a more localized reaction with the carbon precursor and is more effective for the highly ordered materials [2]. Thus, it can be stated that direct KOH activation of a lignocellulosic material is not necessarily an advantage [2]. The temperatures of pyrolysis and activation are considered to be the most important parameters controlling the activated carbon

production. There are many precursors from which activated carbons can be obtained. The use of organic materials for activated carbon is common. These materials are obtained as by-products of the agricultural and food industries and, hence, they are cheap and their use contributes to the conservation of the environment [3]. Banana peels are a solid waste from finished food products, such as chips, slices, and dried banana. They are high organic carbon (41.37%). This waste has been subjected to biomethanation [4] and biogas production [5].

The banana peel charcoals have been prepared by carbonization at 300-700°C. It was found that the percentage of charcoal from banana peel was decreased with the increase of carbonization temperature. However, the percentage of fixed carbons was reversed. The maximum of iodine numbers of charcoal from banana peels were found to be at the carbonized temperature of 500°C. The charcoals of banana peels with carbonization at 500°C were activated with KOH in ratios of 1:2 to 1:5 by weight. Then, these activated charcoals were recarbonized at 600° to 900°C. The iodine number of activated charcoals increased with increasing ratios of KOH, but the ethylene blue absorptions were increased a little [6]. These results suggest that activated carbons prepared from banana peel using KOH activation may be developed for adsorbents.

In this study, the results of the SEM morphology and XRD pattern studies of charcoals and activated charcoals prepared from banana peel are used to describe the effects of pyrolysis temperature and the mass ratios of KOH.

Materials and Methods

Preparation of Charcoals and Activated Charcoals

Banana peel as the precursor material was obtained from the Banggrathum district. Phitsanulok, Thailand. It was well washed with H₂O several times and used after oven drying at 110°C for 3 h. The dried sample was used for charcoal and activated charcoal preparation. The charcoal was prepared by a carbonized temperature of 300°C to 600°C for 1 h under a closed system in a porcelain crucible and then cooled to room temperature. The charcoal was then subjected to KOH activation. The charcoal was agitated in KOH (CARLO ERBA Reagent) at a ratio of 1:2, 1:3, 1:4 and 1:5) charcoal: KOH) weight by weight basis. After the agitation was finished, the pre-carbonized charcoal slurry was left overnight at room temperature and, then, dried at 110°C for 24 h. The samples were then activated in a closed system. Consequently, the samples were heated to optimize temperatures of 500, 600 and 700°C and maintained at a constant temperature for 1 h before cooling. After cooling down, the activated charcoal was washed successively several times with 0.2 N HCl (AR Merck), then with hot water until the pH became neutral, and finally with cold water to remove the excess KOH compounds. The washed samples were dried at 110°C to get the final product. The charcoal and activated charcoal were characterized by SEM and XRD.

Surface Morphology

Scanning electron microscopy was used to visualise the surface morphology of the charcoal and activated charcoal samples. A LEO 1455 VP scanning electron microscope was used. The samples were coated with gold by a gold sputtering device for a clear visibility of the surface morphology.

XRD Analysis

X-ray diffraction (XRD) was measured on a PW 3040/60, X' Pert Pro MPD X-ray diffractometer to determine the crystalline phases formed in banana peel activated charcoal.

Results and Discussion

Influence of Carbonized Temperature on the Development of Porosity of Charcoal

In the carbonization process, the development of porosity of banana peel charcoal starts at 300°C and increases with increasing carbonized temperature (figures 1 (a) - (d)). Figures 1 (a) and (b) show a pore and a cellular structure of banana peel charcoals which was carbonized at 300°C to

400°C. A temperature of 300°C to 400°C led to incomplete carbonization of banana peel and the cell structure is maintained. There are some rudimentary pores due to the release of volatiles. Evident pore evolution occurred in carbonization temperatures of 500°C. Raising the temperatures from 500°C to 600°C has a good influence on the banana peel with the generation moderately developed for charcoal production and shows characteristics open cellular structure in the original banana peel (figures 1 (c) and (d)). It can also be seen that the distribution of the open pores is uniform and forms a honeycomb structure. The scanning electron micrograph of charcoal (figures 1 (c) and (d)) clearly showed its complete porous structure and the opening of cell pores on the surface. The study of Mendez et al. [7] showed that the main important weight change of sewage sludges had been produced due to the light compounds volatilization and pyrolysis transformations at 450°C. This stage is primary pyrolysis (in the 300°C to 500°C range) with evolution of most gases and tars with formation of the basic structure of the char [8]. A temperature of 500°C was found sufficient for banana charcoal production. Therefore, considering economical and manufacturing factors, it was recommended the use of 500°C carbonization temperature for banana charcoal production. Thus, we selected banana charcoal carbonized at 500°C for subsequent KOH activation and characterization.

Influence of Activation Pyrolysed Temperature and Ratios of KOH on the Development of Porosity of Activated Charcoal

Figures 2-5 shows the surface images of activated carbon from banana peel charcoal obtained at pyrolysis temperature between 500°C and 700°C and mass ratios between 1:2 and 1:5. In this study it was established that the activated charcoal activated by KOH lost its original cellular structure and looked broken, therefore it was more fragmented during activation pyrolysis than carbonized charcoal. Generally, with the increase of activation temperature and the ratio of KOH, pore widening should occur. An increase in KOH ratio slightly raises the pore size and porosity of activated charcoals which is due to the aggressive action on the cellular structure, indicating that carbon gasification was enhanced by the increased KOH ratios.

By increasing the temperature from 500°C to 700°C and ratios of KOH from 1:2 to 1:5, the amount and size of porosity of activated charcoal increased. Increasing of the temperature raised the C-KOH reaction rate, resulting in an increased carbon burn-off. Concurrently, the volatiles from the charcoal continue to evolve with increasing activation temperature, whereas the C-KOH

reaction enhances the existing pores and creates new porosities [9]. The pore size depends on the banana charcoal: KOH ratios. Because the KOH reagent is a strong base, it is able to interact with carbon atoms and thus catalyze dehydrogenation and oxidation reaction, leading to the increment of tar evolution and development of porosity [10]. The change of pyrolysis temperature from 500-700°C for ratios ranges between 1:2 and 1:4 has a big effect on pore size. However, the 1:5 ratio of activated charcoal suppressed pore size. It is seen that the white sphere and some fluffy materials appear in the pores of activated charcoal (figures 2-5). The white spheres and fluffy materials may be due to the presence of K₂O, K₂CO₃ or K residues and increase with increasing ratios of KOH. It could be supposed that during the KOH activation process, various reactions can be considered with such products as H₂, K, K₂CO₃, and K₂O [11]. At higher temperature, the formation of K₂O is thermodynamically the most stable. The increase of KOH ratios on samples containing a large amount of potassium suggests that the high ratio KOH may give more K₂CO₃ and K₂O during pyrolysis. They were analyzed to be possibly either K₂CO₃ or K₂O from the corresponding EDS spectra (figure 6). Elemental analysis on the white point of activated charcoal shows that large amounts of K and O. The K₂CO₃ formation may not only occur on the outermost carbon surface, whereby K₂CO₃ forms a shell around the carbon and has no effect on the carbon structure, but also in the pores and cavities of the carbon where molten KOH could be located [3]. K₂CO₃ formed here would cause carbon lamellae separation, deformation and structure crumbling.

In the impregnated samples, increasing pyrolysis temperature at a constant impregnation ratio gives rise to an enhancement of the pore size. The same behavior was observed in activated carbon which ratios of KOH 1:2 to 1:4 (figures 2-4). It appears that a larger amount of K₂CO₃ formed causes a larger pores size and the structural deformation. However, the surface image of banana peel activated charcoal with KOH activation of ratio 1:5 (figure 5) showed smaller pore size than activated charcoal with ratios of KOH 1:2 to 1:4. It might be explained that the larger ratio of KOH probably forms an insulating layer, covering the particles, thus reducing the activation process and the contact with the surrounding atmosphere [8].

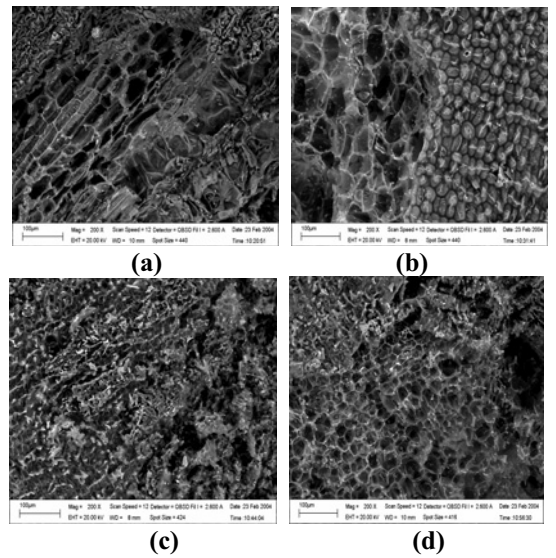


Fig. 1 Surface images of banana peel charcoal with carbonized temperature at (a) 300°C (b) 400°C (c) 500°C and (d) 600°C.

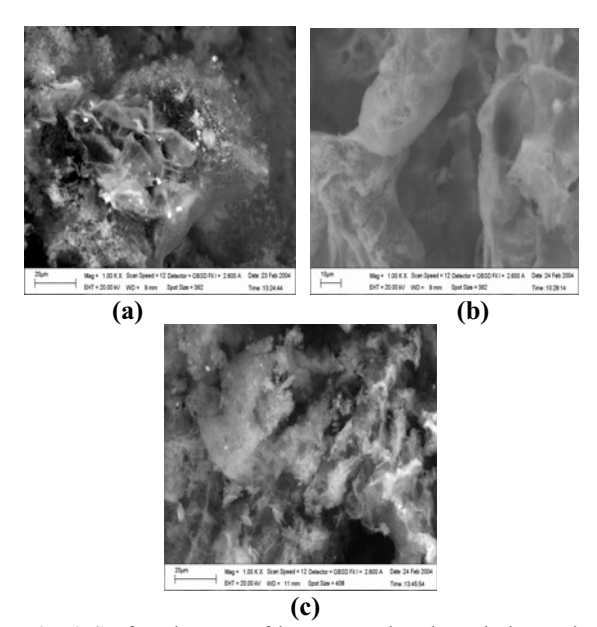


Fig. 2 Surface images of banana peel activated charcoal with KOH activation of ratio 1:2 and pyrolysed temperature at (a) 500°C (b) 600°C and (c) 700°C.

XRD Pattern of Banana Peel Activated Charcoal

Figure 7 illustrates the XRD pattern of the activated carbon prepared from banana peel with an activated temperature of 700°C. The activated carbon exhibited two peaks at around 20= 26° and 44° which correspond to the peak of graphite [9]. At the same time, it exhibits noise of the powder XRD signals. This reveals a predominantly amorphous structure of carbon. In this result, it can be explained that the pyrolytic reaction of organic compounds consists of the breaking of chemical bonds with temperature and repolymerization of radicals condensing further into active compounds. These compounds form typical graphitic layers and

stacks of planes during carbonization [12]. The XRD pattern showed that the compounds formed were probably K_2O and K_2CO_3 in the peaks of $2\theta = 28^\circ$, 31.4° and 42° . Formation of K_2CO_3 occurs by the reaction of KOH with CO_2 . The K_2O is left in the carbon as the end product [10]. The appearance of a broad peak at $2\theta = 24^\circ$ indicated that the silica in activated charcoal was amorphous SiO_2 .

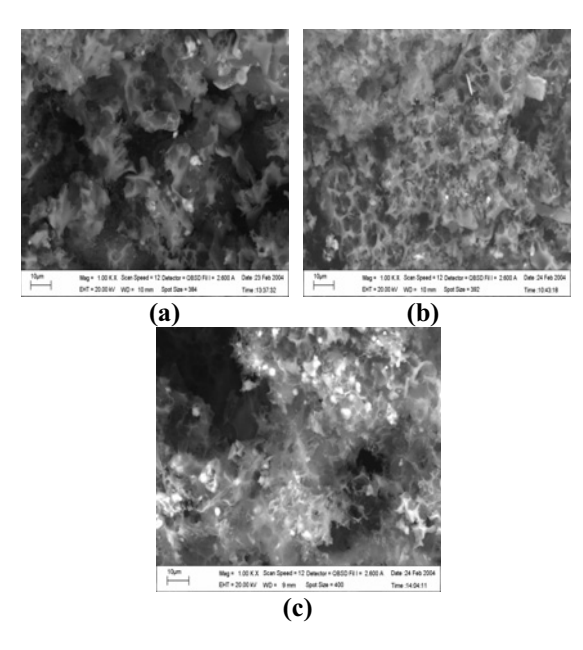


Fig. 3 Surface images of banana peel activated charcoal with KOH activation of ratio 1:3 and pyrolysed temperature at (a) 500°C (b) 600°C and (c) 700°C.

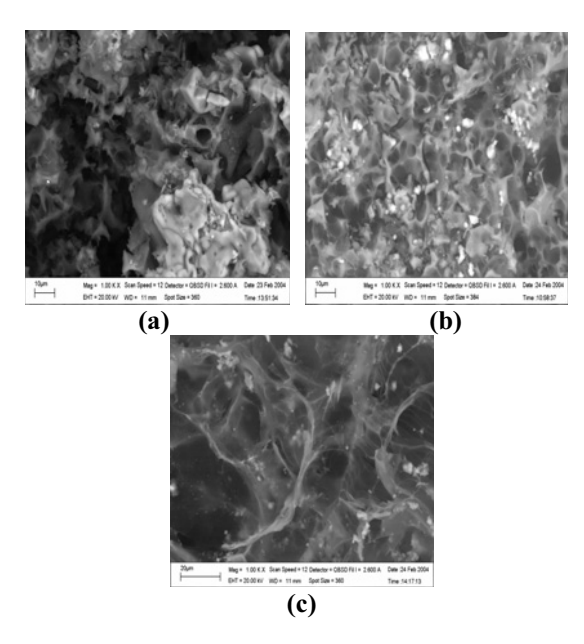


Fig. 4 Surface images of banana peel activated charcoal with KOH activation of ratio 1:4 and pyrolysed temperature at (a) 500°C (b) 600°C and (c) 700°C.

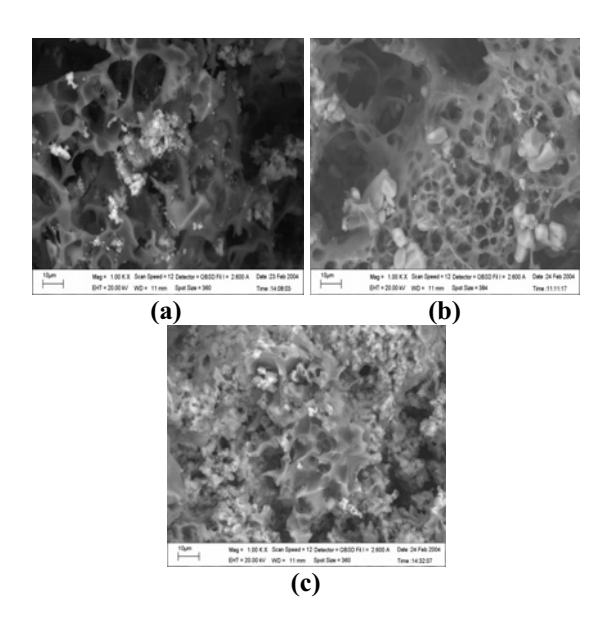
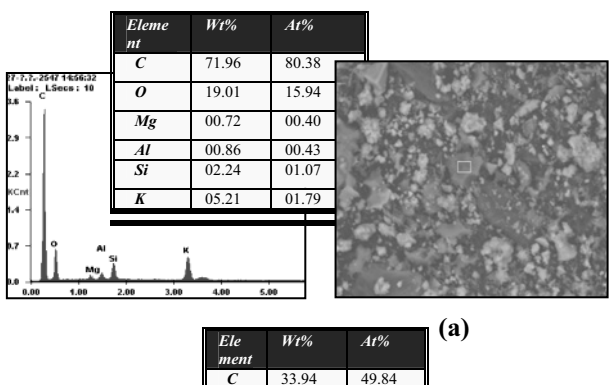


Fig. 5 Surface images of banana peel activated charcoal with KOH activation of ratio 1:5 and pyrolysed temperature at (a) 500°C (b) 600°C and (c) 700°C.



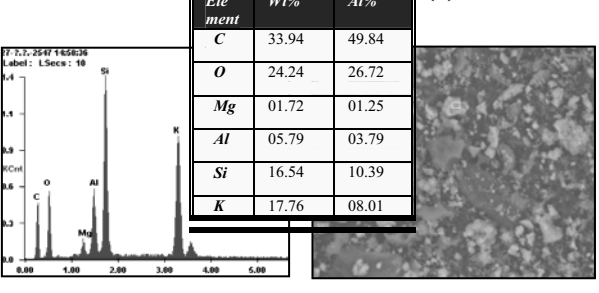


Fig. 6 SEM-EDS analysis of activated charcoal with activated KOH ratio of 1:5 and temperature at 700° C, (a) point on activated carbon granular (b) point on K_2 O granular.

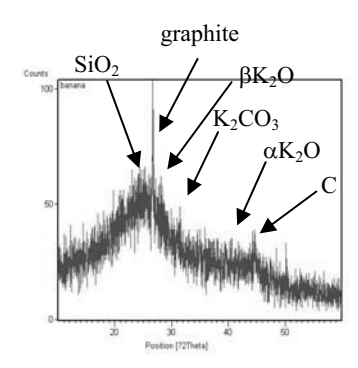


Fig. 7 XRD pattern of banana peel activated charcoal with pyrolysis at 700°C.

Conclusion

As the carbonization temperature increases, the resulting banana peel charcoal is better in clearly structure and ordering. Raising the temperatures from 500°C to 600°C has a good influence on the banana peel with generation of moderately developed charcoal production and shows characteristic due to open cellular structure in the original banana peel.

Increased KOH ratios slightly raises the pore size and porosity of activated charcoals which is due to aggressive action on the cellular structure, indicating that carbon gasification was enhanced by the KOH ratios increase to widen the pores.

The change of pyrolysis temperature from 500°C to 700°C for ratio ranges between 1:2 and 1:4 has a large effect on the pore size. However, the 1:5 ratio of activated charcoal suppressed the pore size. It is seen that the white sphere and some fluffy materials appear in the pores of activated charcoal. The white spheres and fluffy materials may be due to the presence of K₂O, K₂CO₃ or K residues and increase with increasing ratios of KOH. K₂CO₃ formed would cause carbon lamellae separation, deformation and structure crumbling. However, the surface image of banana peel activated charcoal with KOH activation of ratio 1:5 showed smaller pore size than activated charcoal which ratios of KOH 1:2 to1:4.

The XRD pattern showed that the constituents of banana peel activated charcoal were probably graphite, amorphous C, amorphous SiO_2 , K_2O , K and K_2CO_3 .

Acknowledgment

This research was supported by the Faculty of Science, Naresuan University and the National Research Council of Thailand. Instrumentation used in this research was purchased with partial funding from the Department of Chemistry, Faculty of Science, Naresuan University.

- 1. Qian, J.-M., Wang, J.-P., Qiao, G.-J., and Jin, Z.-H. Preparation of porous SiC ceramic with a woodlike microstructure by sol-gel and carbothermal reduction processing. *J. Eur. Ceram. Soc.* 2004, 24, 3251-3259.
- 2. Lillo-Rodenas, M.A., Marco-Lozar, J.P., Cazorla-Amoros, D., and Linares-Solano, A. activated carbon prepared by pyrolysis of mixtures of carbon precursor/alkaline hydroxide. *J. Anal. Appl. Pyrol.* 2007, 80, 166-174.
- 3. Diaz-Teran, J., Nevskaia, D.M., Fierro, J.L.G., Lopez-Peinado, A.J., Jerez, A. Study of chemical activation process of a lignocellulosic material with KOH by XPS and XRD. *Micropor. Mesopor. Mater.* 2003, 60, 173-181.
- 4. Bardiya, N., Somayaji, D., and Khanna, S. Biomethanation of banana peel and pineapple waste. *Bioresour. Technol.* 1996, 58, 73-76.
- 5. Mopoung, S., Udeye, V., Mopoung, R., Boonphong, S., O' Donnohuy, J., Production of biogas from banana peeling. *Nation. Res. Counc. Thail.* 2000, 432, 23-28.
- 6. Mopoung, S. Chemical composition and hysical properties of charcoal and activated charcoal from peel and bunch of banana. *NU Sci. J.* 2005, 2(1), 107-119.
- 7. Mendez, A., Gasco, G., Freitas, M.M.A., Siebielec, G., Stuczynski, T., and Figueiredo, J. Preparation of carbon-based adsorbents from pyrolysis and air activation of sewage sludges. *Chem. Eng. J.* 2005, 108, 169-177.
- 8. Girgis, B.S., and El-Hendawy, A.-N. A. Porosity development in activated carbons obtained from date pits under chemical activation with phosphoric acid. *Micropor. Mesopor. Mater.* 2002, 52, 105-117.
- 9. Lua, A.C., and Yang, T. Effect of activated temperature on the textural and chemical properties of potassium hydroxide activated carbon prepared from pistachio-nut shell. *J. Colloid. Interface. Sci.* 2004, 274, 594-601.
- 10. Hsu, L.Y., and Teng, H. Influence of different chemical reagents on the preparation of activated carbons from bituminous coal. *Fuel Process*. *Technol.* 2000, 64, 155-166.
- 11. Babel, K., and Jurewicz, K. KOH activated carbon fabrics as supercapacitor material. *J. Phys. Chem. Solid.* 2004, 65, 275-280.
- 12. Kurosaki, F., Ishimaru, K., Hata, T., Bronsveld, P., Kobayashi, E., and Imamura, Y. Microstructure of wood charcoal prepared by flash heating. *Carbon*, 2003, 41, 3057-3062.

Effect of pH on Phase Formation and Morphology of the Nanocrystalline Boehmite Powder Prepared by a Precipitation Method

R. Tipakontitikul¹, A. Niyompan^{1*}, K. Srisurat¹, N. Kanchanarat² and T. Tunkasiri³

e-mail: anuson@rocketmail.com

Abstract

Nanocrystalline boehmite, as a precursor for producing γ -Al₂O₃, was prepared using a precipitation method. Mixtures of alumina nitrate nanohydrate (Al(NO₃)₃·9H₂O) and sodium aluminate (Na₂Al₂O₄) solutions were aimed and the starting pH was set at a range of 6-9 to observe effect on morphology and phase formation. After the mixtures were kept at a temperature of 60 °C for 24 hr, nanocrystalline sized boehmite (γ -AlOOH) with different morphologies have been obtained. There were two forms of boehmite observed at two different ranges of pH. The higher pH resulted in the larger crystalline size. The morphology of all obtained boehmite shows strong aggromeration. Calcination of these two different boehmite forms did not produce different γ -Al₂O₃ and its morphology remained the same as boehmite.

Background

Boehmite (γ-AlOOH) is widely used as a raw for producing γ -Al₂O₃, one technological important substances for several applications. Using γ -Al₂O₃ as a starting material in production of mechanical parts, refractors, insulator or even solid electrolyte has been known for a long time [1] and it has been known that morphology and crystalline size of the γ-Al₂O₃ are very much sensitive to characteristics of boehmite [2]. The structure of boehmite consists of Al(O,OH)₆ octahedral layers and its crystallinity is known to be related to preparation conditions [3]. Generally, boehmite of lower crystallinity is named pseudoboehmite. However, there is no significant structural difference between these two forms of boenmite [4]. Since boehmite is prepared from liquid phase by precipitation or hydrothermal method, experimental conditions such as the aluminium source, precipitant, solution pH, temperature, aging and drying conditions are thought to influence the crystalline size of the boehmite product [5].

The γ -Al₂O₃ obtained in this work is used as a raw material for producing the Na. β "-Al₂O₃ solid electrolyte which is an important material for battery technology. Since the final product of Na. β "-Al₂O₃ is also dependent on crystalline size and morphology of γ -Al₂O₃, in order to obtain desired Na. β "-Al₂O₃, selection of γ -Al₂O₃ crystalline size and morphology have to be taken into account and these are controlled by boehmite preparing conditions.

The main goal of the present paper is to investigate the effect of solution pH during precipitation to phase formation, crystalline size and morphology of boehmite. Also, the effect investigated will be extended to that of resulting calcined γ -Al₂O₃. In this study, boehtmite and γ -Al₂O₃ phase formations are determined using X-ray diffractometry (XRD) technique with Cu_{K α} radiation. Line broadening of XRD peaks is also used for crystalline size determination. Finally, the powder morphology is studied by scanning electron microscopy (SEM) Then, the effect of solution pH on characteristics of boehmite and γ -Al₂O₃ are discussed.

Materials and Methods

To synthesis boehmite, 0.5 M aqueous solutions of alumina nitrate nanohydrate (Al(NO₃)₃·9H₂O) and sodium aluminate (Na₂Al₂O₄) were utilized as starting materials. Then, these two solutions were mixed thoroughly at a ratio of 1:1. The mixed solution was heated to 60 °C and adjusted the dispersion pH between 6 to 9 with NaOH. Subsequently, the solution was held for 20 hours to complete the synthesis process while it was being stirred steadily. The solution pH was monitored before and after the synthesis. The resulted precipitates were washed with distilled water five times and followed by ethanol two times in a centrifuge. Then, they were dried at 60 °C for 24 hours. After drying, samples were calcined at 800 °C for 4 hours with heating/cooling rate of 5 °C/min. Phase development during the process was

¹Department of Physics, Faculty of Science, Ubon Rajathanee University, Thailand 34190

²National Metal and Materials Technology Center, 114 Thailand Science Park, Klong Luang, Pathumthani, Thailand 12120

³Department of Physics, Faculty of Science, Chiang Mai University, Thailand 52000

monitored by X-ray diffraction (XRD) technique which were carried out between 5° and 80° with scanning rate 0.02°/second. The XRD patterns were also used for crystalline size determination according to the Sherrer equation. Morphological properties of the prepared powders were observed by SEM.

Results and Discussion

Phase Formation and Crystalline Size of Boehmite

Precipitation from solutions of aluminum nitrate nanohydrate and sodium aluminate mixtures was observed at 60 °C due to the decomposition of NaOH. Figure 1 shows the XRD pattern of the precipitated phase after washing and drying. The linewidth of all patterns indicates precipitated powders are nano-size crystals. The main diffraction peaks can be indexed within the experimental error as boehmite γ-AlOOH (JCPDS file No. 21-1307) which has orthorhombic structure in space group Amam (63) with lattice parameters a = 3.700, b = 12.227 and c = 2.868 Å. In detailed investigation, these four different samples revealed distinctive forms, at pH 6 to 7, pseudoboehmite or gelatinous boehmite were found. While at higher pH, i. e. 8-9, the wellcrystallised boehmite was formed. To observe the difference, the crystalline size of all powders were determined via calculation by means of X-ray line broadening measurement according to the Scherrer equation:

$$D = \frac{0.9\lambda}{\beta \cos \theta}$$

where D is the mean crystalline size, λ is the wavelength (i.e. 1.5418 Å for $Cu_{k\alpha}$), β is the full width at half maximum of boemite (120). Lines instrumental broadening effects eliminated. The results of calculation using reflection from (120) plane are summarized in Table 1. According to phase formation, it can be seen that the related crystalline size of pseudobomite seems to decrease but those of normal boehtmite increases with increasing pH. Formation of these two kinds of boehmite from different pH ranges may correspond to different rate of Al-OH interaction as point out by Bokhimi et al. [6] that the smaller boehmite crystalline size corresponds to the higher Al-OH reaction. This is also consistent with the report of Okada et al [1] which suggested that, at temperature 60 °C, the boundary of gel-like state and crystalline boehmite is laid between pH 6 to 7. The same suggestion was also expressed by Panias and Krestou [7]. The gellike state is in fact characterised by a higher degree of short-range order arrangement. For the patterns of precipitates obtained from pH 6 and 7, lower relative peak intensities coupled with a broader linewidth clearly suggested the observation of such gel-like state with considerably larger proportion.

When pH exceeded 7, the precipitate went across that boudary and readily formed well-defined crystalline boehmite and their crystalline size increased with the pH value. The same observation was also reported by Okada et al [1]. This effect can be explained as an enhancement of the dissolution-reprecipation reaction by a higher pH and giving a larger crystalline size.

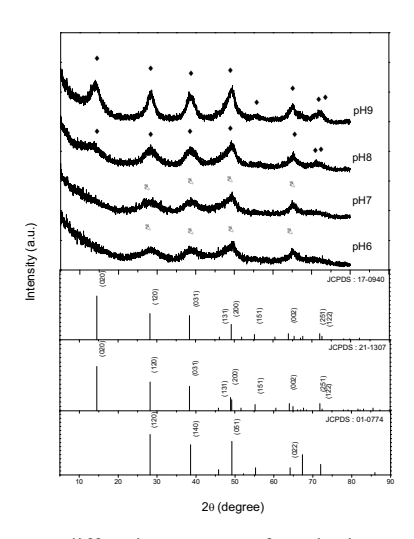


Fig.1 X-ray diffraction pattern of Boehmite precipitated from solution of different pH values at 60 °C, ♦ = Boehmite JCPDS 17-0940, 21-1307, ▼ = Boehmite JCPDS 01-0774

Table 1. Effect of pH conditions on crystalline size of

Bemite powder						
pH Crystalline size (nm)						
6 2.5						
7	1	1.9				
8	;	2.7				
9)	3.4				

Morphology of Boehmite

SEM micrographs of precipitates are shown in figure 2. It can be seen that the microstructure of sample particles precipitated from pH 6 exhibits a less well-defined shape with lower porosity and the larger aggromeration is also observed. For other three samples from higher pH, boehmite particles with lower aggromeration are clearly seen. This is because boehmite itself show a layered structure which each layer linked by H-bond. Thus aggromeration of those layers could form easily. In fact, the mechanism of crystal growth for boehmite and the effect of pH on the particle morphology are not well understood. It has been proposed that the different morphologies observed correspond to different growth mechanisms; direct crystal growth from solution producing particles with a welldefined growth morphology, while a particle coagulation mechanism producing particles of variable morphology [8, 9].

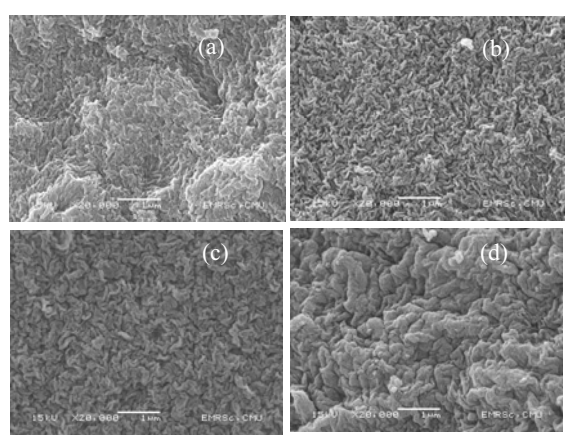


Fig.2 SEM micrographs of sample precipitated at (a) pH 6, (b) pH 7, (c) pH 8 and (d) pH 9.

Calcination of Boehmite

After calcination of boehmite at 800 °C for 4 hr. with heating rate of 5 °C/min, the calcined powders were investigated in both phase formation and morphology. Figure 3 shows XRD patterns of calcined transition alumina produced from four boehmites obtained from four diffrerent pH conditions. All patterns can be identified as γ-Al₂O₃ phase with strongest reflection at $2\theta = 68^{\circ}$, (100). Although, they were produced from different boehmite morphologies and crystalline sizes, but there is no significant distinctive. However, with closer details of the observation, it is suggested that at the same heating temperature, boehmite of larger crystalline size provided sharper and more intense γ-Al₂O₃ XRD peaks. The present study is consistent with that reported by Okada et al. [10]. The morphology of γ-Al₂O₃ is still very much like that of boehmite in which strong aggromeration is also found and this is also seen in the line shape of the XRD peaks.

Conclusion

Crystalline size and morphology of boehmite are sensitive to precipitation conditions, especially pH of the starting solution. The higher pH value gives a larger crystalline size with stronger aggromeration. Two forms of boehmite, pseudobomite and crystalline boehmite, were found to form after completed precipitation. After calcination of boehmite to produce $\gamma\text{-}Al_2O_3$ at 800 $^{\circ}\text{C}$ for a constant time of 4 hr, the aggromeration was found and the morphology was very much the same as that of boehmite precipitated from pH 7.

Acknowledgment

This work was supported by The Thailand Research Fund and National Research Council of Thailand.

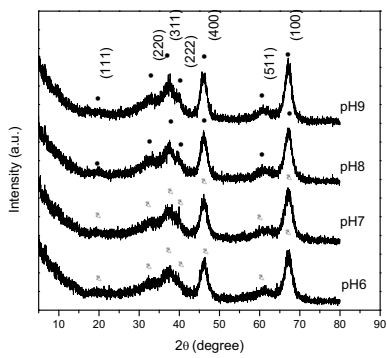


Fig.3 the XRD pattern of powders calcined at 800 °C, \bullet = γ -Al₂O₃ from crystalline boehmite, ∇ = γ -Al₂O₃ from pseudoboehmite.

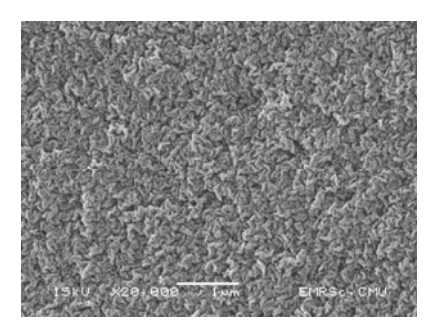


Fig.4 SEM micrograph of sample after calcination at 800°C for 4 h and heating/cooling rate of 5 °C/min.

- Okada, K. Nagashima, T., Kamishima, Y., Yasumori, A. and Tsukada, T. Relationship between formation Conditions, Properties, and Crystalline size of Boehmite. *Journal of Colloid and Interface Science* 2002, 253: 308-314.
- POTDAR, H.S., Jun, K-W., Bae, J. W., Kim, S-M. and Lee, Y-J. Synthesis of nano -sized porous g-alumina powder via a precipitation/digestion route. *Applied Catalysis A: General* 2007, 321: 109-116.
- 3. Machida, M., Takenami, M., and Hamada, H. Intercalation of pseudo-boehmite: a novel preparation route to microporous Al-ti oxide. *Solid State Ionics* 2004, **172**: 125-128.
- 4. Alphonse, P. and Courty, M. Structure and thermal behaviour of nanocrystalline boehmite. *Thermochimica Acta* 2005, **425**: 75-89.
- Petrovic, R., Milonjic, S., Jokanovic, V., Kostic-Gvozdenovic, Lj., Petrovic-Prelevic, I., and Janackovic, Dj. Influence of synthesis parameters on the structure of boehmite sol particles. *Powder Technology* 2003, 133: 185-189
- Bokhimi, X., Toledo-Antonio, J. A., Guzman-Castillo, M. L. and Hernandez-Beltran, F. Relationship between crystalline size and bond lengths in boehmite. *Journal of Solid State Chemistry* 2001, 159: 32-40.
- 7. Panias, D. and Krestou, A. Effect of synthesis parameters on precipitation of nanocrystalline boehmite from aluminate solutions. *Powder Technology* 2007, **175**: 163-173.
- 8. Hulling, J.C. and Messing, G.L. Chemistry-crystallization relations in molecular mullite gels. *Journal of Non-Crystalline Solid* 1992, **147**: 213-221.
- Kaya, C., He, J. Y., Gu, X. and Butler, E. G. Nanostructured ceramic powders by hydrothermal synthesis and their applications. *Microporous and Mesoporous Materials* 2002, 54: 37-49.
- 10.Okada, K., Nagashima, T., Kameshima, Y. and Yasumori, A. Effect of crystalline size on the thermal phase change and porous properties of boehmite. *Journal of Colloid and Interface Science* 2002, **248**: 111-115.

Electron Microscopy and Optical Spectroscopy Analyses of Carbon Nanotube Composite Electrodes for Dye-Sentisized Solar Cells

A. Chindaduang¹, T. Sawatsuk¹, W. Wongsukkab¹, C. Sae-kung² G. Tumcharern¹ and S. Pratonetep^{1*}

National Nanotechnology Center (NANOTEC), NSTDA, 111 Thailand Science Park,
Phathumthani Rd, Klong 1, Klong Luang, Pathumthani 12120, Thailand

Institute of Solar Energy Technology Development (ISET), 111 Thailand Science Park,
Paholyothin Rd, Klong 1, Klong Luang, Pathumthani 12120, Thailand
e-mail: sirapat@nanotec.or.the-mail: sirapat@nanotec.or.th

Abstract

Photovoltaic devices based on dye-sensitized solar cells (DSSCs) have attracted great attention owing to their prospect of high energy conversion efficiency and low production cost. The power conversion efficiency and the long term stability have been reported to be improved by incorporating carbon nanotubes (CNTs) into the front electrode. However, methods to fabricate electrodes made of carbon nanotube composites are often high in cost, e.g. chemical vapour deposition (CVD), or involve some complicated procedures, e.g. functionalization of CNTs with titanium dioxide (TiO₂). Here we report morphological and optical characterizations of DSSC composite electrodes composed of multi-walled carbon nanotubes (MWCNTs) and TiO₂. The composite electrodes were fabricated by a direct mixing method with aid of organic surfactants. The electrodes containing MWCNTs of 0.025% by weight enhanced the power conversion efficiency by a factor of 1.42, under the Air Mass 1.5 illumination standard for an active area of 0.36 cm². The morphology and the composition of the films were characterized by the Field-Emission Scanning Electron Microscope (FE-SEM) as well as the Raman Spectroscopy and Microscopy. The optical transparency of the composite films was revealed by the optical absorption spectroscopy. The SEM results indicate that the increase in the electrode active surface area induced by the MWCNTs is not sufficient to account for the DSSC efficiency improvement, of which the mechanism should be best explained by the improved conductivity of the films from the MWCNTs additives. On the contrary, with MWCNTs additives of over 1%, the conversion efficiency decreases gradually, which seems to result from a poor optical transparency of the composite films.

Background

Carbon nanotubes (CNTs) have been attracting considerable attention due to their unique properties, such as good electrochemical stability, low resistivity and high surface area [1-4]. CNTs play a crucial role in varieties of applications, for example, in field emission displays [5], energy storage devices [6], electrochemical capacitors [7] as well as energy conversion devices such as dyesensitized solar cells (DSSCs) [8].

There has been some interest in the incorporation of CNTs in each component of DSSCs to improve the performance, however, with limited success. The presence of CNTs in TiO_2 matrix [9] or ionic liquid electrolyte [10] shows some improvement in the power conversion efficiency. Most reports in the literature required the well-align carbon nanotubes fabricated by a high cost vacuum-based technique such as reactive sputtering or Chemical Vapour Deposition (CVD) [11].

Here we report a simple method to improve the DSSCs performance by the incorporation of multi-walled carbon nanotubes (MWCNTs) into the front electrode using a direct mixing method. The

morphology of TiO₂-MWCNTs film was observed by Field Emission Scanning Electron Microscope (FE-SEM). The presence of MWCNTs into the film was confirmed by the Raman Spectroscopy and Microscopy. The optical transparency of the composite films was characterized by the optical absorption spectroscopy.

Materials and Methods

All chemicals are commercially available and were used without further purification unless otherwise stated. MWCNTs were kindly provided by Bayers Materials. Indium-doped tin oxide (ITO) conductive glasses were purchased from Bangkok Solar Cell Ltd (sheet resistance: 10 Ω /square). The power conversion efficiency of DSSCs was measured from photocurrent-voltage characteristics with a transient photocurrent under the AM 1.5 irradiation (100 mW cm⁻²). Optical absorption spectra were obtained by the Perkin Elmer Lambda 650. Raman spectra and Raman images were recorded in the direct reflection mode from the sample surface using by the NTMDT Ntegra spectra system with a 632.8 nm excitation.

The images were recorded using a 60X objective. FE-SEM images were taken by the Hitachi S-4700 SEM.

Preparation of TiO₂-MWCNT Electrodes

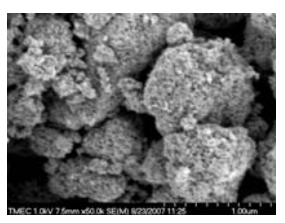
Mixtures of 0-10 wt.% MWCNTs and TiO₂ were dispersed in terpineol by ultrasonication. DSSCs front electrodes were prepared by printscreening the mixtures on ITO glass substrates with an active area 0.36 cm². The TiO₂-MWCNTs composite films were obtained after annealed at 500 °C for 2 hours.

Fabrication of DSSCs using TiO₂-MWCNTs as the Front Electrode

The TiO_2 -MWCNTs films were soaked in an ethanol solution of $Ru(II)L_2(NCS)_2$:2TBA (L = 2,2'-bipyridyl-4,4'-dicarboxylate, TBA = tetrabutylammonium). Pt-coated ITO glass substrates were used as the counter electrode. The acetonitrile solution of LiI, I_2 , 1-methyl-3-propylimidazolium iodide, and 4-*tert*-butylpyridine was used as an electrolyte.

Results and Discussion

Figure 1 displays the FE-SEM images of the annealed TiO2 films with no MWCNT and those with 10 wt.% of MWCNTs. Except for the observation of sparely segregated tubular structures in figure 1 (b), both FE-SEM images display similar porous materials of TiO₂. This implies that the incorporation of MWCNTs does not strongly affect on the surface area of the electrodes. Raman spectra confirm the presence of TiO2 and CNTs in the prepared front electrodes. Three Raman peaks at approximately 395, 518, and 642 cm⁻¹ indicate the anatase form of TiO2, while the other three peaks at approximately 1348 and 1624 cm⁻¹ represent the D and G lines of MWCNTs, respectively (figure 2). Raman images (10 x 10 μm²) of the MWCNTs-TiO₂ composite films were displayed in figure 3.



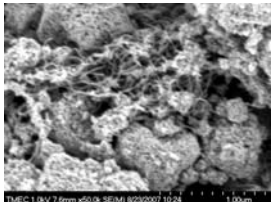


Fig. 1 FE-SEM images of (a) conventional TiO_2 and (b) TiO_2 -MWCNTs (at 10%wt concentration) front electrodes.

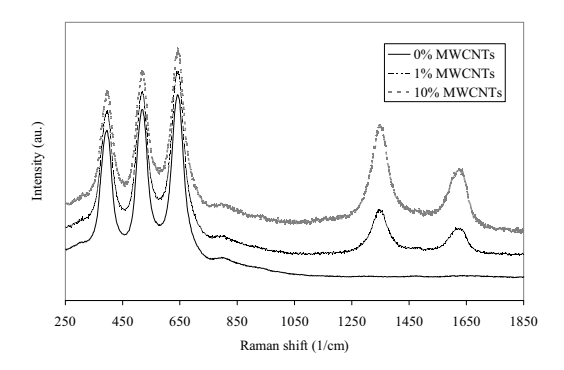


Fig. 2 Raman spectra of conventional ${\rm TiO_2}$ and ${\rm TiO_2}$ -MWCNTs front electrodes.

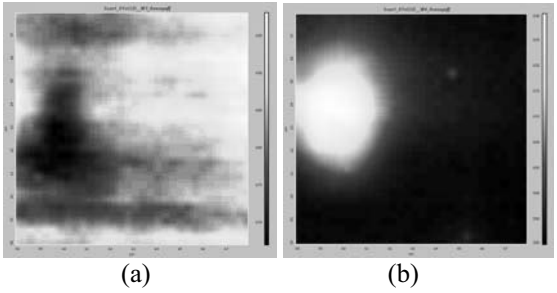


Fig. 3 Raman images of (a) conventional TiO₂ and (b) TiO₂-MWCNTs front electrodes.

The *J-V* characteristics of the DSSCs under the AM 1.5 illumination standard with an active area of 0.36 cm² are reported in Table 1. In the best conditions, the incorporation of MWCNTs at 0.025 wt%) in TiO₂ film increases the conversion efficiency by approximately 50 %, compared to the conventional DSSCs,. Further increase in the amount of MWCNTs resulted in a gradual decrease in the power conversion efficiency, owing to losses in optical transparency of the electrodes as shown by the optical absorption spectra (figure 3).

Table 1. *J-V* characteristics of TiO₂-MWCNTs front electrode of the DSSCs. Voc, Jsc and FF are the open-circuit voltage, the short-circuit current and the filling factor of the DSSCs, respectively.

MWCNTs (Wt.%)	Voc (V)	Jsc (mA/cm ²)	FF	Efficiency (η)
0.000	0.77	5.95	0.73	3.33
0.025	0.80	8.45	0.84	5.67
0.050	0.79	6.40	0.74	3.73
0.075	0.77	6.69	0.67	3.43
0.100	0.76	6.04	0.61	2.79
0.200	0.72	5.01	0.67	2.41
0.300	0.69	6.46	0.53	2.35
0.500	0.68	5.53	0.60	2.26
1.000	0.58	6.14	0.46	1.63
10.000	0.36	2.50	0.39	0.35

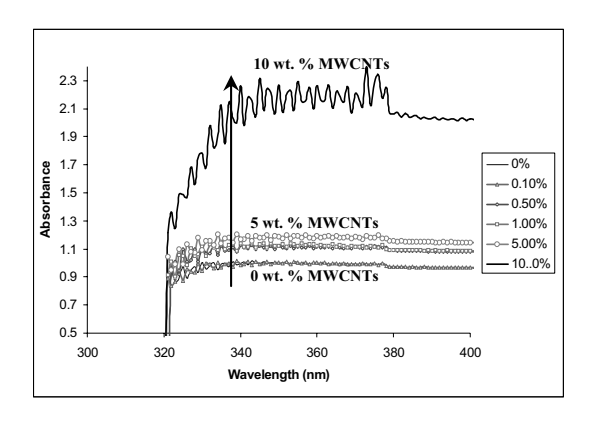


Fig. 3 Optical absorption spectra of TiO_2 films containing 0-10 wt.% of MWCNTs.

Conclusion

We have demonstrated the improvement of the power conversion efficiency of DSSCs by the incorporation of MWCNTs in the TiO_2 front electrode using a direct mixing method. At the best conditions, the TiO2-MWCNTs DSSCs attained in the short-circuit current density of 8.45 mA/cm², leading to the overall power conversion efficiency of 5.67% under the AM 1.5 illumination standard with an active area of 0.36 cm². FE-SEM, Raman spectroscopy as well as Raman microscopy confirmed the presence of MWCNTs in the TiO₂ active layer. The optical absorption measurements of the films suggest that an excess amount of MWCNTs in the electrode lead to degradation of the DSSC performance due to optical transparency losses. Future work should focus on further optimization of the MWCNT DSSC fabrication processes and detailed studies of the mechanisms for the power conversion efficiency enhancement.

Acknowledgment

The authors are grateful for the research funding from the Institute of Solar Energy Development (National Science and Technology Development Agency, Thailand) and also would like to thank Mr. Matthias Hanusch for the supplied of synthezed imidazole.

- 1. Ijima, S. Helical microtubules of graphitic carbon. *Nature* 1991, 354: 56-58.
- 2. Wang, J. Carbon-nanotube based electrochemical biosensors: A review. *Electroanalysis* 2005, 17: 7-14.
- 3. Kay, A. and Grätzel. M. Low cost photovoltaic modules based on dye sensitized nanocrystalline titanium dioxide and carbon powder. *Solar Energy Materials and Solar Cells* 1996, 44: 99-117.
- 4. Kim, H. J., Lee, D. Y. Koo, B. K. Lee, W. J. and Song. J. S. Preparation of CNT electrodes for enhanced electrochemical properties. *Proceedings of the KIEEME Annual Conference* 2004, 17: 1090.
- 5. De Heer, W. A., Châtelain, A. and Ugarte, D. A carbon nanotube field-emission electron source. *Science* 1995, 270: 1179-1180.
- 6. Che, G., Lakshmi, B. B., Fisher, E. R. and Martin, C. R. Carbon nanotube membranes for electrochemical energy storage and production. *Nature* 1998, 393: 346-349.
- Niu, C., Sichel, E. K., Hoch, R., Moy, D., and Tennent, H. High power electrochemical capacitors based on carbon nanotube electrodes. *Applied Physics Letters* 1997, 70: 1480-1482.
- O' Regan, B. and Grätzel. M. A low cost, highefficiency solar cell based on dye sensitized colloidal TiO₂ films. *Nature* 1991, 353: 737-740.
- 9. Vincent, P., Brioude, A., Journet, C., Rabaste, S., Purcell, S. T., Le Brusq, J. and Plenet, J. C. Inclusion of carbon nanotubes in a TiO sol-gel matrix. *Journal of Non-Crystalline Solids* 2002, 311: 130-137.
- 10. Park, N. -G., Van De Lagemaat, J. and Frank, A. J. Comparison of dye-sensitized rutile- and anatase-based TiO solar cells. *Journal of Physical Chemistry B* 2000, 104: 8989-8994.
- 11. Park, Y -J.; Park, S -C.; Jung, W -C.; Nam, J -G.; Kim, H –J. *US patent (Patent application)*, US2006/0137741 A1.

A Microstructural Investigation of Al-doped ZnO Films Prepared by Spray Pyrolysis

Chanipat Euvananont ¹, Supattra Pakdeesathaporn², Pawilas Pratoomwan², Visittapong Yodsri¹,

Yot Boontongkong¹, Chanchana Thanachayanont^{1*}, and Chris Boothroyd³

Abstract

Aluminum-doped ZnO (ZnO:Al) films have been prepared by spray pyrolysis using zinc acetate in methanol as a precursor solution and AlCl₃ as a dopant. It was found that all films exhibited a preferred crystallographic orientation. The average crystallite sizes calculated from X-ray diffraction data ranged from 19 to 22 nm, while dark-field TEM images exhibited individual crystallites ranging from approximately 10 to 100 nm in size. Scanning electron micrographs revealed porous film structures comprising petal-shaped grains, most of which were significantly larger than the calculated crystallite sizes, indicating that such grains comprise multiple crystallites. Any effects of the Al doping concentration on the crystal structure or the microstructure of the ZnO films were not apparent from our current results, however.

Background

During the past few decades, there has been a great demand for transparent conducting oxide (TCO) films, especially from the electronic industry. The TCO films have been used in various applications, e.g. solid state gas sensors, transparent electrodes for displays, heat mirrors, and window layers in heterojunction solar cells [1-4]. Compared with tin oxide (SnO₂) used in dyesensitized solar cells and indium tin oxide (ITO) used in polymer solar cells, zinc oxide (ZnO) is used in amorphous and microcrystalline silicon solar cells due to its stability in hydrogen plasma which is the process environment used for this application [5]. ZnO is an n-type semiconducting oxide of the group II metal zinc, and belongs to the P6₃mc space group [6]. The undoped ZnO has high n-type conductivity due to defects such as oxygen vacancies and Zn interstitials, which form donor levels [7]. Group IIIa elements (Al, Ga, In) have been used to improve the electrical conductivity and thermal stability of ZnO films. For this work, Al3+ substitution on Zn2+ was chosen due to the small ion size of Al^{3+} compared to that of Zn^{2+} ($r_{Al}^{3+}=0.054$ nm and $r_{Zn}^{2+}=0.074$ nm).

Various deposition techniques have been used to grow ZnO thin films, such as sputtering [8], pulsed laser deposition [9], and spray pyrolysis [10]. Among several techniques used to obtain high-quality undoped and doped ZnO thin films, the spray pyrolysis method has the advantages of low cost, ease of operation, and the possibility to coat large surfaces in mass production. The influence of experimental parameters such as precursor concentration, deposition temperature,

deposition time, doping concentration, and growth rate on the morphology, conductivity, and optical transmittance of ZnO films have been investigated in order to obtain thin uniform films of the necessary quality for optoelectronic devices [11,12]. In the present study, the Al doping concentration was varied from 0 to 1.0% in order to investigate the potential effect of the Al content on the microstructure of the ZnO films.

Materials and Methods

ZnO films were prepared by the spray pyrolysis method, using a 0.05M solution of zinc acetate dihydrate (Aldrich, cat. No. 22,335-2) in methanol (MERCK, AR grade) as the precursor [13]. Aluminum-doped series were produced by adding AlCl₃ at concentrations of 0.1, 0.3, 0.5, 0.7 and 1.0 % (atomic) to the precursor solution. Compressed air was used as the carrier gas at a flow rate of 1 liter/min. Prior to deposition, the hot plate-backed substrate was heated to 430°C. The precursor solution was atomized into fine droplets and carried upwards to a heated substrate, which was either glass or a Si wafer (with a native oxide layer as the immediate surface). Spray pyrolysis was then carried out for 1 hour to obtain each film, after which the substrate was allowed to cool to room temperature before further analysis. The crystal structures of the ZnO films were studied with Xray diffraction (Rigaku TTRAX III x-ray diffractometer), employing $CuK_{\alpha 1}$ operating at 50 kV & 300 mA, with a scanning speed of 2°/min at a 2θ step of 0.02°. The microstructures were examined using FE-SEM

¹ National Metal and Materials Technology Center, 114 Thailand Science Park Paholyothin Rd., Klong 1, Klong Luang, Pathumthani 12120, Thailand

² Department of Materials Engineering, Kasertsart University, Bangkok 10900, Thailand

³ Institute of Materials Research and Engineering, 3 Research Link, 117602 Singapore e-mail: chanchm@mtec.or.th

(JEOL-JSM 6301F, 20 keV), TEM (JEOL 2010, 200 keV), and high-resolution TEM (Philips CM300 FEG, 300 keV).

Results and Discussion

The spray pyrolysis process (pyrolytic decomposition of atomized droplets of the precursor solution on a heated substrate) results in the deposition of mostly transparent ZnO films. Figure 1 shows a representative example of the optical transmittance spectra obtained from our ZnO films deposited onto glass substrates.

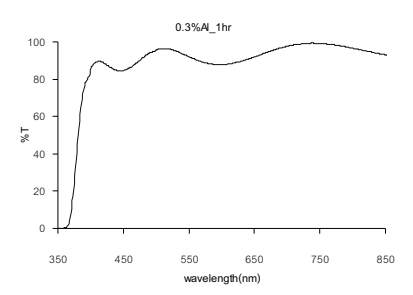


Fig. 1 Optical transmittance of a ZnO film with 0.3% Al doping concentration.

The X-ray diffraction patterns in figure 2 indicate a polycrystalline hexagonal (wurtzite) structure for the deposited films which matches the standard ZnO diffraction pattern [14]. Previous studies have reported the prevalence of the (002) planes observed for undoped and Al-doped ZnO films deposited on glass substrate by spray pyrolysis [15, 16]. Consistently, a preferred orientation of the (002) planes parallel to the substrate was also observed in our ZnO films grown on native oxide-coated Si wafer.

Figure 3 shows the average crystallite sizes of the sample series calculated based on the X-ray diffraction data and calculated using the Scherrer formula:

$$I = \frac{0.9\lambda}{\beta \cos \theta}$$

where β is the observed angular width at half maximum intensity (FWHM) of each diffraction peak located at a peak position 2θ , and λ is the X-ray wavelength. The average crystallite sizes range from 19 nm to 22 nm. However, figure 3 shows no particular trend in crystallite size variation with increasing aluminum doping concentration. This is in contrary to previous reports by Hichou et al. [15] and Allah et al. [17], which showed that a higher doping concentration of Al doping (2-4%) led to decreasing crystallite sizes.

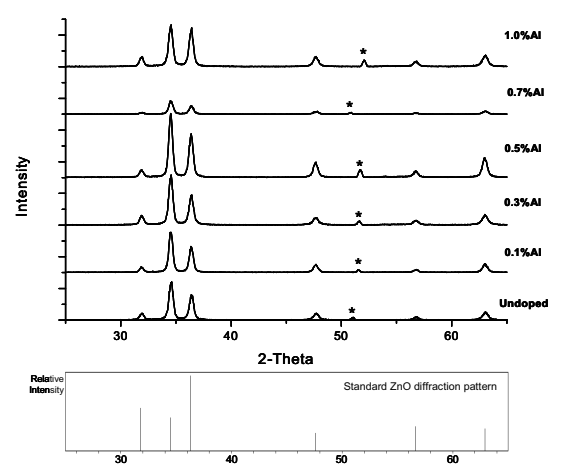


Fig. 2 X-ray diffraction patterns from pure and Al-doped ZnO films (top) and the standard ZnO diffraction pattern (bottom). (* Designates peaks from the silicon substrate.)

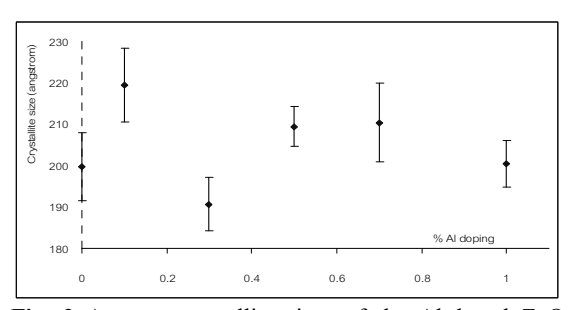


Fig. 3 Average crystallite sizes of the Al-doped ZnO films series calculated from the respective X-ray diffraction patterns.

Plan-view SEM investigation (figure 4) reveals a porous structure of the ZnO films with Al doping concentrations of 0, 0.1, 0.3, 0.5, 0.7, and 1.0at%, respectively. Petal-shaped grains of various sizes were observed all samples. The majority of these grains appear several times larger than the average crystallite sizes calculated from X-ray diffraction data (19-22 nm); thus, indicating that most of the grains comprise multiple crystallites. No systematic variation in the microstructure of the ZnO films as a function of the doping concentration was detected.

Figure 5 shows bright-field and dark-field TEM images taken from an undoped ZnO film. The crystallites within the undoped ZnO film are not uniform, with sizes varying from around 10 to 100 nm, whereas the average crystallite size obtained from XRD result is 20 nm. Similarly non-uniform crystallite sizes were observed for all other doped samples in the series, see figure 6 for example. Figure 7 shows a high-resolution transmission electron micrograph of the 1% Al-doped ZnO sample, wherein overlapping crystallites of various sizes are present.

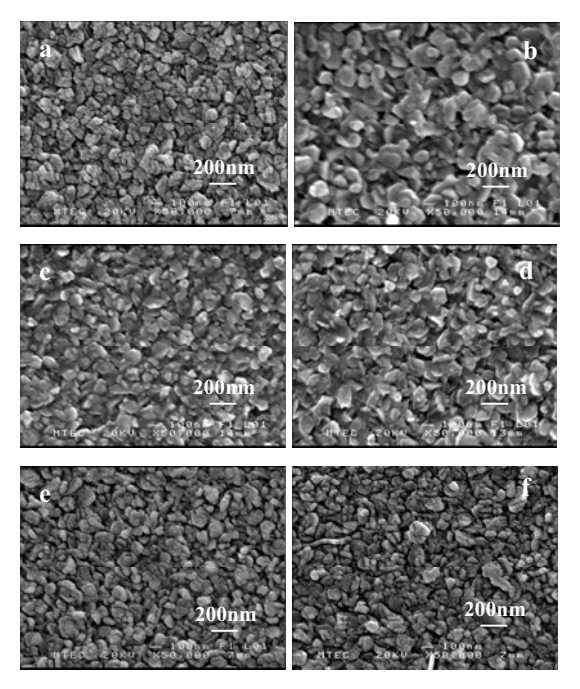


Fig.4 Plan-view scanning electron micrographs of ZnO films containing (a) 0%, (b) 0.1%,(c) 0.3%, (d) 0.5%, (e) 0.7%, and (f) 1.0% Al.

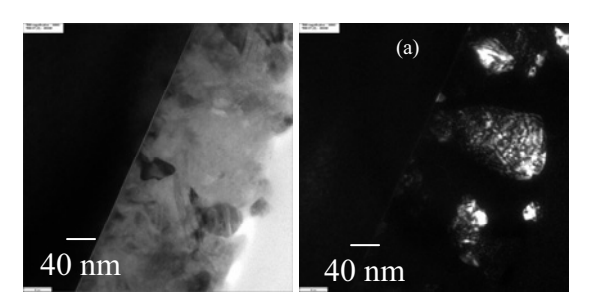


Fig. 5 (a) bright-field and (b) dark-field TEM micrographs from the undoped ZnO film.

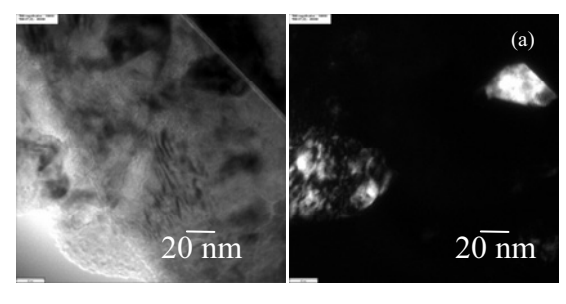


Fig. 6 (a) bright-field and (b) dark-field TEM micrographs from the 0.5% Al-doped ZnO film.

Conclusion

Aluminum-doped ZnO films with Al concentrations up to 1.0% have been prepared by spray pyrolysis from zinc acetate solutions in methanol, using AlCl₃ as the dopant. X-ray diffraction indicates a preferred c-axis orientation perpendicular to the substrate in all samples of the series, while the calculated average crystallite sizes range from 19 to 22 nm. SEM micrographs reveal porous film structures comprising petal-shaped

grains that are significantly larger than the calculated crystallite sizes. However, no apparent effects of the Al doping concentration on the crystal structure or the microstructure of the ZnO films were found. Further work is underway to investigate the reproducibility of our current results, as well as to characterize the electrical properties of these Al-doped ZnO films.

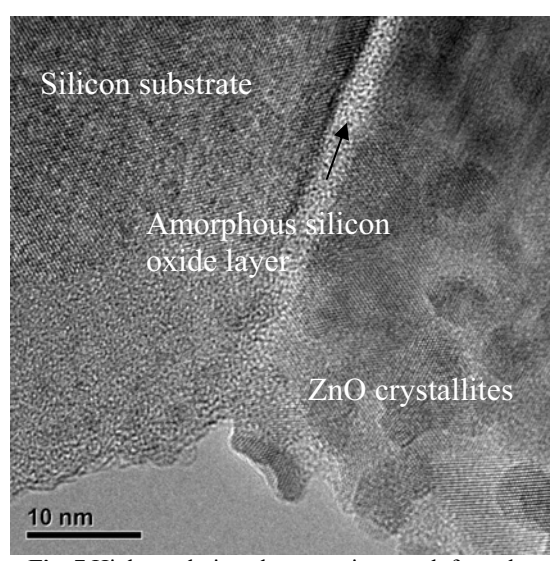


Fig. 7 High-resolution electron micrograph from the 1.0% Al-doped ZnO film.

Acknowledgment

The authors would like to thank the National Metal and Materials Technology Center for financial support (MTEC Grant No. MT-B-48-CER-07-187-I) and Miss Onuma Santawitee for her help with SEM imaging.

- 1. Stambolova I, Konstantinov K, Vassilev S, Peshev P, Tsacheva T S. High transmittance and low resistive AZO films for thin film solar cells. *Mater. Chem. Phys.* 2000, 63: 104-108.
- 2. Chen M, Pei Z L, Sun C, Gong J, Huang R F, Wen L S. ZnO: an attractive potential substitute of ITO in flat display panels. *Mater. Sci. Eng. B* 2001, 85: 212-217.
- 3. Chopra K L, Major S, Pandya D K. Properties of InGaN deposited on Glass at Low Temperature. *Thin Solid Films* 1983, 102: 1-46.
- 4. Jin Z-C, Hamberg I, Gradqvist C G, Sernelius B E, Berggren K-F. Reactively sputtered AZO films for energy-efficient windows. *Thin Solid Films* 1988, 164: 381-386.
- 5. Major S, Kumar S, Bhatnagar M and Chopra K L. Effect of hydrogen plasma treatment on transparent conducting oxides. *Appl. Phys. Lett.* 1986, 49: 394-396.
- 6. Steiner, T. Semiconductor Nanostructures for Optoelectronic Applications, *Artech House, Inc.*, 2004.

- 7. Look D C, Hemsky J W, Sizelove J R. Residual Native Shallow Donor in ZnO. *Phys. Rev. Lett.* 1999, 82: 2552-2555.
- 8. Tominaga K, Umezu N, Mori I, Ushiro T, Moriga T, Nakabayashi I. Transparent conductive ZnO film preparation by alternating sputtering of AZO and Zn or Al targets. *Thin Solid Films* 1998, 334: 35-39.
- 9. Khandelwal R, Singh A P, Kapoor A, Grigorescu S, Miglietta P, Evgenieva N S, Perrone A. Effects of deposition temperature on the structural and morphological properties of thin ZnO films fabricated by pulsed laser deposition. *Optics & Laser Technology* 2008, 40: 247–251.
- 10. Ootsuka T, Liu Z, Osamura M, Fukuzawa Y, Kuroda R, Suzuki Y, Otogawa N, Mise T, Shinan W, Hoshino Y, Nakayama Y, Tanoue H, Makita Y. Studies on aluminum-doped ZnO films for transparent electrode and antireflection coating of h-FeSi2 optoelectronic devices. *Thin Solid Films* 2005, 476: 30–34.
- 11. Choi B G, Kim I H., Kim D H, Lee K S, Lee T S, Cheong B, Baik Y-J., Kim W M. Electrical, optical and structural properties of transparent and conducting ZnO thin films doped with Al and F by rf magnetron sputter. *Journal of the European Ceramic Society* 2005, 25: 2161–2165.
- 12. Joseph B, Manoj P K, Vaidyan V K. Studies on the structural, electrical and optical properties of Al-doped ZnO thin films prepared by chemical spray deposition. *Ceramics International* 2006, 32: 487–493.

- 13. Lokhande B J, Patil P S, Uplane M D. Studies on structural, optical and electrical properties of boron doped zinc oxide films prepared by spray pyrolysis technique. *Physica B* 2001, 302-303: 59-63
- 14. Powder Diffraction File, Data Card 5-644, 3c PDS International Center for diffraction Data, Swartmore, PA. +6.
- 15. Hichou A El, Addou M, Bougrine A, Dounia R, Ebothe J, Troyon M and Amrani M. Cathodoluminescence properties of undoped and Al-doped ZnO films deposited on glass substrate by spray pyrolysis. *Mat. Chem. Phys.* 2004, 83: 43-47.
- 16. Romero R, Leinen D, Dalchiele E A, Ramos-Varrado J R and Martin F. The effects of zinc acetate and zinc chloride precursors on the preferred crystalline orientation of ZnO and Aldoped ZnO thin films obtained by spray pyrolysis. *Thin Solid Films* 2006, 515: 1942-1949.
- 17. Allah F K, Abe S. Y, Nunes C M, Khelil A, Cattin L, Morsli M, Bernede J C, Bougrine A, del Valle M A and Diaz F R. Characterisation of porous doped ZnO thin films deposited by spray pyrolysis technique. *Applied Surface Science* 2007, 253: 9241-9247.
- Rozati S M and Asesteh S M. Characterization of ZnO:Al thin films obtained by spray pyrolysis technique. *Materials Characterization* 2007, 58: 319-322.

Phase Formation and Microstructure of Ba(Zr_{0.20}Ti_{0.80})O₃ Ceramics Prepared via Solid State Reaction Method

T. Bongkarn^{1*}, N. Phungjitt¹, N. Vittayakorn²

¹ Department of Physics, Faculty of Science, Naresuan University, Phitsanulok, Thailand

² Department of Chemistry, Faculty of Science, King Mongkut's Institute of Technology Ladkrabang, Bangkok, Thailand

e-mail: researchcmu@yahoo.com

Abstract

In this work, effects of calcination and sintering temperatures on phase formation and the microstructure of $Ba(Ti_{0.80}Zr_{0.20})O_3$ (BZT) ceramics were investigated. The BZT powders were prepared via a solid state reaction method under various calcination and sintering temperatures. X-ray diffraction (XRD) was used to evaluate the optimum condition for calcinations. Microstructure was studied by using scanning electron microscopy (SEM). It was found that the pure perovskite phase of BZT powder was obtained at a calcination condition of 1250 °C for 4 h. Sintered pellets showed a pure peroverskite cubic phase in all samples. Lattices parameter (a) tended to increase with increasing calcination temperatures. Microstructures of the powders exhibited an almost-spherical morphology and had a porous agglomerated form. Average particle sizes and average grain sizes increased from 0.27 to 1.48 μ m and 15.06 to 60.30 μ m when increasing calcination and sintering temperatures from 800 to 1350 °C and from 1400 to 1600 °C, respectively. Dielectric constant was relative with the density of the sintered ceramic.

Background

Barium titanate (BaTiO₃, BT) is well known as a fundamental ferroelectric perovskite oxide [1] and is often used in multilayer ceramic capacitors (MLCs) due to its high dielectric constant [2]. The BaTiO₃ displays dielectric anomalies at 130, 0, and -90 °C with respective transformations in symmetry from cubic to tetragonal, from tetragonal to orthorhombic orthorhombic, and from rhombohedral, respectively. Those anomalies are accompanied by a high dielectric constant near the phase transition [3]. Nature and phase transition temperature of BT can be modified via partial substitution of either Ba ions (A-site doping) or Ti ions (B-site doping). A-site doping with cations of the same valence as Ba causes the Curie temperature (T_c) (~ 130 °C) to either decrease (Sr substitution) or increase (Pb substitution) without any significant broadening of the transition [4]. With B-site doping, ferroelectric domains, which are associated with a cooperative off-center displacement of Ti⁴⁺ ions in their TiO₆ octahedra, are disrupted, which often lead to a broadening of the transition at T_c. Partial replacement of titanium by tin or hafnium generally leads to a reduction in T_c and an increase in the permittivity maximum with dopant content [5].

Barium zirconate titanate ($Ba(Zr_xTi_{1-x})O_3$, BZT) is obtained by substituting ions at the B site of $BaTiO_3$ with Zr ions. This substitution results in a

decrease in the temperature and a broadening of the permittivity maximum [6]. Brajer and Kulscar showed that, as the zirconium content increases, the orthorhombic-tetragonal phase transition temperature increases and the tetragonal-cubic phase transition temperature decreases [7,8]. At a Zr/Ti ratio greater than 0.10, the three dielectric constant peaks coalesce into a single broad maximum [9]. Moreover, the transition temperature of the BZT shifts to a lower temperature region with the increase of the Zr contents. The dielectric study of the Ba(Zr_xTi_{1-x})O₃ ceramics with x=0.20 and 0.25 showed a normal ferroelectric with weak diffuse phase transition behaviors [10]. Diffuse phase transition and a relaxor-like behavior were found at higher Zr contents (x=0.30 and 0.35). High tunability and dielectric loss of the $Ba(Zr_xTi_{1-x})O_3$ with x=0.20 ceramic, measured at room temperature under the biasing field 20 kV/cm, are 82% and 0.0034, respectively [11]. This makes the Ba(Zr_{0.20}Ti_{0.80})O₃ ceramics a promising material for ceramic capacitors. However, to the author's best knowledge, no phase formation and microstructure of BZT ceramics prepared by the solid state reaction method have been reported yet. Therefore, in the present work, the phase formation and the microstructure of the Ba(Zr_{0.20}Ti_{0.80})O₃ ceramics prepared via solid state reaction method was studied.

Materials and Methods

Starting materials were commercially available barium carbonate, BaCO₃ (99%) titanium (IV) oxide, TiO₂ (99%) and zirconium (IV) oxide, ZrO₂ Barium (99%). zirconate titanate (Ba(Zr_{0.20}Ti_{0.80})O₃, BZT) powder was synthesized solid state reaction of thoroughly ground mixtures of BaCO₃, TiO₂ and ZrO₂ powders by a ball milling procedure (zirconia milling media under ethanol for 24 h). Drying was carried out at 120 °C for 4 h. After sieving, various calcination temperatures, ranging from 800 to 1350 °C, with a dwell time of 4 h. and heating/cooling rate of 5 °C/min, were performed. The calcined powders were then pressed into disks with a diameter of 15 mm at a pressure of 40 MPa. The pellets were sintered from 1400 to 1600 °C for 2 h and cooled in a furnace. For electrical measurements, silver paste was fired on both sides of the polished samples at 500 °C for 30 min and used as electrodes.

X-ray diffractometer (XRD; Philip PW3040/60 X' Pert Pro) were employed to identify the phase formed and optimum temperature of the BZT powders and ceramics. Morphologies of the calcined powders and sintered ceramics were imaged using scanning electron microscope (SEM; LEO 1455 VP). Densities of the sintered ceramics were measured by the Archimedes method and average grain size was determined by using a mean linear intercept method. Capacitance was measured with a LCR meter (Agilent 4263B) at room temperature. Dielectric constant (\mathcal{E}_r) calculated using the geometric area and thickness of the discs.

Results and Discussion

The XRD patterns of the BZT powders formed with different calcination temperatures are given in figure 1. After calcination at 800 °C, the crystalline phase of BZT was accompanied with BaCO3 and ZrO₂ as separate phases, whose X-ray peaks matche the JCPDS file number 41-0373 [12] and 24-1165 [13]. As the temperature increased to 1000 °C, the peaks corresponding to the raw materials disappeared, while the intensity of the BaTiO₃, BaZrO₃ and Ba₂ZrO₄ peaks became minor phases, which can correlate with JCPDS file number 03-0726 [14], 06-0399 [15] and 24-0130 [16] respectively. After calcination at 1200 °C, the peaks corresponding to BaTiO3, BaZrO3 and Ba₂ZrO₄ were not detectable. Evidently, a single phase of BZT is formed by calcination at 1250 °C.

The strongest reflections in the majority of the XRD patterns indicate the formation of the perovskite phase of BZT, which can be matched with the JCPDS file number 36-0019 [17]. To a first approximation, this phase is a cubic perovskite type structure.

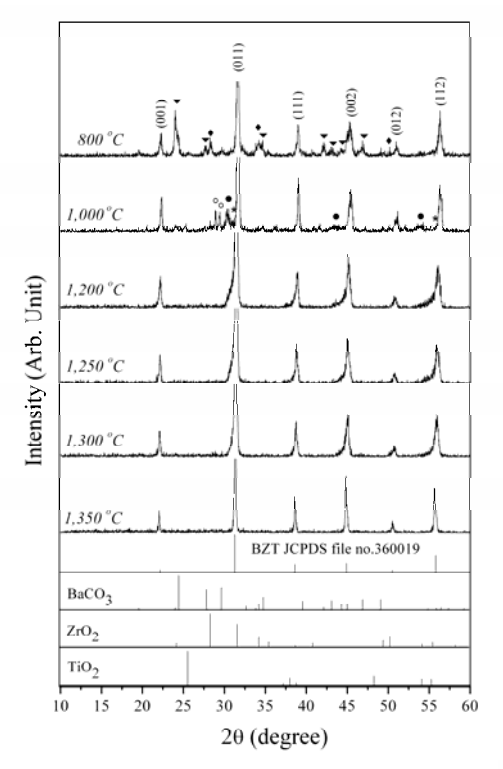


Fig.1 XRD patterns of $Ba(Zr_{0.20}Ti_{0.80})O_3$ powders: (\checkmark) $BaCO_3$; (\checkmark) ZrO_2 ; (\bullet) $BaZrO_3$; (\circ) Ba_2ZrO_4 ; (*) $BaTiO_3$.

Percentage of the perovskite phase of BZT powders as a function of calcination temperatures was calculated. The perovskite phase of 800 to 1200 °C calcined samples does not reach a hundred percent. The single phase of perovskite of the calcined samples at a temperature higher than 1250 °C is formed. The percentage of the BZT perovskite phase was increased with the increase of calcination temperatures listed in Table 1.

SEM photographs of BZT powders calcined between 800 and 1350 °C are shown in figure 2. These powders exhibit an almost spherical morphology and have a porous agglomerated form. As the temperature increased, more agglomerate particles could be observed. The average particle size tended to increase as calcination temperature increased as shown in Table 1.

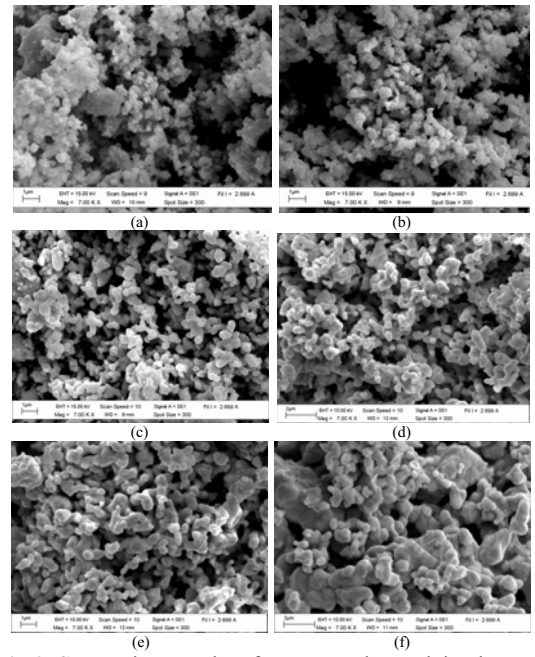


Fig.2 SEM micrographs of BZT powders calcined at (a) 800 °C, (b) 1000 °C, (c) 1200 °C, (d) 1250 °C, (e) 1300 °C and (f) 1350 °C.

Table 1 Percentage of perovskite phase and the average particle size of BZT powders.

partiele size of BZT powders.						
calcination temperature	% perovskite	average particle size				
(°C)	phase	(µm)				
800	70	0.3				
1000	74	0.4				
1200	94	0.8				
1250	100	0.9				
1300	100	1.1				
1350	100	1.5				

The phase formation behavior of the sintered ceramics is revealed by the XRD method. The XRD pattern of the BZT ceramics, with varied sintering temperatures, is shown in figure 3. This confirms that all samples were free of minor phase peaks. The BZT ceramics are identified as a single phase with a perovskite structure which has a cubic symmetry, as reported in previous investigations [18,19].

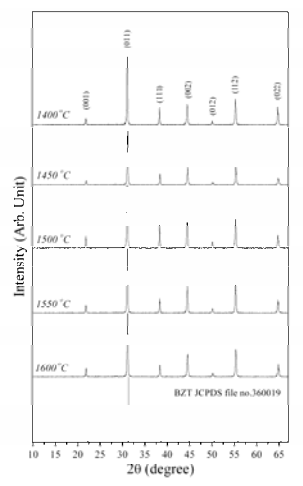
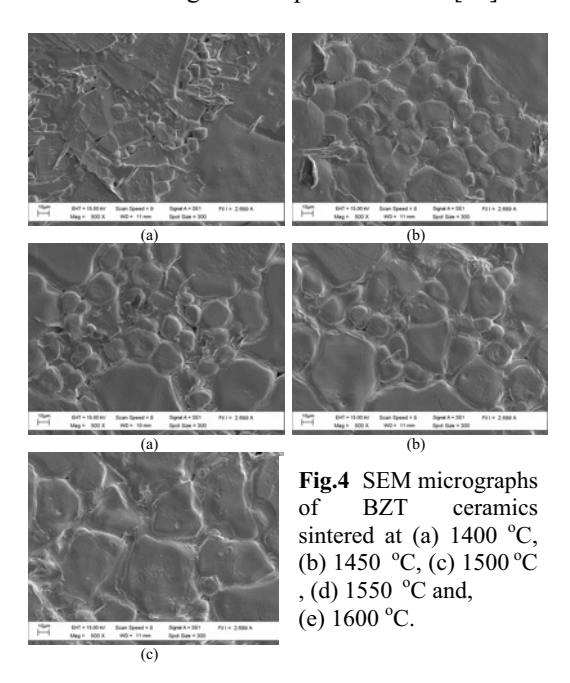


Fig.3 XRD patterns of Ba(Zr_{0.20}Ti_{0.80})O₃ ceramics.

The SEM photographs in figure 4 shows the surface of BZT ceramics at various sintering temperatures from 1400 to 1600 $^{\circ}$ C. The average grain sizes increased from 15.1 to 60.3 μ m with an increase in sintering temperature and the results also show a nonuniform distribution of grain size. These results agree with previous work [20].



The measured density and the dielectric constant at room temperature with a variation of the sintering temperatures are shown in figure 5. It can be seen that both the density and dielectric constant were first increased by sintering temperature and reached a maximum at 1500 °C and then both values were dropped when the sintering temperature was higher than 1500 °C. These results indicated that the dielectric constant is relative to the density of the ceramic.

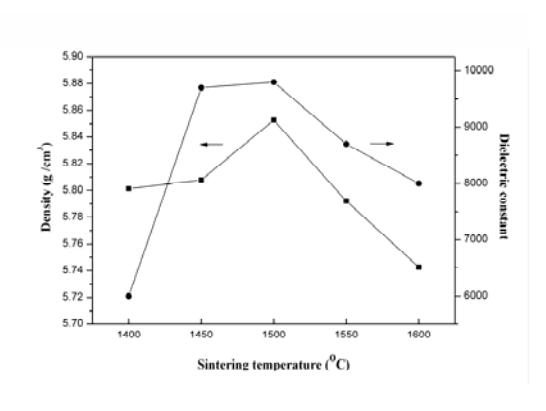


Fig. 5 Variation of dielectric constant at room temperature and density of BZT ceramics with various of sintering temperatures.

Conclusion

BZT powders can be formed through the reaction of barium carbonate, titanium (IV) oxide and zirconium (IV) oxide via calcined temperature at 1250 °C. The resulting of the BZT powders were more agglomerated as the calcination temperature increased. The BZT ceramic was identified by XRD as a single phase with a perovskite structure having cubic symmetry. The average grain size increased with an increase in sintering temperature. The maximum density and maximum dielectric constant were achieved from the ceramics sintered at 1500 °C.

Acknowledgment

This work was financial supported by the Thailand Research Fund (TRF), Faculty of Science, Naresuan University and King Mongkut's Institute of technology, Ladkrabang (KMITL). Thanks are also to the Science Lab Center, Faculty of Science, Naresuan University for facilities supporting. Acknowledgement is also given to Mr. Don Hindle for his helpful comments and correction of the manuscript.

- Clabaugh, W.S., Swiggard, R. and Gilchrist, R. Preparation of Barium Titanyl Oxalate Tetrahydrate for Conversion to Barium Titanate of High Purity. *J. Res. Nat. Bur. Stds.* 1956, 56: 289-291.
- Sakabe, Y., Minai, K. and Wakino, K. High-Dielectric Constant Ceramics for Base Metal Monolithic Capacitors. *Jpn. J. Appl. Phys. Suppl.* 1981, 20: 147-150.
- 3 Jaffe, B., Cook J., W. R. and Jaffe, H. Piezoelectric Ceramics, in Nonmetallic Solid: Series of Monographs No.3. *Academic Press, London, U.K.*, 1997, 53-57.
- 4 Nemoto, H. and Oda, I. Direct Examinations of PTC Action of Single Grain Boundaries in Semiconducting BaTiO₃ Ceramics. *J. Am. Ceram. Soc.* 1980, 63: 398-401.
- 5 Kuwabara, M., Morimo, K. and Matsunaga, T. Singer-Grain Boundaries in PCT Resistors. *J. Am. Ceram. Soc.* 1996, 79: 997-1001.
- 6 Ulrich, W., Georg, G., Ulrich, B., Sophie, W., Detlev, H. and Rainer, W. Dielectric Properties of Ba(Zr,Ti)O₃-Based Ferroelectrics for Capacitor Applications. *J. Am. Ceram. Soc.* 2001, 84: 759-766.

- 7 Brajer, E. J. Polycrystalline Ceramic Materials. U.S. Pat, 1955, No. 2 708 243.
- 8 Kulscar, F. Fired Ceramic Barium Titanate Body. U.S. Pat, 1956, No. 2 735 024.
- 9 Hennings, D., Schnell, A. and Simon, G. Diffuse Ferroelectric Phase Transitions in Ba(Ti_{1-y}Zr_y)O₃ Ceramics. *J. Am. Ceram. Soc.* 1982, 65: 539-544.
- Tang, X.G., Chew, K.H. and Chan, H.L.W. Diffuse Phase Transition and Dielectric Tunabilibty of Ba(Zr_yTi_{1-y})O₃ Relaxor Ferroelectric Ceramics. *Acta Mater.* 2004, 52: 5177-5183.
- Tang, X.G., Chew, K.H. and Chan, H.L.W. Effect of Grain Size on the Dielectric Properties and Tunabilies of Sol-Gel Derived Ba(Zr_{0.2}Ti_{0.8})O₃ Ceramics. Solid State Commun. 2004, 131: 163-168.
- 12 Powder Diffraction File No. 41-0373. International Center for Diffraction Data, Newton Square, PA, 2003.
- Powder Diffraction File No. 24-1165. International Center for Diffraction Data, Newton Square, PA, 2003.
- 14 Powder Diffraction File No. 41-0726. International Center for Diffraction Data, Newton Square, PA, 2003.
- 15 Powder Diffraction File No. 06-0399. International Center for Diffraction Data, Newton Square, PA, 2003.
- 16 Powder Diffraction File No. 24-0130. International Center for Diffraction Data, Newton Square, PA, 2003.
- 17 Powder Diffraction File No. 36-0019. International Center for Diffraction Data, Newton Square, PA, 2003.
- 18 Kbune, M., Yamakawa, K. and Yazawa, T. Barium Zirconate Titanate-Based Inorganic Dielectric Material with High Permittivity as a Lead-Free Insulator for Semiconductor Application. *Integr. Ferroelectr.*. 2005, 77: 69-78.
- 19 Verbitskaia, T.N., Zndanov, G.S., Venevtsev, I.N. and Solviev, S.P. Electrical and X-Ray Diffraction Studies of the BaTiO₃-BaZrO₃ System. *Crystallography* 1958, 3: 186-196.
- 20 Liang, R.H., Dong, X.L., Chen, Y., Cao, F. and Wang, Y.L. Dielectric Properties and Tunability of Ba(Zr_xTi_{1-x})O₃ Ceramics Under High DC Electric Field. *Ceram. Int.* 2007, 33: 957-961.

Microstructures of Dip-coated TiO₂ Thin Film Capacitor

Chanipat Euvananont¹, Jirawat Doungratsamee², Chabaiporn Junin¹, Tossapol Tippo³ and Chanchana Thanachayanont^{1*}

¹National Metal and Materials Technology Center, 114 Thailand Science Park

Paholyothin Rd., Klong 1, Klong Luang, Pathumthani 12120, Thailand

Abstract

In this paper, we investigated the effect of number of dip coating times between 1, 2 and 3 times to the capacitance properties of TiO_2 thin film capacitors. The TiO_2 thin films were directly deposited on Si substrates using dip coating technique. Single phase anatase TiO_2 dense and smooth films with small grain sizes were obtained after calcination at 450 °C for 4 hours in air. The maximum electrical capacitance obtained was 1.178 nF at 4.0 V applied voltage.

Background

Thin film capacitors are widely used in multilayer ceramic capacitors (MLCCs) and electronic integrated circuits, where they perform essential functions such as storing electric charges and blocking leakage current. For example, the MLCCs consist of ceramic dielectric layers and inner metal electrodes [1-3], which are piled up alternately leading to an equivalent circuit of several capacitors in parallel. In recent years, thin film capacitors have been predominantly used as passive component materials in electronic circuits and, in particular, they are used in most compact electronic devices, such as laptop computer, mobile phone and modern electronic gadgets.

To fabricate the dielectric thin films for thin film capacitors, titanium dioxide is a very interesting material in both of physical and chemical properties [4]. A high dielectric constant makes the material a good insulator. Stability of TiO₂ in harsh environment and elevated temperatures makes it an attractive transparent oxide semiconductor for many microelectronic applications. There have been previous attempts to prepare TiO₂ films using sol-gel technique [5-7]. In this study, the sol-gel technique via dip coating method was selected to fabricate TiO2 dielectric thin film due to main advantages of being cheap and easy to control microstructures of the films. In this study, thin TiO2 film capacitors were prepared from titanium precursor solution with various number of dipping cycles from 1 to 3 times to compare differences in film morphologies, thicknesses and its capacitive properties.

Materials and Methods

Preparation of Sol-TiO₂ Precursor Solution for Dip Coating

To obtain a stable TiO₂ sol, a precursor solution was prepared following Legrand-Buscema et al. [8]. Firstly, 0.3 M titanium- isopropoxide (TTIP, Fluka) was dissolved in isopropanol (IPA, Fluka) and stirred at room temperature for 30 mins. Then, acetylacetone (Acac, Merck) was added to make 10:3 molar ratio of titanium isopropoxide to acetylacetone. The mixture was used as chelating agent to stabilize the solution. The mixture was then stirred for 30 minutes more. Acetic acid (Labscan) was added afterwards to help initialize hydrolysis by creating esterification reaction with isopropanol. Transparent yellow solution was obtained.

Dip Coating Method Procedure

The TiO₂ precursor was used for film fabrication by dip coating technique. (1 0 0) Silicon wafer (cut into 15 x 20 x 1.5 mm³ size) was used as a substrate. The Silicon wafer pieces were ultrasonicated in DI water, acetone, ethanol and isopropanol for 15 minutes each, respectively, before dip coating in TiO₂ precursor with 1 mm./sec withdrawal speed 1, 2 and 3 times, respectively. The coated films were dried at 60 °C for 30 minutes before calcinination at 450 °C for 4 hours in air [9]. Figure 1 summarizes the film fabrication process. Aluminium electrodes were deposited using thermal evaporation both side of the TiO₂ thin film for C-V analysis measurement. Reasonably smooth and uniform TiO₂ film with the

²Department of Electronic Engineering, Mahanakorn University of Technology, Thailand

³Department of Electronic Engineering, King Mongkut Institute of Technology Ladkrabang, Thailand e-mail: chanchm@mtec.or.th

highest capacitance was selected for characterization.

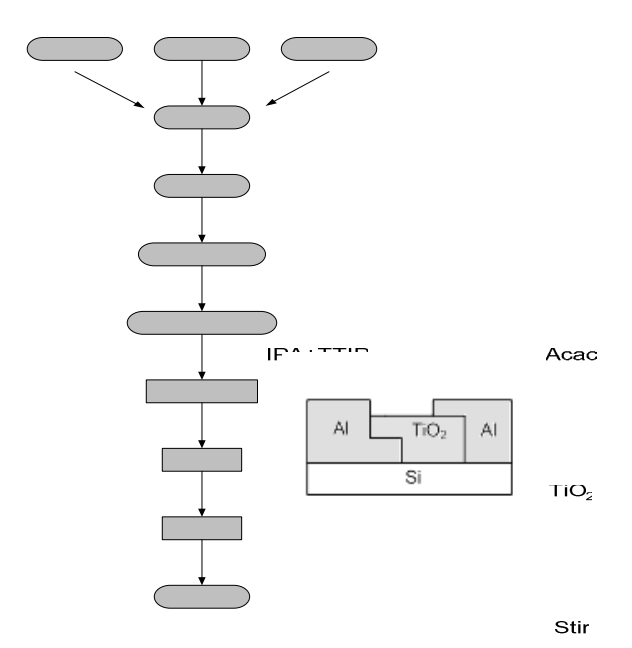


Fig. 1 Flow chart for preparation procedure of TiO_2 thin film via dip coating technique and structure of TiO_2 thin film capacitor.

Characterization

Coating Solution

Capacitive properties of TiO2 thin film capacitors were measured using C-V analyzer (Keithley CV Analyzer model 590). Morphological Eletrodes of the TiO₂ films were investigated using tapping mode Atomic Force Microscopy (AFM, Seiko instrument SPA 400) and field emission Scanning Electron Microscopy (JEOL 6321F). Film thicknesses were measured using a Dektak 3st Coating profilometer confirmed and surface Transmission Electron Microscopy (TEM, JEOL 2010FX). Crystal structures of the TiO₂ films were studied using Rigaku TTRAX III X-Drawing diffractometer (XRD). The CuKa radiation was operated at 50 kV.

Results and Discussion

Capacitance Properties

Firing

Dielectric properties of sol-gel coated TiO₂ films were studied by plotting the variation of capacitance, C, at different applied bias voltages film from 0 to 20 V with 0.05 V stepping and a frequency of 100 Hz applied across the samples. The C-V plots of the films dipped 1,2 and 3 times are shown in figure 2.

From figure 2, maximum capacitances obtained from each film were 1.072nF at 5.1 Volt, 1.060nF at 3.5 Volt and 1.178 nF at 4.0 Volt for number of dip coating 1, 2 and 3 times, respectively. The capacitance values of all the TiO_2 films are not very different because the thickness of the TiO_2 films increases only slightly with increasing

dipping cycle. The 3-time dip coated TiO₂ film was selected for characterization due to its highest maximum capacitance among the three samples.

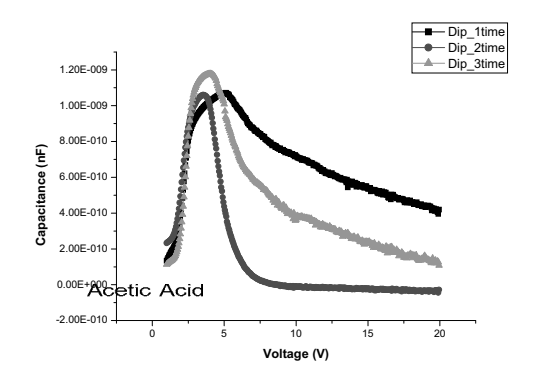


Fig.2 C-V plot of TiO₂thin film with different number of coating times

Microstructure and Thickness of the TiO₂ Films

Figure 3 shows the XRD pattern of the 3-time dip coated TiO_2 film. The result indicates that the film consists of only pure anatase phase after calcination at 450°C for 4 hours in air atmosphere. Figures 4 and 5 show surface morphologies of 3-time dip coated TiO_2 film using AFM and SEM, respectively. Uniform grain size within a range of 20-30 nm and very smooth dense film having roughness of around 1 nm were obtained.

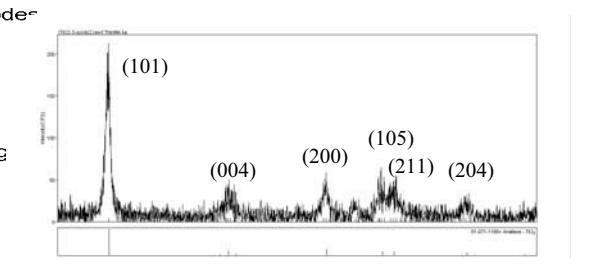


Fig.3 XRD pattern of TiO_2 film dip coating 3times after calcine at 450 °C for 4 hrs.

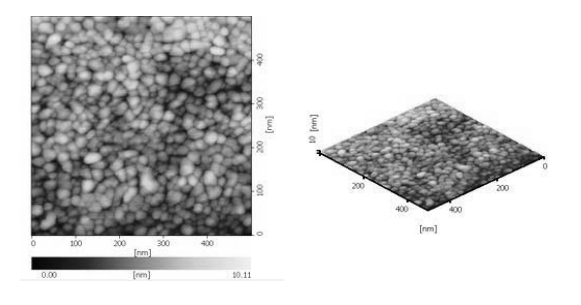


Fig.4 AFM images of surface of 3-time dip coated TiO₂ film after calcination at 450 °C.

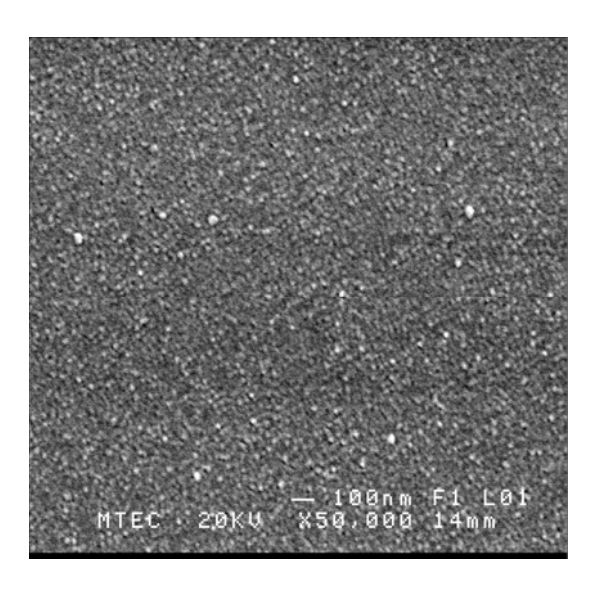


Fig.5 An SEM micrograph of the surface of 3-time dip coated TiO₂ film after calcinination at 450 °C for 4 hrs.

Figure 6 shows a cross-sectional TEM micrograph of the 3-time dip coated TiO_2 film. The result indicates that dipping titanium dioxide precursor 3 times provides single uniform TiO_2 layer after calcination. The film thickness of 78 nm was obtained. Unfortunately, we could not increase the capacitance by dipping more than 3 times to increase the film thickness because the TiO_2 film cracked and may cause leakage current when performing as a dielectric layer of the thin film capacitors.

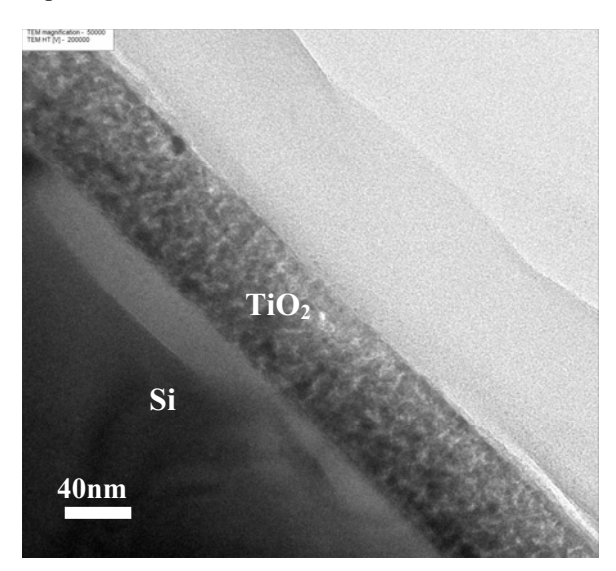


Fig.6 A cross-sectional TEM image of 3-time dip coated TiO₂ film after calcinination at 450 °C for 4 hrs.

Conclusion

Dielectric TiO_2 thin film capacitors have been prepared successfully by dip-coating the TiO_2 films from TiO_2 sol-gel precursor. The maximum capacitance was obtained from 3-time dip coated TiO_2 film because of the pure phase, thick, uniform and smooth microstructure.

Acknowledgment

Authors would like to thank the National Metal and Materials Technology Center for financial support (MTEC Grant No. MT-B-48-CER-07-187-I) and Miss Viyaporn Krongtong for her help on SEM imaging.

- 1. Hino T, Matsumoto N, Nishida M, Araki T. PLD of X7R for thin film capacitors. *Applied Surface Science* 2007, doi:10.1016/j.apsusc.2007.10.001.
- 2. Juan P C et al. The effect of annealing temperature on the electrical properties of metal-ferroelectric (PbZr0.53Ti0.47O3)-insulator (ZrO2)-semiconductor (MFIS) thin-film capacitors. *Micro Electronic Engineering* 2007, 84: 2014-2017.
- 3. Lin-Jung Wu, Jenn-Ming Wu, Thickness-dependent dielectric properties of nanoscale Pt/(Pb,Ba)ZrO₃/BaPbO₃ capacitors. *Journal of Crystal Growth*. article in press. accepted 30 August 2007.
- 4. Mo S D, Ching W Y, Electronic and optical properties of three phases of titanium dioxide: Rutile, anatase, and brookite. *Phys. Rev.* 1995, B 51 (19): 13023-13032.
- 5. Young Jin Yun et al. Low-temperature coating of sol-gel anatase thin films. *Materials Letter* 2004, 58: 3703-3706.
- 6. Cui H, Shen H S, Gao Y-M, Dwight K and Wold A. Photocatalytic properties of titanium (IV) oxide thin films prepared by spin coating and spray pyrolysis. *Materials Research Bulletin* 1993, 28 (3): 195-201.
- 7. Gao Y M, Shen H S, Dwight K and Wold A. Preparation and photocatalytic properties of titanium(IV) oxide films. *Materials Research Bulletin* 1992, 27 (9): 1023-1030.
- 8. Legrand–Buscema C, Malibert C and Bach S. Elaboration and characterization of thin films of TiO₂ prepared by sol-gel process. *Thin Solid Films* 2002, 418: 79-84.
- 9. Guillard C, Debayle D, Gagnaire A and Jaffrezic H. Physical properties and photo catalytic efficiencies of TiO₂ films prepared by PECVD and sol-gel methods. *Materials Research Bulletin* 2004, 28: 1445-1458.

Collagen Measurement and Staining Pattern of Wound Healing Comparison with Fixations and Stains

S. Ukong¹, S. Ampawong^{2*}, and K. Kengkoom³

e-mail: a sumate@hotmail.com

Abstract

Several studies have measured collagen fiber with advance imaging techniques. Unfortunately these are performed by complicated methods and with specific tools. In seeking out the easier ways in routine histopathological laboratory, collagen measurements and staining patterns of wound healing comparison with fixatives (10% Neutral Buffer Formalin; NBF and Bouin's solution) and stains (Hematoxylin & Eosin; H&E and Masson's trichrome) were observed in Sprague Dawley rat. Wound characteristics were measured running under image analysis program, ImageJ, NIH. The result showed that moderate effects of fixatives on staining intensity of collagen fiber and staining pattern were observed in healing wound. 10% NBF fixed specimens were stained on collagen fiber less intensely than Bouin's solution. However there were no effects of fixatives on basic architecture such as size and length of neovascularied vessels and epithelial tongue respectively. We preliminarily conclude that Bouin's fixative is appropriate to fix tissue for measuring collagen fiber because of its color enhancement property. The most important of our results is used to application for assessment the pharmacological products which promote new collagen fibers formation and wound healing.

Background

Histopathological studies of wound healing process are normally used for evaluation the efficacy of pharmacological products which promote dermal skin substitutes (Truong N.T and et al., 2005; Bae and et al., 2005; Roh and et al., 2006; Rao and et al., 2007). Those studies are related to phases of cutaneous wound repairing which have been divided into three phases: inflammation (early and late), proliferation, and remodeling (Clark 1996; Martin 1997). Several wound characteristics are considered to determine the level of histopatological changing e.g. the depth length of healed wound, epithelial incorporation of the stratification, substitute, degree of neutrophil, macrophage, fibroblast, and foreign body giant (FBG) cell infiltration, extent of elastin formation (Truong N.T and et al., 2005). One of the most important wound characteristic to be measured was collagen fiber (Gogly and et al., 1997; Ballas & Davidson 2001; Truong N.T and et al., 2005; Rao and et al., 2007). Because of its property, plays a dominant role in maintaining the structural integrity and healing wound (Myllyharju & Kivirikko 2001). Many studies attempt to quantify the amount of collagen changing and orientation in any stages of wound healing, epipolarization microscope

picrosirius red-stained (Noorlander and et al., 2002), computer vision analysis of collagen fiber bundles (Elbischger and et al., 2004; Elbischger and et al., 2005), Fourier Transform Infrared (FTIR) spectral imaging (Potter and et al., 2001), and laser scanning confocal microscopy (Taylor and et al., 2002). However, all of these methods are complicate steps, using some special equipments and non available in routine histopathology laboratory unit.

The aim of this study was to measure the wound characteristics with imaging analysis program, ImageJ NIH (Girish & Vijayalakshmi 2004; Irving and et al., 2007) as a tool to quantify the area of interest especially collagen. This software package is accessible online at http://www.sbes.vt.edu/tools.htm. All of specimens were fixed both in 10% NBF and Bouin's solution in any difference stains, H&E and Masson's Trichrome.

Materials and Methods

Animals and Surgery

Six male outbred Sprague Dawley rat (8 weeks, 250±10 g) were used. The study was reviewed and approved by the Institutional Animal Care and Use

¹Department of Biology, Faculty of Science, Silpakorn University, Nakhon Pathom, Thaliland

²Quality Development Division, National Laboratory Animal Centre, Mahidol University (NLAC-MU), Nakhon Pathom, Thailand

³Production and Service Division, National Laboratory Animal Centre, Mahidol University (NLAC-MU), Nakhon Pathom, Thailand

Committee. Attending veterinarian care program was performed to reach the animal welfare acts. Animal were housed under clean conventional system in suspended cages/wire bottom and fed adlibitum. All survival surgery was performed using aseptic technique. Anesthesia consisted of Zoletil® (30 mg/kg) administered intramuscularly needed maintain deep anesthesia. to Standardized full thickness 15×15 mm² skin wounds (removing the subcutaneous layer) were excised both sides of the anterior dorsum of each anesthetized rat. Wound dressing with Tegaderm[®], clean with normal saline and betadine[®], were take placed everyday.

Specimens Processing

Healing wounds were collected after euthanized with over dose intraperitoneally of Thiopentone on day 7th. Divided healing wounds of both sides were fixed in 10% NBF 8hr, room temperature and Bouin's solution 48hr, room temperature (Presnell and Schreibman, 1997). The tissues were embedded in paraffin and sectioned at 6-7 μm . Alternate slides of each specimen were submitted to H&E stain (Harris, 1900) and Masson's Trichrome (Masson, 1929) for terminology collagen.

Gross and Histologic Measurements and Assessments

From each specimen, colour images of 640x480 pixel resolution were acquired with a light microscope (BX51, Olympus®) and digital camera (Moticam 1000, Moticam®) running under imaging analysis program (ImageJ, NIH). The collagen fiber intensity, surface area of neovascularization, and staining pattern of epithelial layer of skin and subcutaneous muscle were measured for comparison between fixations and stains. All of wound characteristics were quantified by Red-Blue-Green; RBG color histogram (figure 1A) and measure mode (figure 1B).

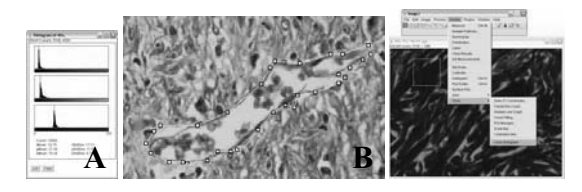


Fig.1 [A] The collagen fiber intensity was measured by color histogram mode, the red, blue, and green color intensity was showed as a result. Blue:green ratio was calculated as the comparison criteria. [B] Quantify the surface area of neovascularization was measured by analyse- area measure mode; Masson's Trichrome staining, 400x magn.

Data Analysis

Data are presented as mean values \pm SEM were calculated. The normality of the data was analyzed by the Kolmogorov – Smirnov test. Statistical comparisons with fixations were made by Student's t test in normal data. The non-parametric test Mann-Whitney was applied in non-normal data. The level of significance accepted was p < 0.05.

Results and Discussion

Skin wound full thickness had developed to proliferation and/or early remodeling phase after 7 days. As obviously could be seen the new vascularized vessels and collagen fibers formation. Under conventional light microscope, the collagen fibers had under clearly observation in both normal skin and wound area (figure 2). The arrangement of the collagen visible in the sections showed that the intensity and width in wound area are less than normal skin. Together with the collagen fiber plays a dominant role in maintaining the structural integrity and healing wound (Myllyharju & Kivirikko 2001). By this reason, several studies have been normally measured collagen content to quantified dermal wound recovering for application to pharmacological products as toxicity and efficacy test (Truong N.T and et al., 2005; Bae and et al., 2005; Roh and et al., 2006; Rao and et al., 2007).

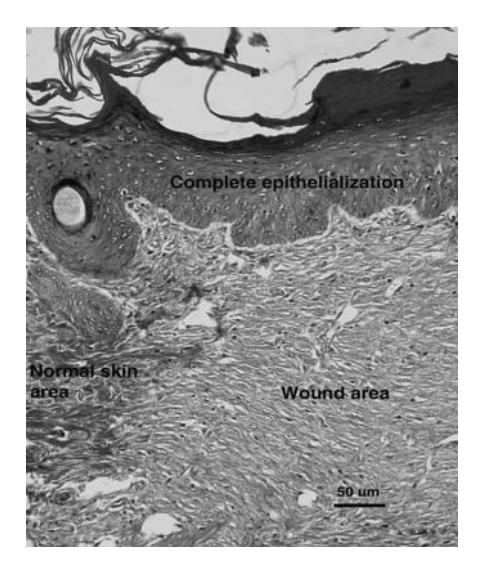


Fig.2 Photomicrograph of the complete epithelialization of wound with Masson's Trichrome staining, 100X magn., note that collagen intensity (blue) in wound area is less than normal skin area.

Staining intensity in epithelial layer of skin and subcutaneous muscle is shown in Table 1. Under H&E and Masson's trichrome, epithelial layer staining pattern which fixed in 10% NBF were less intensely than Bouin's solution. According to the intensity of RBG color, eosinophilic shade of red color on epithelial layer and keratinized material in

Bouin's solution is significantly higher than 10% NBF (figure 3; A-D). Similar to the result of the collagen measurement, in both normal skin and wound had low intensity in 10% NBF (figure 4; A-F). The blue shade of aniline blue on collagen fiber in Bouin's solution is significantly higher than 10% NBF. However there was no difference intensity of muscle fiber between both fixatives. The intensity of acidic dye of Biebrich scarlet on subcutaneous muscle in both fixatives was not difference (figure 3; E-F). The results are showed that there was moderate fixative effect on the staining pattern and color intensity because of its enhancement properties (Presnell and Schreibman, 1997).

The results are shown that there was no fixative effect on the basic architecture. The length of epithelial tongue was not significant different, between both fixatives (figure 4; G-I). Resemble to the magnitude, there was no difference on the size of neovascularized vessel at any sections direction, except longitudinal once (figure 4; J-L). We should be measured neovascularization, numerous capillaries arise from blood vessels adjacent to the

wound that invade the wound neodermis, because the formation of new blood vessels is necessary to sustain the newly formed granulation tissue (Madri and et al., 1996).

Dielectric TiO_2 thin film capacitors have been prepared successfully by dip-coating the TiO_2 films from TiO_2 sol-gel precursor. The maximum capacitance was obtained from 3-time dip coated TiO_2 film because of the pure phase, thick, uniform and smooth microstructure.

Further study, we intend to measure other wound characteristics which perform by image analysis program on analyzed particle mode such as (1) monocytes & neutrophils counting since they are the source of pro-inflammatory cytokines that probably serve as some of the earliest signals to activate local fibroblasts and keratinocytes (Pierce and et al., 1991; Hubner and et al., 1996) (2) macrophages since they are essential for effective wound healing (Leibovich and et al., 1975) (3) fibroblasts are responsible for the synthesis, deposition and remodelling of the extracellular matrix (Singer & Clark 1999).

Table 1 Staining pattern of epithelial and subcutaneous muscle in difference staining between 2 fixatives.

Stain	Zone	Fixative]	Red inten	sity	p value	H	Blue inten	sity	p value
			n	Mean	SEM		n	Mean	SEM	
H&E	Epithelial	Bouin's	20	1.59	0.01	0.000	20	1.47	0.01	0.98
		10%NBF	13	1.42	0.02		13	1.47	0.04	
	Epithelial	Bouin's	14	1.93	0.12	0.005	14	1.52	0.10	0.007
Trichrome		10%NBF	19	1.55	0.05		19	1.20	0.05	
	Muscle	Bouin's	18	1.9	0.06	0.15	18	1.11	0.03	0.69
		10%NBF	20	2.1	0.08		20	1.30	0.04	

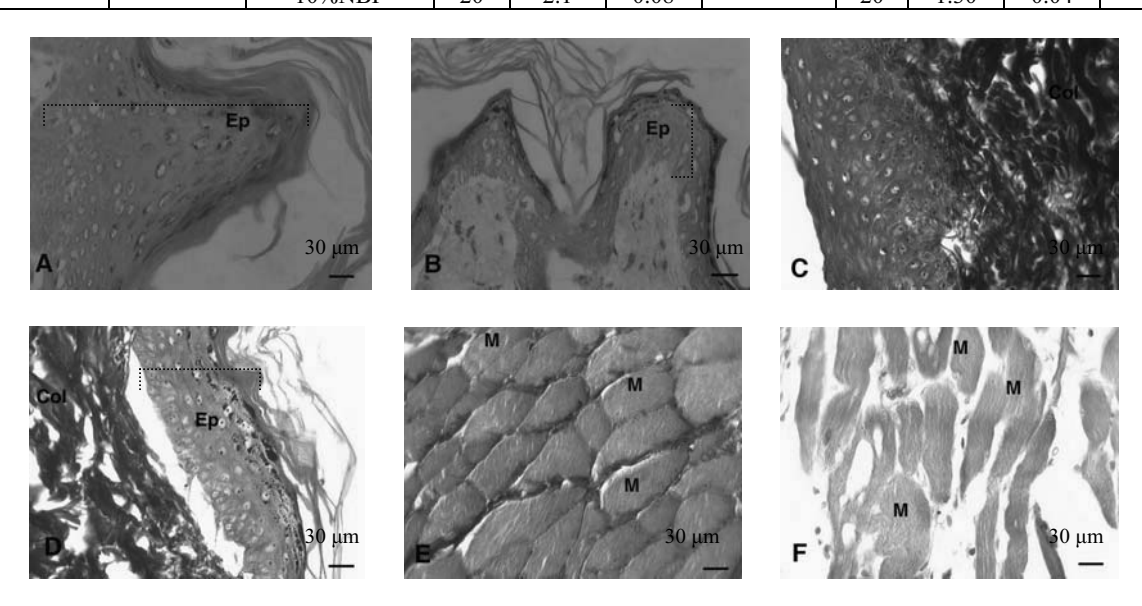


Fig. 3 The photomicrograph of staining pattern, 400X magn, epithelial layer with H&E staining in Bouin's solution **[A]** and 10% NBF **[B]**. Epithelial layer and subcutaneous muscle with Masson's Trichrome staining, in Bouin's solution **[C,E]** and 10% NBF **[D,F]**.Ep; epithelial layer, Col; collagen fiber, M; subcutaneous muscle.

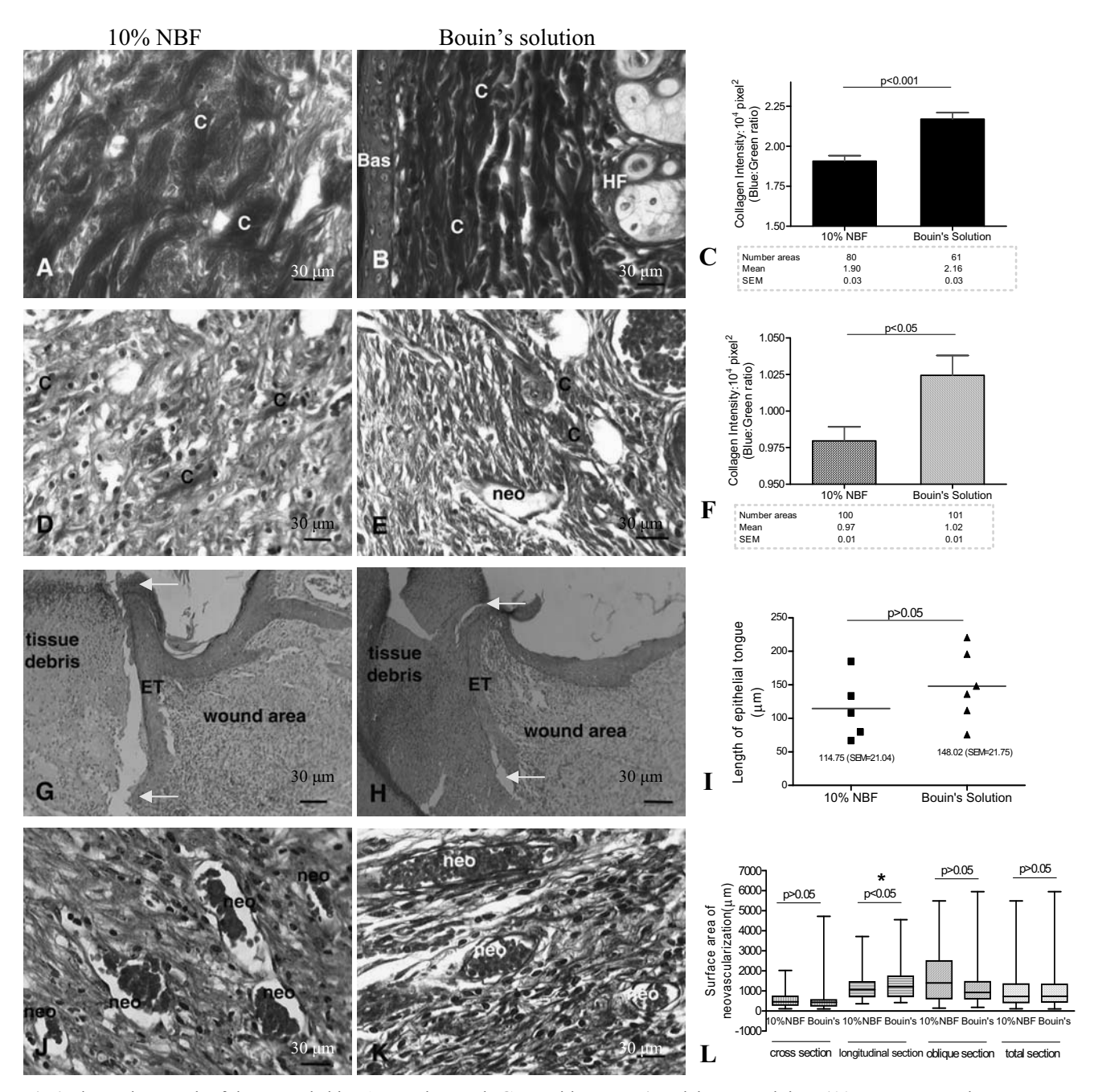


Fig.3 Photomicrograph of the normal skin **[A,B]** and wound **[G,H]** with Masson's Trichrome staining, 400X magn, note that 10% NBF **[A,D]** exhibit collagen (C) intensity lower than Bouin's solution **[B,E]**. HF; hair follicle, Bas; stratum basale, **[G,H]** Photomicrograph of the wound with H&E staining, 400X magn, showed that the length of epithelial tongue between both fixatives is equal, arrow indicate epithelial tongue (ET) edge. **[J,K]** Photomicrograph of the wound with Masson's Trichrome staining, 400X magn, exhibit surface area of neovascularization (neo) between both fixatives is equal.

Conclusion

Collagen measurement is normally used for application to pharmacological products as toxicity and efficacy test. Measurement by image analysis program, ImageJ, NIH provided an efficient tool for morphometric study and could be performed in routine histopathological laboratory with no more complicated methods and special tools except conventional light microscope. There was no fixatives effect on the basic architecture. Conversely, there was moderate fixatives effect on

the staining pattern and color intensity. Bouin's fixative is appropriate to fix tissue for measuring collagen fiber because of its enhancement property.

Acknowledgment

We would like to thank and deep appreciate to Colonel Dr. Piboon Phunyarit, Pathological Institute, Phramongkutklao Medical Centre Division, The Royal Thai Army Medicine Department that kindly provided some cytochemistry dyes.

- 1. Bae, J.S., Jang, K.H., Park, S.C. and Jin, H.K. Promotion of dermal wound healing by polysaccharides isolated from Phellinus gilvus in rats. *J. Vet. Med. Sci.*, 2005, 67(1):111-114.
- Ballas, C.B. and Davidson, J.M. Delayed wound healing in aged rats is associated with increased collagen gel remodeling and contraction by skin fibroblasts, not with differences in apoptotic or myofibroblast cell populations. Wound Repair Regen., 2001, 9(3):223-237.
- 3. Elbischger, P. J., Bischof, H., Regitnig, P., and Holzapfel, G. A. Automatic analysis of collagen fiber orientation in the outermost layer of human arteries. *Pattern Anal. Applic.*, 2004, 7: 269–284.
- 4. Elbischger P.J., Bischof, H., Holzapfel, and G.A., Regitnig, P. Computer vision analysis of collagen fiber bundles in the adventitia of human blood vessels. *Stud. Health Technol. Inform.*, 2005, 113:97-129.
- Girish, V. and Vijayalakshmi, A. Affordable image analysis using NIH Image/ImageJ. *Indian J. Cancer*, 2004, 41(1):47.
- Gogly, B., Godeau, G., Gilbert, S., Legrand, J. M., Kut, C., Pellat, B. and Goldberg, M. Morphometric analysis of collagen and elastic fibers in normal skin and gingiva in relation to age. Clin. Oral Invest., 1997, 1: 147–152.
- 7. Harris, H.F. Haematoxylin into haematein in staining reactions. *Appl. Microsc. Lab. Meth.*, 1900, 3:777-780.
- 8. Irving, B.A., Weltman, J.Y., Brockm, D.W., Davis, C.K., Gaesser, G.A. and Weltman, A. NIH ImageJ and Slice-O-Matic computed tomography imaging software to quantify soft tissue. *Obesity (Silver Spring)*, 2007, 15(2):370-376.
- 9. Leibovich, S.J. and Ross, R. The role of the macrophage in wound repair. A study with hydrocortisone and antimacrophage serum. *Am. J. Pathol.*, 1975, 78(1):71-100.
- Madri, J.A., Sankar, S. and Romanic, A.M. Angiogenesis. In: Clark RAF, ed. *The Molecular and Cellular Biology of Wound Repair*. New York: Plenum Press., 1996, p. 355.
- 11. Masson, P. Some histological methods. Trichrome staining and their preliminary

- technique. *Bulletin of the International Association of Medicine*, 1929, 12:75.
- 12. Myllyharju, J. and Kivirikko, K.I. Collagens and collagen-related diseases. *Ann. Med.*, 2001, 33(1):7-21.
- 13. Noorlander, M.L., Melis, P., Jonker, A. and Van Noorden, C.J. A quantitative method to determine the orientation of collagen fibers in the dermis. *J. Histochem. Cytochem.*, 2002, 50(11):1469-1474.
- Pierce, G.F., Mustoe, T.A., Altrock, B.W., Deuel, T.F., and Thomason, A. Role of platelet-derived growth factor in wound healing. *J. Cell Biochem.*, 1991, 45(4):319-326.
- Potter, K., Kidder, L.H., Levin, I.W., Lewis, E.N., and Spencer, R.G.S. Imaging of Collagen and Proteoglycan in Cartilage Sections Using Fourier Transform Infrared Spectral Imaging. *Arthritis & Rheumatism.*, 2001, 44(4):846-855.
- Presnell, J.K. and Schreibman, M.P. Fixative. Humason's Animal tissue techniques. Baltimore: Johns Hopkins University Press. 1997, 14 – 28.
- 17. Rao, K.S., Patil, P.A. and Malur, P.R. Promotion of cutaneous wound healing by famotidine in Wistar rats. *Indian J. Med. Res.*, 2007, 125(2):149-154.
- Roh, DH, Kang, S.Y., Kim, J.Y., Kwon, Y.B., Young Kweon, H., Lee, K.G., Park, Y.H., Baek, R.M., Heo, C.Y., Choe, J. and Lee, J.H. Wound healing effect of silk fibroin/alginateblended sponge in full thickness skin defect of rat. J. Mater Sci Mater Med., 2006, 17(6):547-52.
- 19. Singer, A.J. and Clark, R.A. Mechanisms of Disease: Cutaneous Wound Healing. *N. Engl. J. Med.*, 1999, 341: 738-745.
- Taylor, M.D., Roberts, J.R., Hubbs, A.F., Reasor, M.J. and Antonini, J.M. Quantitative image analysis of drug-induced lung fibrosis using laser scanning confocal microscopy. *Toxic. Sci.*, 2002, 67:295-302.
- 21. Truong, N.T., Vern, A.K., Latenser, B.A., Wiley, D.E., and Walter, R.J. Comparison of Dermal Substitutes in Wound Healing Utilizing a Nude Mouse Model. *J. Burns Wounds.*, 2005, 14;4:e4:72-82.

Effect of Polysaccharide from *Phellinus ignarius* (L.) Quél. on Hematological Values and Blood Cell Characteristics in Diabetic Rats

C. Talubmook*

Faculty of Environment and Resource Studies and Department of Biology, Faculty of Science, Mahasarakham University, Maha Sarakham 44150, Thailand e-mail: chusri.t@msu.ac.th

Abstract

The effect of polysaccharide from *Phellinus ignarius* (L.) Quél. (PI) on the packed cell volume, hemoglobin concentration, red and white blood cell counts, and also the blood cell characteristics was investigated in streptozotocin-induced diabetic rats. PI at a dose of 100 mg/kg b.w. was injected venously daily to the diabetic rats for seven weeks. The results showed that PI decreased the pack cell volume, hemoglobin concentration, red blood cell count, and diameter of red blood cells but not white blood cell count. In addition, PI showed some alteration of the blood cell characteristics in diabetic rats. These data indicated that long term administration of PI changed some hematological values and some characteristics in diabetic rats.

Background

Diabetes mellitus is a metabolic disorder disease characterized by high blood glucose levels, which result from defects in pancreatic insulin and/or impaired target-cell secretion responsiveness to insulin [1]. This disease is characterized by chronic hyperglycaemia and other metabolic abnormalities and sometimes accompanied by symptoms of polydipsia, polyuria, polyphagia complications affecting various organs in the body such as the eye, kidney, nervous system and blood vessels. Hematological complications consist mainly of abnormalities in the function, morphology and metabolism of erythrocytes, leukocytes and platelets [2]. Treatment of diabetes mellitus and its complications in the recent context have focused on the usage of plant extracts [3]. Antihyperglycaemic activities of plant extracts and an extract from Phellinus ignarius (L.) Quél., mushroom, a member of Hymenochaetaceae, have been reported. However, the safety of extract in such treatment is still unclear whether it has any side effect(s). Moreover, the effect of the extract from PI. on hematology has not yet been demonstrated. Therefore, the effect polysaccharide from PI. on hematological values and blood cell characteristics in diabetic rats was carried out.

Materials and Methods

Preparation of PI

The polysaccharide from PI was kindly given by Frankie Chan from Thai-Korea Natural Phellinus Mushroom Research Center. On the day of experiment, polysaccharide at a given dosage was dissolved in 2 ml normal saline before intravenous injection to the diabetic rats.

Animals

Animals used in this study were male albino Wistar rats weighting 150-220 g purchased from the Animal Resource, National Research Council Thailand. The rats were acclimatized in an air conditioned room at 22-28 °C for five days and given a standard chow and watered *ad libitum* prior to the commencing experiments. The rats were maintained in accordance with the guidelines of the Committee on Care and Use of Laboratory Animal Resource, National Research Council Thailand. The experiments performed on the rats were performed in accordance with the advice of the Institutional Animal Care and Use Committee MSU.

Induction of Diabetes

The rats were injected intraperitonealy with a single dose of 65 mg/kg b.w. streptozotocin (STZ, Sigma Chemicals, St. Louis, MO) freshly dissolved in 20 mM citrate buffer adjusted pH to 4.5. After STZ injection, they were provided with a 2% sucrose solution as their drink for 48 hours to alleviate the severity after initial hypoglycemic phase. Blood glucose levels were assessed three days after STZ injection to confirm the diabetic stage. Rats with blood glucose level of at least 200 mg/dl were used in the experiment [4].

Experimental Design

The experiment consisted of 4 groups;

Group 1: Control rats received 2 ml normal saline

Group 2: Diabetic rats received 2 ml normal saline

Group 3: Diabetic rats received 0.25 mg/kg b.w. glibenclamide

Group 4: Diabetic rats received 100 mg/kg b.w. PI

The rats were administered once daily for seven weeks. At the end of the experiment, the rats were anesthetized with ether. Blood samples obtained from the tail vein of animals were used for the determination of hematological values. The blood cell characteristics and ultrastructure were also monitored.

Hematological Values

Hematological values were examined in according with the protocol used by Chomko and Talubmook [5]. Blood sample was filled in heparinised capillary tube and centrifuged at 1,500 rpm for 5 min. After centrifugation, the capillary tube was placed in microhematocrit reader and the packed cell volume (PCV) was determined. The hemoglobin concentration was determined using Sahli method, hematin obtained from the reaction of hemoglobin and hydrochloric acid was compared with the standard hematin. Total red and white blood cell counts were examined manually using hemocytometer after the blood was diluted. The diluting solution for red blood cell was Gower's solution but for the white blood cell was Turk's solution.

Light Microscopic Specimen Preparation

Blood smear was fixed in methanol and stained with Wright-Giemsa stain for morphological study of white blood cells.

Ultrastructure of Blood Cells

Investigation of ultrastructure of blood cells was performed with the aid of the Scanning Electron Microscope. Specimens were fixed in Karnovsky's fixative, and dehydrated in an acetone series. Dried specimens were mounted on stubs, coated with gold and viewed in Scanning Electron Microscope (JEOL6460LV) [6].

Statistical Analysis

The results of hematological values and the length and width of blood cells were presented as the mean \pm SEM. Comparisons were made between control and treatment groups using one-way analysis of variance (ANOVA) followed by

Duncan's New Multiple Range Test. Values of p < 0.05 were regarded as statistical significant.

Results and Discussion

The homological values of controls, diabetic controls and diabetic rats treated with PI were shown in Table 1.

The packed cell volume from PI treated rats was not different from diabetic control and glibenclamide treated rats but was significantly (p<0.05) less than that from normal controls. The hemoglobin concentration was also significantly (p<0.05) less than the control, diabetic control and glibenclamide treated rats. In addition, the red blood cell count was significantly (p<0.05) less than normal controls and glibenclamide treated rats. In contrast, the white blood cell count was significantly (p<0.05) higher than the controls and glibenclamide treated rats. Nevertheless, the red and white blood cell counts were not different from the diabetic controls.

Table 1 Hematological values of controls, diabetic controls, diabetic rats treated with glibenclamide, and diabetic rats treated with PI.

Groups	PCV (%)	Hb (g/dl)	RBC (x10 ⁶ cell/µl)	WBC (x10³cell/µl)
control	53.00 <u>+</u> 1.06 ^b	21.33 <u>+</u> 0.21	8.67 <u>+</u> 0.37 ^b	5.63 <u>+</u> 0.22 ^a
Control	ab		ab	b
diabetic control	51.00 <u>+</u> 0.89 ab	21.16±0.47	7.85±0.30 ab	7.11 <u>±</u> 0.53 ^b
glibenclamide	50.50 <u>+</u> 1.58 ^{ab}	20.66 <u>+</u> 0.49	8.58 <u>+</u> 0.34 ^b	4.41 <u>+</u> 0.62 ^a
	40.50 1.70 8	10 22 10 22	(51:0748	7.62+0.50 b
Phellinus ignarius	48.50 <u>+</u> 1.72 ^a	19.33 <u>+</u> 0.33	6.51 <u>+</u> 0.74 ^a	7.62 <u>+</u> 0.50 ^b

Means \pm SEM within the same column followed by the different letters are significantly different at p<0.05. Abbreviations: PCV packed cell volume, Hb hemoglobin, RBC red blood cell, WBC white blood cell.

Table 2 Diameter of the red blood cells in of controls, diabetic controls, diabetic rats treated with glibenclamide, and diabetic rats treated with PI.

Groups	Diameter of red blood cell (µm)
control	5.40 <u>+</u> 0.10 ^{ab}
diabetic control	5.62 <u>+</u> 0.10 ^b
glibenclamide	5.57 <u>+</u> 0.11 ^b
Phellinus ignarius	5.17+0.12 ^a

Means \pm SEM within the same column followed by the different letters are significantly different at p<0.05.

Table 2 showed that the diameter of red blood cells from PI treated rats was significantly (p<0.05) smaller than those from controls, diabetic controls and glibenclamide treated rats. Figure 1 presented different characteristics of the young and old red blood cells from controls, diabetic controls, glibenclamide treatment and diabetic rats treated with PI. The red blood cells of all rats were non-nucleated biconcave disk. The old ones were small and had a prominent central pallor. However, the

red blood cell characteristics from all experimental rats were not significantly different. Figure 2 showed the smooth membrane red blood cells and the knobby white blood cells. Nevertheless, the red and white blood cells of all experimental rats were not different. Figure 3 illustrated the white blood cells; lymphocytes, monocytes, neutrophils, and eosinophils. Significant differences of all types of white blood cells from experimental rats were not found.

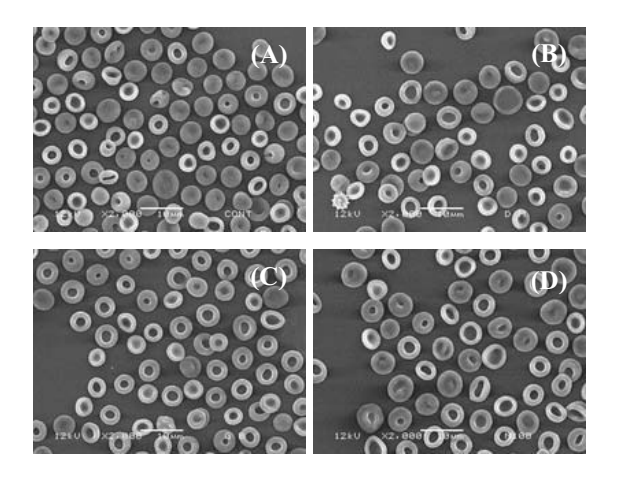


Fig. 1 Scanning electron micrographs of red blood cells from controls (A), diabetic controls (B), diabetic rats treated with glibenclamide (C), and diabetic rats treated with PI (D).

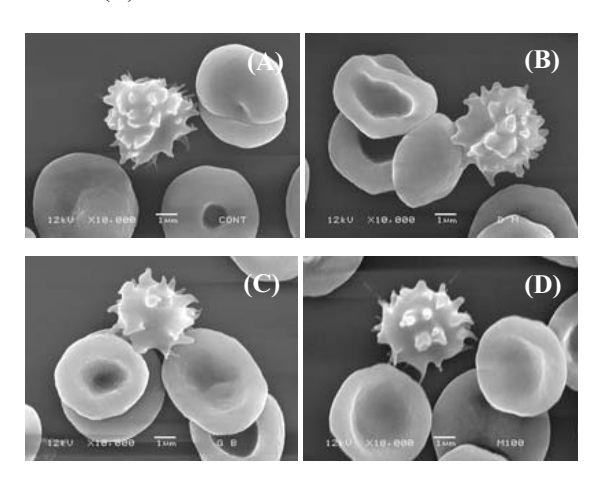


Fig. 2 Scanning electron micrographs of red and white blood cells from controls (A), diabetic controls (B), diabetic rats treated with glibenclamide (C), and diabetic rats treated with PI (D).

Groups	Lymphocytes	Monocytes	Neutrophils	Eosinophils
A				
В				
C	•			
D				

Fig. 3 White blood cells from controls (A), diabetic controls (B), diabetic rats treated with glibenclamide (C), and diabetic rats treated with PI (D). bars = $10 \mu m$

Conclusion

In conclusion, the overall results showed that long-term treatment of PI altered some hematological values but not ultrastructure of blood cells in diabetic rats.

Acknowledgment

This research was supported by grant from the development research division and Faculty of Science, Mahasarakham University, Thailand. The author would like to thank Dr. Savittree Wongtangthintarn for her help. Thank also go to Areeya Suchantabud and Thanutchaporn Mahanarm for technical assistance.

References

1. Talubmook, C. The influence of elevated glucose levels and the diabetic state on neuromuscular function in the gut, Hatfield: University of Hertfordshire, 2002, (Ph.D. thesis).

- Comazzi, S., Spagnolo, V. and Bonfanti, U. Erythrocyte changes in canine diabetes mellitus: in vitro effects of hyperglycaemia and ketoacidosis. *J Comp Clin Path.* 2004, 12: 199-205.
- 3. Kamalakkannan, N. and Mainzen, P.S. Rutin improves the antioxidant status in streptozotocin-induced diabetic rat tissues. *J Mol Cell Biochem.* 2006, 293: 211-219.
- 4. Talubmook, C., Forrest, A. and Parsons, M. Streptozotocin-induced diabetes modulates presynaptic and postsynaptic function in the rat ileum. *Eur J Pharmacol*. 2003, 469: 153-158.
- 5. Chomko, S. and Talubmook, C. Effect of leaf extracts from *Morus alba* and *Annona squamosa* on hematological values in diabetic rats. *J Sci and Technol. MSU*. 2007, 26: 167-173.
- Ponsen, S., Narkkong, N-A. and Angwanich, W. Morphological and ultrastructural observations on the blood cells of Sand Lizards (*Leiolepis* belliana Rubritaeniata) Mertens 1961. J Anim Vet Adv. 2007, 6(4): 522-527.

Microscopy and Image Analysis Techniques for Quality Control in Food Industry: A Case Study of Wheat Grain Cooking Process

K. Srikaeo*

Food Science and Technology Program, Faculty of Food and Agricultural Technology, Pibulsongkram Rajabhat University, Muang, Phitsanulok, Thailand

e-mail: khongsak@psru.ac.th

Abstract

A variety of microscopy techniques have been applied in food industry for quality control purposes. This paper demonstrates the use of a scanning electron microscope (SEM) and a light microscope (LM) in conjunction with image analysis for investigation of starch granules, in order to judge the quality of starch gelatinization in wheat grain cooking process. Both SEM and LM with image analysis are proved to be a useful tool. The present study shows that the swelling and melting of starch granules are influenced by the cooking process. The use of LM with subsequent image analysis provided a simple method for observation of starch gelatinization and quantitation. This study also demonstrates that SEM and LM are useful for the investigation of starch granules in cooked wheat grains without prior starch isolation.

Background

The cooking of wheat grains with steam under pressure is an initial process for some breakfast cereals. This process is important as it develops the grain properties necessary for the development of the product characteristics such as texture, flavor and color - primarily by gelatinization of the starchy grain fractions [1]. Microscopy techniques be used for examination of starch gelatinization. Recently, a variety of microscopy techniques have been applied into food industry for quality control purposes, particularly in cereal products [2]. This study demonstrates the use of scanning electron microscope (SEM) and a light microscope (LM) to observe the gelatinization of intact starches within the whole grain system during the cooking process. Microscopy images were used to judge the quality of starch gelatinization in cooked wheat grains.

Materials and Methods

Mixed varieties of soft wheat grains, 10% protein content, were used. Wheat samples (100 g) were cooked in a steam pressure cooker (45 L volume and 413 kPa maximum pressure). The cooking conditions included cooking at the same temperature (120 °C) for 20, 40, 60, 80, 100 and 120 min, and cooking for the same time (40 min) at 110, 130 and 140 °C.

For the SEM analysis, the cooked wheat samples from various conditions were cut in cross section and then frozen instantly using liquid nitrogen. Frozen samples were dried using a freeze drier (Dynavac Freeze Drier). Dried samples were mounted onto aluminum stubs using metal adhesive glue and then coated with gold (SPI Gold

Sputter Coater) before observed by the SEM (Phillips XL30). SEM images of each sample were taken at 1,000x magnification.

For the LM study, cooked wheat grains after cooling down and equilibration to room temperature were dried in a vacuum oven at 40 °C for about 24 hr. This low temperature drying should limit the effect of heat on the remaining starches. Dried samples were ground using a laboratory mill (LM 3100, Perten Instruments, 0.8 mm sieve). This provided the cooked-wheat flour which was then used for the LM observations. Suspensions of cooked-wheat flour (1g/25mL distilled water) were prepared in the test tube, iodine stained and mixed thoroughly before being analyzed by direct LM (Kyowa Medilux-12) at 40x magnification. Notably that the suspensions were sampled immediately after mixing using a dropper and then smeared on slides before covered with cover glasses. The sampling was conducted with the minimized time to ensure the uniformity of starch in the suspensions. LM images were captured by the digital camera (Pulnix TMC-6) attached with the microscope using the resolution at 640 x 480 pixels for all samples. The images obtained were then analyzed for the number and size of the starch granules (determined from the dark particles in the captured LM images) using Image-Pro Plus Version 1.3.2 (Media Cybernetics U.S.). Notably that this study assumed the darkblue spots found in the LM images to be starch granules. However, they might not be all starches since the samples were cooked wheat flour, other component e.g. protein embedded with starch granules could also be counted.

Results and Discussion

The SEM images of samples cooked at the same temperature (120 °C) for different times are shown in figure 1. In addition, figure 2 represents the SEM images of wheat grains cooked at different temperatures for the same time (40 min).

The SEM provides a clear view of changes of intact starch granules in cooked wheat samples. For the experiment on the same cooking temperature (figure 1), when cooking for a short time e.g. 20 min, the lentil-shaped and circular starch granules of various sizes (both A and B types), protein matrix, and adhesive protein areas attached to starch granules were clearly observed. However, when cooking for a longer period, starch gelatinization increased, resulting in swelling and melting which led to strong deformation of the granules and ultimately the molten granules connected with one another. Other components of the grains such as protein, pentosan and gluten also absorbed water and could be denatured when exposed to heat for a longer period. The combination of these factors resulted in the changes of starch microstructure which were progressively more shapeless or mud-like structure. For the experiment on the same cooking time (figure 2), as expected, samples exposed to higher temperatures e.g. 130-140 °C developed more mud-like structure than those exposed to lower temperatures e.g. 110-120 °C.

SEM observation of starch granules during gelatinization has been well documented but mainly in systems of pure starches with water. This study showed that SEM could be used to observe the starch granules in the whole grain system without the need for starch isolation. Although, the SEM images are not as clear as in isolated or pure starch systems, they provide similar patterns. For qualitative purposes or product quality control in food manufacturing, the results should be acceptable.

Figure 3 shows the LM images of wheat samples cooked at the same temperature (120 °C) for various times (20-120 min). Similar patterns were obtained for the experiment of cooking at the same time (40 min) but different temperatures (110-140 °C), the images are not shown.

It is well known that gelatinized starch granules become bigger in size and granule shape turns to be a honeycomb-like structure. Figure 4 shows the average area sizes of the starch granules, determined from the dark-blue spots and calculated by the image analysis software. It appears that, with the increased cooking time or temperature, the area of starch granules increased as a result from swelling and structural changes of starch granules together with the connection to each other and other components.

LM with iodine staining is a simple and well established technique for the observation of starch granules. This study demonstrated the use of LM and computer-based image analysis for quantitative investigation of starch granules. A cooked-wheat flour system without prior isolation of starches was investigated. Such a simple preparation could be beneficial in practices or for industrial uses as starch isolation is a complicated and time-consuming procedure especially isolation of starch from cereal products.

Conclusion

Both SEM and LM could be used for investigation of starch gelatinization in the whole grain system without the need for prior isolation of starches. These simple methods could be practical for food industries for the quality control of their products, particularly in cereal products in which starch gelatinization is the main processing step. The enhancement of image analysis in conjunction with traditional LM techniques provides a simple method for investigation of starch granules with quantitative results. However, it should be kept in mind that the microscopic methods used in this study are limited for some purposes e.g. for industrial use. The results should be used with great care.

- Caldwell, E.F., Fast, R.B., Levolella, J., Lauhoff, C., Levine, H., Miller, R.C., Slade, L., Strahm, B.S. and Whalen, P.J. Cooking of ready-to-eat breakfast cereals. Cereal Foods World. 2000, 45: 246-252.
- Srikaeo, K., Furst, J.E., Ashton, J.F. and Hosken, R.W. Microstructural changes of starch in cooked wheat grains as affected by cooking temperatures and times. LWT. 2006, 39: 528-533.

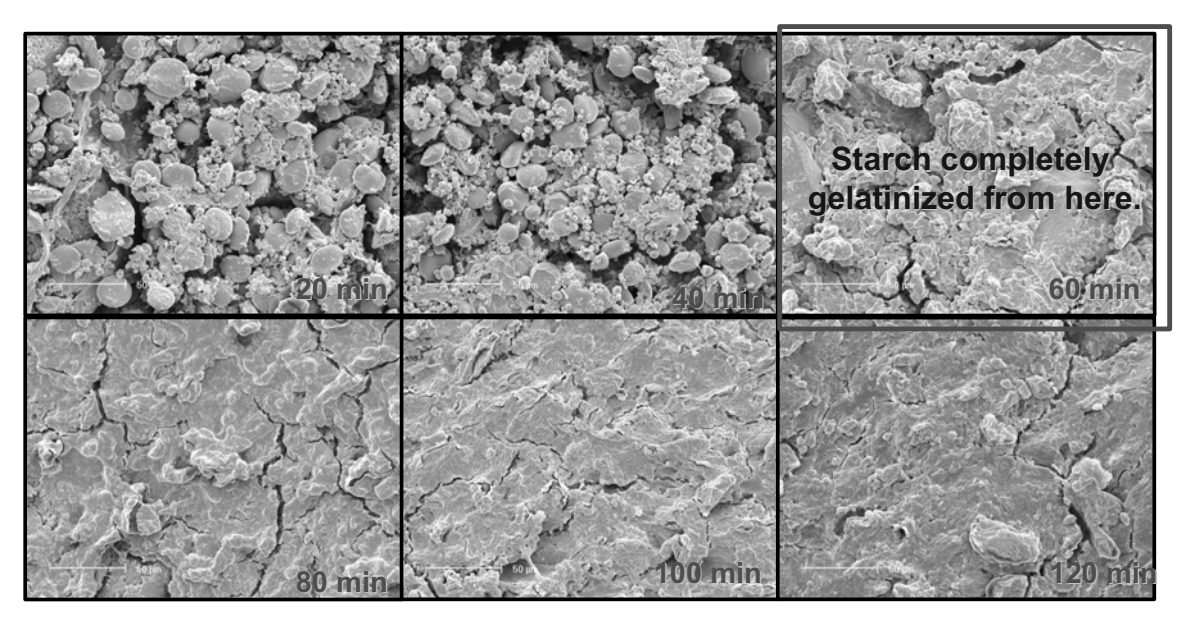


Fig. 1 SEM images of wheat grains cooked at 120 °C for 20, 40, 60, 80, 100 and 120 min

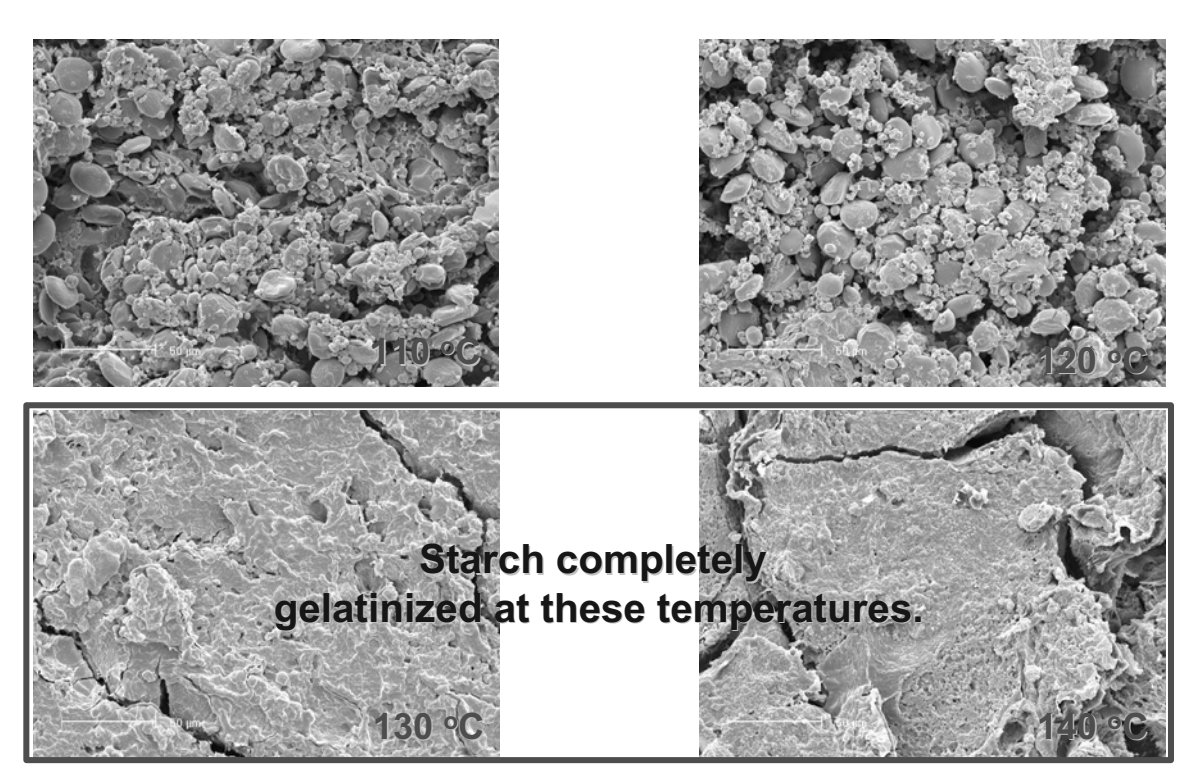


Fig. 2 SEM images of wheat grains cooked at 110 - 140 $^{\rm o}{\rm C}$ for the same time (40 min).

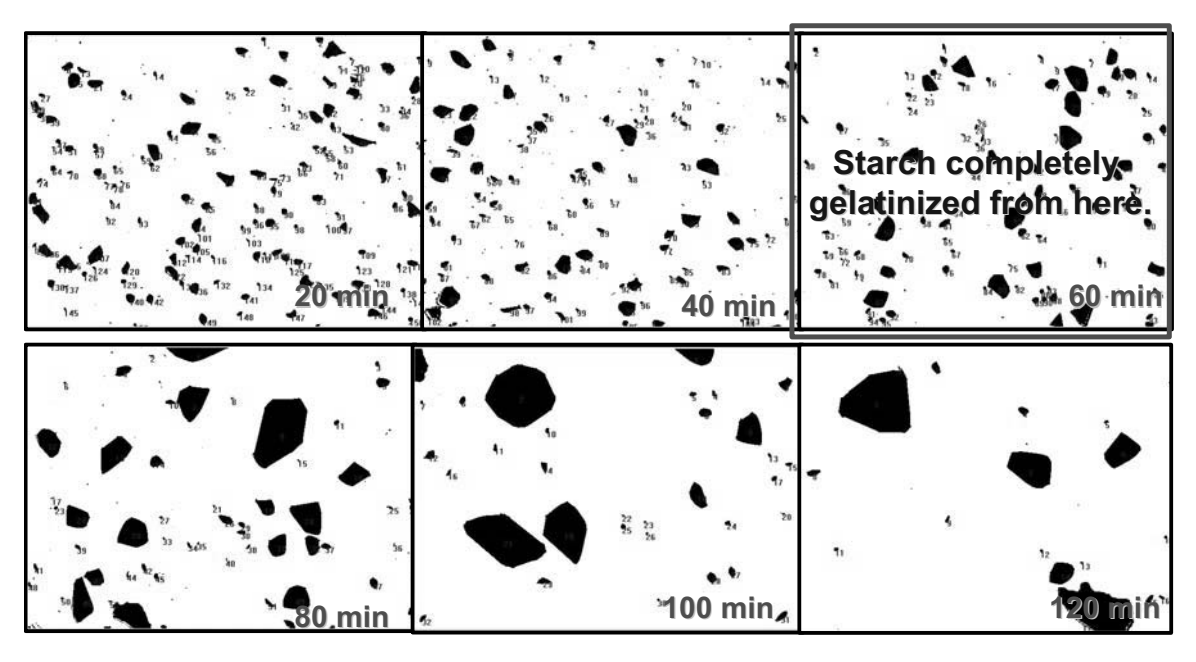


Fig. 3 LM images of wheat grains cooked at 120 °C for 20, 40, 60, 80, 100 and 120 min.

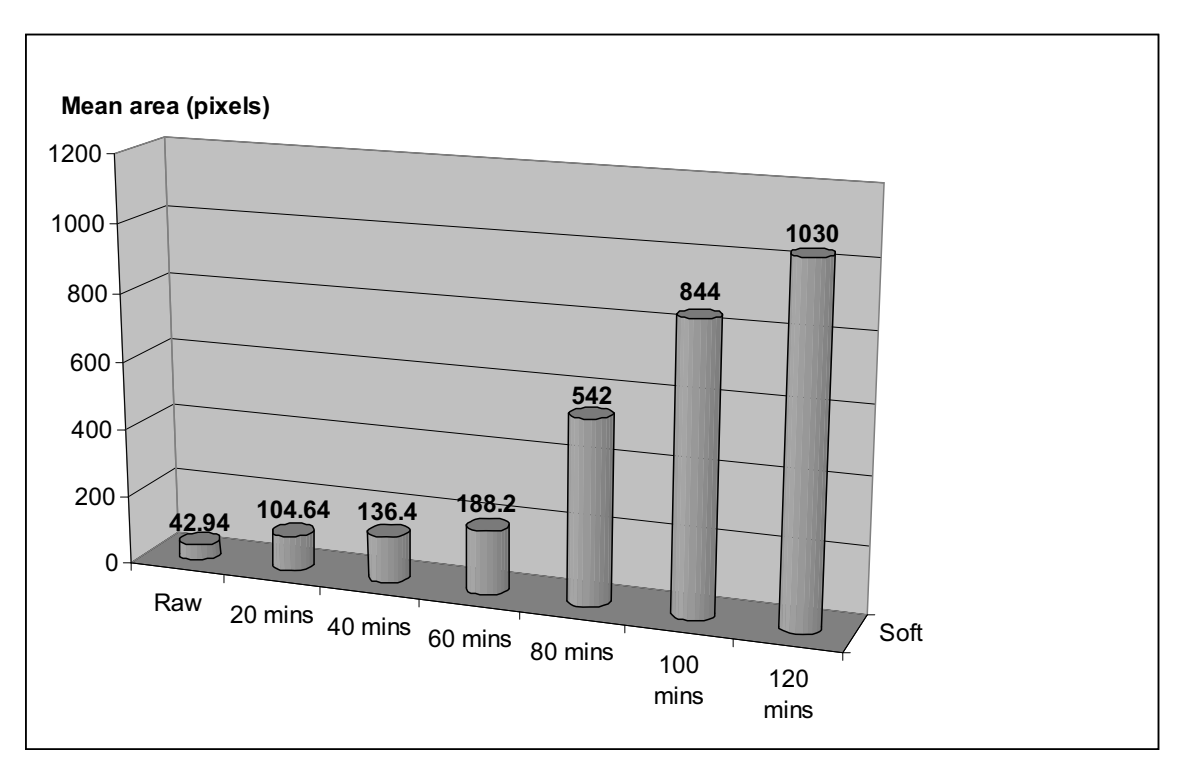


Fig. 4 Average area sizes of starch granules of raw wheat and wheat grains cooked at 120 °C for 20, 40, 60, 80, 100 and 120 min (calculated by image analysis software)

Neuronal Sprouting Following Spared Nerve Injury in Rats Studied by Cholera Toxin B Subunit Immunoreactivity

Supin Chompoopong^{1*}, Kanyarat Bamrungsuk¹, Kanokwan Tilokskulchai² and Tulaporn Wongtawatchai¹ Department of Anatomy and ²Department of Physiology, Faculty of Medicine, Siriraj Hospital, Mahidol University, Bangkok 10700, Thailand

e-mail: siscm@mahidol.ac.th

Abstract

Objective: The aim of this study was to determine whether spared nerve injury (SNI) alters the laminar terminations of A-beta fibers in rat spinal dorsal horn.

Materials and Methods: Twenty six adult male rats weighing 250-300 grams were randomly assigned into two groups (n=13 each). One group underwent SNI. Another group was subjected to sham operation. The SNI was performed on the right hind limb by transected the tibial and common peroneal nerves leaving the sural nerve intact. Three days before sacrifice of rat, the sciatic nerve proximal to injury site was injected with cholera toxin B subunit (CTB) that effectively labels both peripheral and central A-beta axons. The effect of SNI was evaluated by analyzing the extent of CTB (CTBir) and substance P (SPir) immunoreactivities with confocal microscopy in L4-L6 dorsal root ganglia (DRG) and spinal dorsal horn at five weeks after surgery. The intensity of SPir were analysed as the percentage changes in mean grey level by using ImageTool program 3.0 and compared between SNI and sham groups.

Results: Following SNI, SPir in DRG and spinal dorsal horn were significantly increased with respect to sham, p < 0.001. On the basis of the use of CTB as a selective tracer for A-beta fibers, neuronal sprouting was studied in the spinal dorsal horn. In sham operation group, CTBir was present in laminae III and IV. In SNI group, CTBir distributed in laminae III and IV and dispersed into lamina II, a region that normally receives only C-fiber input. In addition, CTBir was shown co-localization with SPir in medium- and large-size DRG neurons.

Conclusions: The present results showed that the increase of SPir in DRG and spinal dorsal horn may due to elevated NGF levels from Schwann and other endoneurial cells involved in Wallerian degeneration following SNI. It was also shown that the central terminals of cutaneous myelinated afferents, including the large A-beta fibers from the medium- and large- DRG neurons, sprout into lamina II of spinal dorsal horn. This lamina that normally receives nociceptive input was activated by tactile stimuli. It was suggested that this structural reorganization in the central nervous system may contribute to mechanical allodynia associated with neuropathic pain. Therefore, this phenomenon may also help to explain the pain mediated by A-fiber following peripheral nerve injury in patients.

Background

Neuropathic pain represents a major clinical problem because in contrast to nociceptive pain, it is largely resistant to the methods that are presently available for pain relief. There is the evidence that this type of pain is mediated by large myelinated (A-beta) afferents (1, 2). Because stimulation of these afferents does not normally produce pain, it is believed that changes within the CNS must be involved (3).

It is clear that in DRG, most large and medium diameter neurons possess large myelinated axons (A-beta fibers). Small neurons exhibit axons with either no myelination (C-fibers) or thinly myelinated axons (A-delta fibers). The central projections of DRG neurons convey functionally distinct information to the spinal dorsal horn in a laminar-specific manner. Small diameter slowly conducting DRG neurons with C-fibers and A-delta fibers are principally nociceptive with central projections to laminae I and II of the spinal cord

dorsal horn (4). Large diameter neurons with Abeta fibers have central terminations in laminae III–VI (5).

Following peripheral nerve injury, the neuronal sprouting can be defined as the growth of intact axons into neighboring denervated territory. There was the evidence that the nerve lesion such as partial denervation results in the peripheral sprouting of both small (6) and large (7) intact primary sensory axons. The central sprouting of uninjured primary sensory neurons in the spinal dorsal horn which denervated by transection of adjacent dorsal roots was first suggested by Liu and Chambers (1958) (8). Since then, the notion that denervation alone is sufficient to induce sprouting of the central axons of uninjured primary sensory neurons has been both supported (9, 10) and disputed (11, 12).

To date, it is still controversial what are responsible for the central sprouting of those

primary afferents. Recently, the cholera toxin B subunit (CTB) that effectively labels both peripheral and central A-beta axons has been used to study in sciatic nerve section or crush models. The mechanism of A-fiber sprouting has been thought to involve this injury (13). Since there is evidence indicating that SNI rat model closely mimic many features of clinical neuropathic pain (14). It has been proposed as a useful tool for identifying the development of mechanisms involved in the production of neuropathic pain and as an additional model for screening the efficacy of new treatments. Therefore, in this study, the CTB was injected into the injured nerve to determine whether SNI alters the laminar terminations of Abeta fibers in rat spinal dorsal horn.

Materials and Methods

All experiments were performed on adult Sprague Dawley male rats (average weight 250-300g). During the experimentation period, the rats were housed in individual cages with free access to food and water and at a controlled room temperature (22±2°C) with a twelve-h light/dark cycle. All procedures complied with the ethical guidelines for pain experimentation on awake animals (15) and were approved by the Ethical Committee on Animal Experiments of Mahidol University. This study was based on results obtained from 26 rats randomly distributed into two groups (n= 13 each). One group underwent spared nerve injury (SNI) and another group was subjected to sham operation (Sham)

Nerve Injury Surgical Procedure

Peripheral neurophathy following Decosterd and Woolf (14) model was induced in the SNI group. Briefly, under pentobarbital sodium anesthesia (40 mg/kg, i.p.), the skin on the lateral surface of the right thigh was incised and a section made directly through the biceps femoris muscle exposing the sciatic nerve and its three terminal branches: the sural, common peroneal and tibial nerves. The common peroneal and the tibial nerves were transected close to the position that nerves enter the muscles and leaving the sural branch intact. Great care was taken to avoid any contact with or stretching of the intact sural nerve. Muscle and skin were closed with 3-0 silk in two layers. The wound was then covered with topical antibiotics. In sham controls the right sciatic nerve and its branches were identically exposed without any lesion. In both groups, the contralateral thigh remained unoperated.

Tracing of A-beta Projections to the Dorsal Horn

Cholera toxin B-subunit (CTB) have been used to map the central rojections of cutaneous

myelinated primary afferents in the spinal dorsal horn of rats (16). Three days before sacrifice, all animals were anesthetized with sodium pentobarbital (40 mg/kg i.p.). Right sciatic nerves were reexposed and injected proximal to the injury site with small volumes (2.5–3 microlitre) of CTB (sigma, 1% dissolved in distilled water) by using Hamilton microsyringes.

Tissue Preparation and Immunofluorescent Staining

SP and CTB were determined in SNI and Sham rats by immunofluorescent histochemistry. Five weeks after surgery, all animals were anesthetized with sodium pentobarbital (50 mg/kg i.p.) and perfused transcardially with 100 ml saline followed by 500 ml ice cold 4% paraformaldehyde in 0.1 M phosphate buffer (PB) at pH 7.4. The L4-L6 spinal cord and DRG were removed, placed in the same fixative overnight at 4°C, and transferred to 30% sucrose (w/v) in 0.1 M PB for three days for cryoprotection. Serial coronal section of spinal cord and DRG at a thickness of 40 µm and 15 µm, respectively were prepared in a Leitz cryostat and mounted on gelatin coated slides. The sections were treated with phosphate-buffered saline (PBS, 0.1M, pH 7.2) containing 1% BSA and 0.05% Tween-20 for 30 min at room temperature. The primary antiserum, goat polyclonal antiserum directed against SP (1:50; Santa Biotechnology) and rabbit anti-cholera toxin B (1:1000, Sigma) in 0.1M PBS containing 1% BSA and 0.05% Tween-2 was used for the incubation with the sections for overnight at 4°C. The sections were washed in 0.1 M PBS and then incubated in the secondary antiserum, FITC-conjugated donkey anti-goat IgG (1:500; Santa Crus Biotechnology) and 1.5% Texas Red anti-rabbit IgG (Vector laboratories) for 3 h at room temperature. After several rinses in 0.1 M PBS, sections were cover slipped with Vectashield (Vector) and observed under a Carl Zeiss Confocal Laser Scanning microscope.

Image Analysis

Image analysis of SPir staining was performed on five nonadjacent sections of DRG and spinal dorsal horn from each animal. To determine changes in SPir in the SNI and sham groups, the density of SPir was quantified using a computerbased image analysis system (the free UTHSCSA ImageTool program, 3.00) (17). While viewing the monitor, upper and lower thresholds of grey level density were set such that only specific SP product immunoreaction was accurately discriminated from the background in the outlined lamina I-IV of the dorsal horn and DRG. The pixel-by-pixel was read by the computer (18).

Subsequently, the total area of discriminated pixels was divided by the area of the outlined dorsal horn. The mean grey level values from the five random sections were averaged for each animal and expressed as mean \pm S.E.M. Since the staining on the contralateral side was equivalent to that seen in unoperated animals, the percentage change in DRG and spinal dorsal horn was calculated as ipsilateral/contralateral X 100. The changes in SPir staining in DRG and spinal dorsal horn were compared by using independent sample t-test. Differences were considered significant if p < 0.001.

Results

General Observations

The majority of rats subjected to SNI displayed evident signs of neuropathy in the hind paw ipsilateral to the nerve injury. This was clearly present 24 h after the surgery. These signs included abnormal position of the paw (inversion) and signs of spontaneous pain such as shaking and licking. No autotomy or body weight loss was observed. It is worth noting here that rats without evident signs of neuropathy were not included in this study.

SP and CTB Immunofluorescent Localization

SP and CTB were located in DRG and spinal dorsal horn of rats by immuno-fluorescent staining. As shown in table 1, the percentage changes of mean grey level of SPir were analyzed and compared between SNI and sham groups. Following five weeks surgery, SNI rats demonstrated a significant increase of SPir in DRG and spinal dorsal horn on the operated side, as compared with the same side in sham, p < 0.001.

Using retrograde labelling with CTB to identify A-beta fibers, CTBir was shown co-localization with SPir in medium- (30-50 micrometer) and large-size (> 50 micrometer) DRG neurons five weeks after SNI (figure 1A). But only SPir was shown in small-size (< 30 micrometer) DRG neuron. In addition, neuronal sprouting was studied in the spinal dorsal horn. In sham operation group, CTBir was present in laminae III and IV (data not shown). In figure 1B, it was shown that SNI results in the sprouting of numerous CTBir- labeled large myelinated sensory axons. These A-beta fibers sprout from their normal termination site in laminae III and IV into lamina II, a region that normally receives only C-fiber input.

Discussion

As proposed previously by Decosterd and Woolf (2000), SNI is well-established methods that are available to measure thermal and mechanical sensitivity in awake behaving rats for studying the neuropathic pain. The purpose of this investigation was to determine whether SNI alters the laminar

terminations of A-beta fibers in rat spinal dorsal horn. In this study, it was demonstrated that the transected tibial and common peroneal nerves leaving the sural nerve intact in this SNI model could result in a significant increase of SPir in DRG and spinal dorsal horn five weeks after injury. In contrast, the previous report was shown that complete sciatic nerve injury reduces SP expression in primary sensory neurons of the L4 and L5 DRG and spinal dorsal horn, due to loss of target-derived nerve growth factor (NGF) (19-21). But the present study in line with the report by Noguchi and Kawai (22) that SPir was increased in the gracile nucleus and large myelinated fibers in the dorsal root two weeks after unilateral sciatic nerve transection. In addition, Ma and Bisby (23) reported that partial sciatic nerve injury elevated SP levels in spared DRG neurons. They also suggested that the elevated of SP might be involved in the development of neuropathic pain, which commonly follows partial nerve injury. One possible explanation is that the increase of SPir in the present study may be the result of the activation of spared sural nerve and it's spared DRG neurons after exposing to elevated NGF levels. Moreover, there has been proposed interaction between injured and intact nerve fibers that the degeneration of axons is likely to alter Schwann cells supporting intact axons (24). Therefore, the elevated of NGF may be released from Schwann and other endoneurial cells involved in Wallerian degeneration of injured tibial and common peroneal nerves (25). SP is believed to be a neuromediator of nociception in the spinal dorsal horn. SP prescursor is synthesized in the small DRG neurons and transported via axoplasmic transport to the nerve terminal where it is stored and released as SP. This increase in SP may be the result of increased electrical activity due to activation of small C-fibers (26). Although lowthreshold myelinated (A-beta) afferent axons do not normally synthesize neuropeptides, it is well established that they can upregulate neuropeptideY (NPY) after peripheral axotomy (27). The present results also demonstrated the co-localization of CTBir and SPir in medium- and large-size DRG neurons that possess large myelinated axons (Abeta fibers). Therefore, both C- and A-beta fibers in intact sural nerve may be involved in the increase of SP in the spinal dorsal horn after SNI.

On the basis of the use of CTB as a selective tracer for A-beta fibers, neuronal sprouting was shown in the spinal dorsal horn. The present results demonstrated that following SNI, large myelinated (A-beta) primary afferent axons terminate in the spinal dorsal horn, occupying an area that extends from laminae III and IV up to lamina II. There was the sprouting of these A-beta fibers into the spinal territory (lamina II) where postsynaptic targets usually receive only small (C-fiber) afferent fibers.

This study agreed with the previous reports that the sprouting depends on the type and location of axonal injury (3, 13). It was proposed that the sprouting of intact A-fibers may be induced by two phenomena. The first is the injury to those sensory C-fibers that terminate in lamina II and the presence of vacant synaptic sites within the superficial dorsal horn as a consequence of transganglionic degeneration of C-fibers (28, 29). The second is the peripheral axonal injury and the induction of a regenerative capacity in the injured neurons (30), presumably because of upregulation of developmentally regulated growth-related proteins such as GAP-43 (31). GAP-43 is transported to central terminals of injured sensory neurons in lamina II (32). Therefore, peripheral nerve injury may induce both the molecular machinery necessary for growth and provide a denervated area (space) in lamina II (substantia gelatinosa) for the sprouts of A-beta fibers to grow into. This type of growth has been termed conditioned collateral sprouting (3). In this study, it could not conclude that SNI induces the sprouting of injured or intact A-beta fibers because the CTB injection was performed in the sciatic nerve proximal to injury site. Therefore, it's better to inject CTB into the intact sural nerve. However, based on these phenomena, it was also suggested that the sprouting may contribute to neuropathic tactile allodynia (touch-evoked pain) after SNI. In addition, finding of A-beta sprouting in SNI model also supports evidence for using as a direct way of investigating changes in both injured primary sensory neurons and in neighboring intact sensory neurons in the same level (L4-L6) of dorsal root ganglion. It could explain the contribution to the pathophysiology of neuropathic pain. It permits behavioral testing of the noninjured (sural nerve) skin territories adjacent to the denervated (tibial and common peroneal nerves) areas.

Conclusion

The present results indicate that, SNI increased SPir in the DRG and spinal dorsal horn at five weeks after injury. It may due to elevated NGF levels from Schwann and other endoneurial cells involved in Wallerian degeneration. It was also shown that following SNI, the central terminals of cutaneous myelinated afferents, including the large A-beta fibers from the medium- and large- DRG neurons, sprout into lamina II of spinal dorsal horn. This lamina that normally receives nociceptive input was activated by tactile stimuli. It was suggested that this structural reorganization in the central nervous system may contribute to mechanical allodynia associated with neuropathic pain. Therefore, this phenomenon may provide evidence that SNI might be a suitable neuropathic model that may help to explain the pain mediated

by A-fiber following peripheral nerve injury in patients.

Acknowledgment

We would like to express our sincere thanks to Sansanee Noisakorn, PhD for her valuable advice in Confocal microscope at Medical Biotechnology Unit, Siriraj Hospital.

Table 1 The percentage change of mean grey level of SPir expressed as mean \pm SEM from 5 random sections of L4-L6 DRG and spinal dorsal horn per rat was measured by ImageTool analysis program 3.0. Comparison between sham and SNI group was demonstrated. (*Statistical significant at p < 0.001)

Sections	SI	Pir	<i>p</i> -value
	Sham	SNI	P
DRG	100.0±5.5 (10±2.1)	282.0±6.0* (28.2±8.1)	0.000
Spinal dorsal horn	100.0±5.6 (61.4±0.2)	224.8±9.0* (138±2.3)	0.000

- 1. Campbell, J.N., Raja, S.N., Meyer, R.A. and Mackinnon, S.E. Myelinated afferents signal the hyperalgesia associated with nerve injury. *Pain* 1988, 32: 89-94.
- Koltzenburg, M., Torebjork, H.E. and Wahren, L.K. Nociceptor modulated central sensitization causes mechanical hyperalgesia in acute chemogenic and chronic neuropathic pain. *Brain* 1994, 117 (Pt 3): 579-591.
- 3. Woolf, C.J., Shortland, P., Reynolds, M., Ridings, J., Doubell, T. and Coggeshall, R.E. Reorganization of central terminals of myelinated primary afferents in the rat dorsal horn following peripheral axotomy. *J Comp Neurol* 1995, 360: 121-134.
- 4. Leem, J.W., Willis, W.D., Weller, S.C. and Chung, J.M. Differential activation and classification of cutaneous afferents in the rat. *J Neurophysiol* 1993, 70: 2411-2424.
- 5. Grant, G. Projection patterns of primary sensory neurons studied by transganglionic methods: somatotopy and target-related organization. *Brain Res Bull* 1993, 30: 199-208.
- Diamond, J., Holmes, M. and Coughlin, M. Endogenous NGF and nerve impulses regulate the collateral sprouting of sensory axons in the skin of the adult rat. *J Neurosci* 1992, 12: 1454-1466.
- 7. Doubleday, B. and Robinson, P.P. Nerve growth factor depletion reduces collateral sprouting of cutaneous mechanoreceptive and tooth-pulp axons in ferrets. *J Physiol* 1994, 481 (Pt 3): 709-718.

- 8. Liu, C.N. and Chambers, W.W. Intraspinal sprouting of dorsal root axons; development of new collaterals and preterminals following partial denervation of the spinal cord in the cat. *AMA Arch Neurol Psychiatry* 1958, 79: 46-61.
- 9. LaMotte, C.C. and Kapadia, S.E. Deafferentation-induced terminal field expansion of myelinated saphenous afferents in the adult rat dorsal horn and the nucleus gracilis following pronase injection of the sciatic nerve. *J Comp Neurol* 1993, 330: 83-94.
- McNeill, D.L., Carlton, S.M., Coggeshall, R.E. and Hulsebosch, C.E. Denervation-induced intraspinal synaptogenesis of calcitonin generelated peptide containing primary afferent terminals. *J Comp Neurol* 1990, 296: 263-268.
- 11. McMahon, S.B., Lewin, G. and Bloom, S.R. The consequences of long-term topical capsaicin application in the rat. *Pain* 1991, 44: 301-310.
- 12. Pubols, L.M. and Bowen, D.C. Lack of central sprouting of primary afferent fibers after ricin deafferentation. *J Comp Neurol* 1988, 275: 282-287.
- 13. Woolf, C.J., Shortland, P. and Coggeshall, R.E. Peripheral nerve injury triggers central sprouting of myelinated afferents. *Nature* 1992, 355: 75-78.
- Decosterd, I. and Woolf, C.J. Spared nerve injury: an animal model of persistent peripheral neuropathic pain. *Pain* 2000, 87: 149-158.
- 15. Zimmermann, M. Ethical guidelines for investigations of experimental pain in conscious animals. *Pain* 1983, 16: 109-110.
- Woodbury, C.J., Ritter, A.M. and Koerber, H.R. On the problem of lamination in the superficial dorsal horn of mammals: a reappraisal of the substantia gelatinosa in postnatal life. *J Comp Neurol* 2000, 417: 88-102.
- 17. Wilcox, C.D., Dove, S.B., McDavid, W.D. and Greer, D.B. UTHSCSA ImageTool 3.00 ed. San Antonio, Texas: The University of Texas Health Science Center 2002.
- 18. Imbe, H., Okamoto, K., Kadoya, T., Horie, H. and Senba, E. Galectin-1 is involved in the potentiation of neuropathic pain in the dorsal horn. *Brain Res* 2003, 993: 72-83.
- 19. Barbut, D., Polak, J.M. and Wall, P.D. Substance P in spinal cord dorsal horn decreases following peripheral nerve injury. *Brain Res* 1981, 205: 289-298.
- Hokfelt, T., Zhang, X. and Wiesenfeld-Hallin,
 Z. Messenger plasticity in primary sensory neurons following axotomy and its functional implications. *Trends Neurosci* 1994, 17: 22-30.
- 21. Jessell, T., Tsunoo, A., Kanazawa, I. and Otsuka, M. Substance P: depletion in the dorsal horn of rat spinal cord after section of the peripheral processes of primary sensory neurons. *Brain Res* 1979, 168: 247-259.

- Noguchi, K., Kawai, Y., Fukuoka, T., Senba, E. and Miki, K. Substance P induced by peripheral nerve injury in primary afferent sensory neurons and its effect on dorsal column nucleus neurons. *Journal of Neuroscience* 1995, 15: 7633-7643.
- Ma, W. and Bisby, M.A. Increase of preprotachykinin mRNA and substance P immunoreactivity in spared dorsal root ganglion neurons following partial sciatic nerve injury. Eur J Neurosci 1998, 10: 2388-2309
- Murinson, B.B., Hoffman, P.N., Banihashemi, M.R., Meyer, R.A. and Griffin, J.W. C-fiber (Remak) bundles contain both isolectin B4binding and calcitonin gene-related peptidepositive axons. *J Comp Neurol* 2005, 484: 392-402
- 25. Heumann, R., Lindholm, D., Bandtlow, C., Meyer, M., Radeke, M.J., Misko, T.P., Shooter, E. and Thoenen, H. Differential regulation of mRNA encoding nerve growth factor and its receptor in rat sciatic nerve during development, degeneration, and regeneration: role of macrophages. *Proc Natl Acad Sci U S A* 1987, 84: 8735-8739.
- Robert, M.K., Barry, D.G. and Margaret, L.K. Regulatory mechanisms for subtance P in the dorsal horn during a nociceptive stimulus: Axoplasmic transport vs electrical activity. *Brain Research* 1986, 385: 282-290.
- 27. Zhang, X., Meister, B., Elde, R., Verge, V.M. and Hokfelt, T. Large calibre primary afferent neurons projecting to the gracile nucleus express neuropeptide Y after sciatic nerve lesions: an immunohistochemical and in situ hybridization study in rats. *Eur J Neurosci* 1993, 5: 1510-1519.
- Himes, B.T. and Tessler, A. Death of some dorsal root ganglion neurons and plasticity of others following sciatic nerve section in adult and neonatal rats. *J Comp Neurol* 1989, 284: 215-230.
- Kapadia, S.E. and LaMotte, C.C. Deafferentation-induced alterations in the rat dorsal horn: I. Comparison of peripheral nerve injury vs. rhizotomy effects on presynaptic, postsynaptic, and glial processes. *J Comp Neurol* 1987, 266: 183-197.
- 30. Skene, J.H. Axonal growth-associated proteins. *Annu Rev Neurosci* 1989, 12: 127-156.
- 31. Chong, M.S., Fitzgerald, M., Winter, J., Hu-Tsai, M., Emson, P.C., Wiese, U. and Woolf, C.J. GAP-43 mRNA in Rat Spinal Cord and Dorsal Root Ganglia Neurons: Developmental Changes and Re-expression Following Peripheral Nerve Injury. *Eur J Neurosci* 1992, 4: 883-895.
- 32. Woolf, C.J. and King, A.E. Dynamic alterations in the cutaneous mechanoreceptive fields of dorsal horn neurons in the rat spinal cord. *J Neurosci* 1990, 10: 2717-2726.

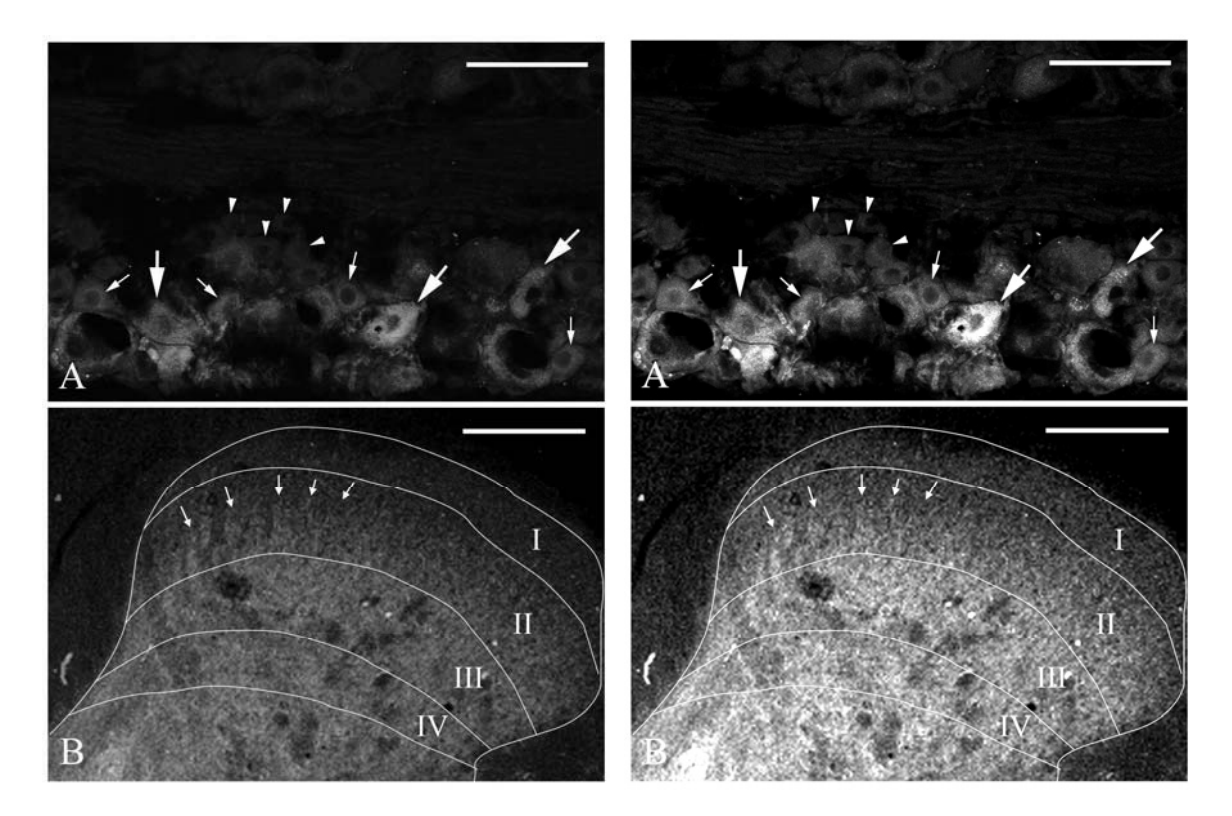


Fig. 1 The confocal merge - image of SPir (green) and CTBir (red) in the rat DRG (fig. 1A) and spinal dorsal horn (fig. 1B) at five weeks after SNI. Co-localization of SP and CTB were demonstrated in medium- (small arrows) to large-sized (large arrows) DRG neurons but not in small- (arrow head) DRG neurons (fig. 1A). Neuronal sprouting was studied in the spinal dorsal horn. In sham operation group, CTBir was present in laminae III and IV (data not shown). In fig.1B, it was shown that SNI results in the sprouting of numerous CTBir- labeled large myelinated sensory axons into laminae II (small arrows), a region that normally receives only C-fiber input. Scale bar: 100 micrometer.

Light and SEM Studies on Leaf Litter Fungi

Leka Manoch¹*, Onuma Jeamjitt¹, Amnat Eamvijarn¹, Tida Dethoup¹, Jitra Kokaew¹, Yupadee Paopun², Pachongchit Poochinya² and Patcharee Umrung²

Department of Plant Pathology, Faculty of Agriculture, Kasetsart University, Bangkok 10900, Thailand

e-mail: agrlkm@ku.ac.th

Abstract

Diversity of leaf litter fungi from various fallen leaves was carried out. Thirteen samples of nine different plants were collected from various locations. The moist chamber, direct isolation and dilution plate methods were used. Fungi were cultivated on 3% malt extract agar and half strength potato dextrose agar. Identification was based on morphological study examined under stereo, light and scanning electron microscopes (Jeol: JSM 5600 LV).

Twenty-nine species of leaf litter were found, including Arthrinium phaeospermum, Bipolaris maydis, Beltrania rhombica, Chaetospermum camelliae, Cladosporium cladosporioides, Colletotrichum capsici, Corynespora sp., Curvularia eragrostidis, Cylindrocladium sp., Ellisiopsis gallesiae, Fusarium semitectum, Gilmaniella humicola, Gyrothrix sp. Helicomyces sp., Lophodermium sp., Memnoniella echinata, Myrothecium verrucaria, Nigrospora sphaerica, Periconia digitata, Pestalotiopsis guepinii, Pithomyces sp., Pseudorobillarda sp., Stachybotrys nephrospora, S. kampalensis, Tetraploa aristata, Torula herbarum, Volutella concentrica and Wiesneriomyces javanicus.

Background

The study on diversity of leaf litter fungi from various host plants were reported (Bills and Polishook 1994, Saravanan, 2004; Tokumasu *et al.*, 1997). Some fungi are common on leaf litter in many studies, while many new fungal taxa have been described from decaying leaves and dead wood (Hughes, 1989). Several species of microfungi can produce bioactive compounds very useful in phamaceutical and agriculture.

Recent contributions of leaf litter fungi in Thailand have been carried out. Manoch al. (2006 a) reported diversity of leaf litter fungi from 7 plants collected from different locations. found 26 genera 31 species of Hyphomycetes, 8 species of Coelomycetes and 5 species of Ascomycetes. Leaf litter fungi have been used as biological control agent against plant pathogenic fungi in vitro. Manoch et al. (2006 a) found that two leaf litter fungi, Myrothecium verrucaria and Ciliochorella sp. could inhibit growth of Alternaria alternata, Colletotrichum capsici, Curvularia lunata and oxysporum in vitro. In addition, morphological study of 42 genera 48 species leaf litter fungi was reported using light microscope (Manoch et al., 2006 b).

Six new species of dematiaceous hyphomycetes from dead wood and bark in New Zealand were illustrated and described (Hughes, 1989).

Microfungi are very important in producing secondary metabolites very useful in agriculture, medicine and pharmaceutical. Saparrat *et al.* (2002) reported laccase activity in *Tetraploa aristata* (

Hyphomycetes) isolated from crude oil-polluted organic matter in Santiago river, Buenose Aires, Aegentina. Namata *et al.* (1997) reported pericosines A, B and macrosphelides from *Periconia byssoides* isolated from seahare (*Aplysia kurodai*). This compound proved to be antitumour to the patient, Kim *et al.* (2004) recorded *Periconia* sp. as a source of bioactive compound, periconisin A, B which is bacteria inhibitor.

In Thailand, Rukachisirikul *et al.*, 2005 found that *Beltrania rhombica* on leaf litter from Tone Nga-Chang water fall, Songkha, produced secondary metabolites which inhibited *Staphylococcus aureus* and *Candida albica*. It is thus very interesting to investigate leaf litter fungi in this tropical region.

The purposes of this study were: 1) to study diversity of leaf litter fungi 2) to isolate and identify leaf litter fungi using morphological features.

Materials and Methods

Thirteen samples of leaf litter were collected from different locations (Table 1). For isolation techniques, the moist chamber, direct isolation, dilution plate methods were used. Fungi were cultivated on 3% malt extract agar and half strength potato dextrose agar. Identification was based on morphological study examined under stereo (Olympus SZ-PZ), light (Olympus BH) and

² Scientific Equipment Center, Kasetsart University Research and Development Institute (KURDI), Bangkok 10900, Thailand

scanning electron microscopes (Manoch et al., 2006 a).

For SEM study, several pieces of decaying leaf tissue with fungal spores on the surface were dissected (5x5 mm²). They were prefixed with 25% glutaraldehyde in 0.1 M potassium phosphate buffer, pH 7.2 for overnight in a refrigerator. They were postfixed with 1% osmium tetroxide in distill water for 2 hours at room temperature, then dehydrated with a series of ethyl alcohol at 10%, 30%, 50% and 100% followed by critical point drying method using liquid carbon dioxide (Hitachi model HCP-2). The treated plant samples with fungal spores were placed on aluminum stub using carbon tape. They were coated with gold and examined under SEM (Jeol: JSM 5600 LV) operating at 10 kV (Paopun et al., 2006).

The preparation for SEM study for resistant or hard-walled spore, small pieces (5x5 mm²) of agar blocks containing mycelium and fungal spores from the culture media were put in an electric dessicator for overnight. They were placed on aluminium stub using carbon tape, coated with gold and examined under SEM (Manoch *et al.*, 2007).

Results and Discussion

Twenty nine genera of microfungi from thirteen samples of nine different fallen leaves namely bamboo, jack fruit, lan thom , banana, Kaffir lime (ma-krut), star gooseberry , Pra du, rose apple, Java plum (wha) were reported (Table 2).

Most species of leaf litter fungi are similar to the previous report (Manoch *et al.*, 2006 a, b). Four new species are recorded, including *Ellisiopsis gallesiae*, *Tetraploa aristata* (figures 5, 6), *Helicomyces* sp. (figure 1) and *Lophodermium* sp. isolated from jack fruit leaf, bamboo leaf and unidentified plant respectively.

Tetraploa aristata was isolated from bamboo leaf sheath, Saraburi province (figures 5-6). It is the first record for Thailand. Saparrat et al. (2002) reported laccase activity in Tetraploa aristata (Hyphomycetes) isolated from crude oil-polluted organic matter in Santiago river (Buenose Aires province, Aegentina). Laccases have been used for transforming and polymerizing or degrading different aromatic pollutants causing environmental damage. Laccases catalyze the direct oxidation of aromatic amines, a wide number of phenolic compounds, including lignin phenolic unit, melanin precursors, chlorophenols, anthraquinone dyes and some polycyclic aromatic hydrocarbon (PHA) such as anthracene.

Wiesneriomyces javanicus was isolated from babana leaf, Saraburi province (figures 2-4). Ellis (1971) reported *W. javanicus* on rotten leaves and twigs; Java. This species is widely distributed in the tropics.

Rukachisirikul *et al.*, 2005 found that the isolate of *Beltrania rhombica*_ on leaf litter from Tone

Nga-Chang water fall, Songkha, southern Thailand could produce new active compound sesquiterpenes, such as beta-eudesmol, pterocarpol, longilobol chrysanthemol, and 5 beta hydroxy-beta-eudesmol that could inhibit *Staphylococcus aureus* and *Candida albica*.

Arthrichitin from *Arthrinium phaeospermum* could decompose chitin, which is the component of hypha and insect. As a result this compound can be developed to fungicide and insecticide (Vijayakumar *et al.*, 1996).

Saravanan (2004) studied fungus diversity on *Neolitsea scrobiculata* (Lauraceae) leaf litter in India. A total of 199 genera and 360 species of microfungi were reported comprising 17 undescribed taxa which include 4 new genera and 13 new species.

Conclusion

Twenty nine genera of leaf litter fungi were found on 9 different host plants. Some species are common leaf litter fungi, whereas 4 genera are new records for Thailand including *Ellisiopsis gallesiae, Helicomyces* sp., *Lophodermium* sp., *Tetraploa aristata*..

Acknowledgment

The authors acknowledge the support from Kasetsart University Research Development Institute for the project "Diversity of microfungi from soil, leaf litter and their applications"

- Bills, G.F. and J.D. Polishook. 1994. Abundance and diversity of microfungi in leaf litter of a lowland rain forest in Costa Rica. Mycologia 86: 187-198.
- 2. Ellis, M.B. 1971. Dematiaceous Hyphomycetes. Commonwealth Mycological Institute,
 - Kew, Surrey, England. 608 p.
- 3. Ellis, M.B. 1976. More Dematiaceous Hyphomycetes. Commonwealth Mycological Institute, Kew, Surrey. 507 p.
- 4. Hughes, S.J. 1989. New Zealand fungi 33. Some new species and new record of dematiaceous hyphomycetes. New Zealand Journal of Botany. 27: 449-459.
- Kim, S., D. Shin, T. Lee and K. Oh. 2004. Periconicins, two new fusicoccane diterpenes produced by an endophytioc fungus *Periconia* sp. with antibacterial activity. J. Nat. Prod. 37: 448-450.
- Manoch, L., J. Kokaew, O. Jeamjitt and T. Dethoup. 2006 a. Leaf litter fungi and studies on antagonistic effect against plant pathogenic fungi *in vitro*. pp. 771-780. *In* The Proceedings of 44th Kasetsart University Annual

- Conference, Subject: plants. Kasetsart University, Bangkok. 30 January 2 February 2006.
- Manoch, L., O. Jeamjitt J. Kokaew and T. Dethoup. 2006 b. Morphological study of leaf litter fungi. Journal of Microscopy Society of Thailand 20(1): 231-232.
- 8. Manoch, L., O. Jeamjitt T. Dethoup, J. Kokaew, A. Eamvijarn, P. Poochinya and Y. Paopun. 2007. Morphological study of some noteworthy fungi from soil and plant. Journal of Microscopy Society of Thailand 21(1): 158-159.
- Paopun, Y., P. Poochinya, P. Umrung and C. Kongpukdee. 2006. Electron microscopic techniques for pollen ornamentation of *Oryza* sativa L. Journal of Microscopy Society of Thailand 20(1): 233-234.
- Rukachaisirikul, V., C. Kaewbumrung, S. Phongpaichi and Z. Hajiwangoh. 2005.
 Eudesmane sesquiterpene from the aquatic fungua *Beltrania rhombica*. Chem. Pharm. Bull. 53(2): 238-240.

- Saparrat, M.C.N., M.N. Cabello and A.M. Arambarri. 2002. Extracellular laccase activity in *Tetraploa aristata*. Biotechnology Letters 24: 1375-1377.
- Saravanan, T. 2004. Studies on the Biodiversity of Microfungi in the Eastern Ghats of Tamilnadu, India. Ph.D. Thesis. University of Madras. India. 201 p.
- Tokumasu, S., Tubaki, K. and Manoch, L. (1997). Microfungal communities on decaying pine needles in Thailand. In:
 Tropical Mycology (eds. K.K. Janardhanan, K.R. Natarajan and D.L. Hawksworth). Science Publishers Inc, USA: 93-106.
- Vijayakumar, E.K.S., K. Roy, S.Chatterjee, S.K. Deshmukh, B.N.Ganguli.,H.W. Fehlhaber and H. Kogler.1996. Arthrichitin, a new cell wall active metabolite from Arthrinium phaeospermum. J. Org. Chem. 61: 6591-6593.

Table 1 Various fallen leaf samples collected from different locations

No	Substrate	Location	Date of	No.	Substrate	Location	Date of
			collection				collection
1	bamboo leaf 1	KU, Bangkok	1 / 6 / 07	8	Java plum leaf	KU, Bangkok	1 / 6 / 07
2	bamboo leaf 2	Angthong	5 / 6 / 07	9	Kaffir lime leaf	Angthong	5 / 6 / 07
3	bamboo leaf 3	Saraburi	14 / 6 / 07	10	Pra du leaf	Angthong	5 / 6 / 07
4	jack fruit leaf	Angthong	5 / 6 / 07	11	bamboo leaf sheath	Saraburi	14 / 6 / 07
5	rose-apple leaf	Bangsue, Bangkok	5 / 6 / 07	12	lan thom leaf	KU, Bangkok	1 / 6 / 07
6	star-gooseberry	Angthong	5 / 6 / 07	13	unidentified plant	Nakhon Si	19 / 10 / 07
7	banana leaf	Saraburi	14 / 6 / 07			Thammarat	

bamboo *Bambusa* sp., banana *Musa sapientum* Pra du *Pterocarpus indicus* jack fruit Artocarpus heterophyllus, Kaffir lime (ma-krut) Citrus hystrix rose apple Eugenia malaccensis, lan thom *Plumeria acuminata*, star gooseberry *Phyllanthus distichus*, Java plum (wha) *Syzygium cumini*

Table 2 Leaf litter fungi isolated from various fallen leaves at different locations

No.	Fungal species	Substrate	No.	Fungal species	Substrate
110.				υ 1	
1	Arthrinium phaeospermum	bamboo leaf 1	16	Lophodermium sp.*	unidentified plant
2	Bipolaris maydis	bamboo leaf 2	17	Memnoniella echinata	Pra du leaf
3	Beltrania rhombica	jack fruit leaf	18	Myrothecium verrucaria	bamboo leaf 3
4	Chaetospermum camelliae	rose apple leaf	19	Nigrospora sphaerica	bamboo leaf 2
5	Cladosporium cladosporioides	jack fruit leaf	20	Periconia digitata	bamboo leaf 3
6	Colletotrichum capsici	star gooseberry	21	Pestalotiopsis guepinii	Java plum leaf
7	Corynespora sp.	banana leaf	22	Pithomyces sp.	bamboo leaf sheath
8	Curvularia eragrostidis	bamboo leaf 1	23	Pseudorobillarda sp.	jack fruit leaf
9	Cylindrocladium sp.	Java plum leaf	24	Stachybotrys nephrospora	lan thom leaf
10	Ellisiopsis gallesiae *	jack fruit leaf	25	Stachybotrys kampalensis	lan thom leaf
11	Fusarium semitectum	Kaffir lime leaf	26	Tetraploa aristata *	bamboo leaf sheath
12	Gilmaniella humicola	bamboo leaf 3	27	Torula herbarum	banana leaf
13	Gyrothrix sp.	bamboo leaf 2	28	Volutella concentrica	bamboo leaf 1
14	Helicomyces sp.*	unidentified plant	29	Wiesneriomyces javanicus	banana leaf
15	Humicola grisea	bamboo leaf 2			

^{*} indicated new record for Thailand

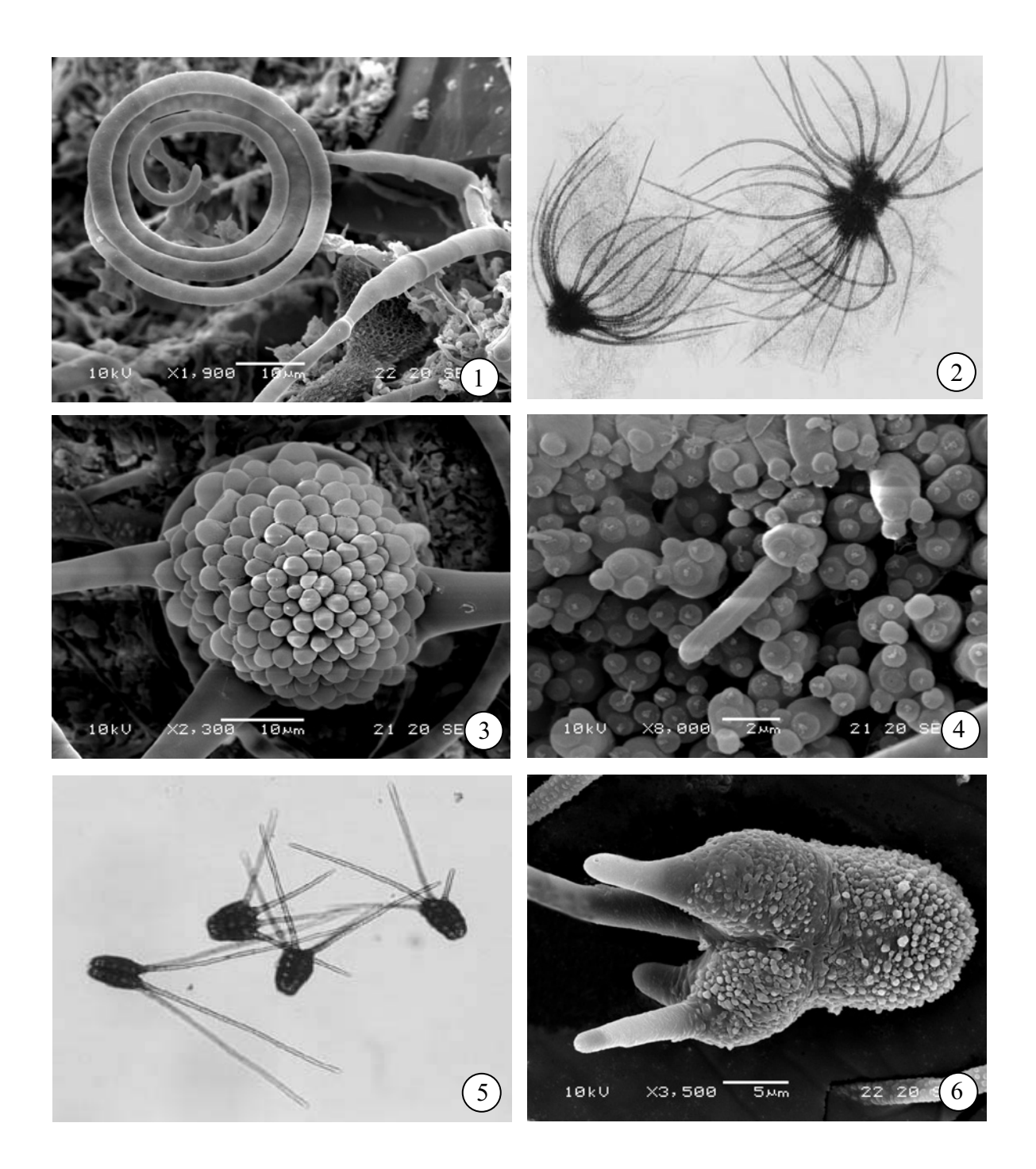


Fig. 1-6 Light and scanning electron microscope photomicrographs of 1. Helicomyces sp. conidiophore and helicoconidium

- 2-4. Wiesneriomyces javanicus conidiophore, conidia and setae
- **5,6.** Tetraploa aristata conidium

Diversity of Arbuscular Mycorrhizal Fungi in Forest Restoration Area of Doi Suthep-Pui National Park, Northern Thailand

Patipan Nandakwang^{1*}, Stephen Elliott² and Saisamorn Lumyong^{2*}

¹Applied Biology Programme, Faculty of Science and Technology, Pibulsongkram Rajabhat University, Phitsanuloke, 65000, Thailand

²Department of Biology, Faculty of Science, Chiang Mai University, Chiang Mai, 50200, Thailand e-mail: patipan263@hotmail.com; scboi009@chiangmai.ac.th

Abstract

Arbuscular Mycorrhizal (AM) fungal diversity was surveyed in the forest restoration area of Doi Suthep-Pui National Park, northern Thailand. Twenty four indigenous tree species, used for forest restoration in a degraded watershed area were examined. Rhizosphere soil samples were collected and AM spores were counted and identified morphologically. AM spores were found in the rhizosphere soils of all tree species. Twenty one AM species were identified: *Acaulospora* (6 species), *Glomus* (12 species) and *Scutellospora* (3 species). AM fungi belonging to the genera *Glomus* and *Acaulospora* were dominant. Abundant species present were *Acaulospora elegans*, *Glomus multicaule* and *Scutellospora pellucida*. These results showed that all 24 indigenous tree species were associated with AM fungi and some AM species had a broad host range.

Background

The tropical forests of Doi Suthep-Pui National Park are one of the most important watershed areas which composed of a number of indigenous tree species. Deforestation within the national park has had adverse consequences on biodiversity and environmental quality. One method of forest restoration, which involves planting mixtures of several indigenous tree species, has been used to counteract this problem (Goosem and Tucker, 1995; FORRU, 2006). Many indigenous species were selected and tested in the experimental plot, established in the north of national park (Elliott et al., 2003). AM fungi are one of the beneficial soil microorganisms that play a crucial role in the mineral nutrition of forest trees (Koide and Mosse, 2004). Information on the capacity of indigenous tree species in association with AM fungi is very important to forest restoration. The purpose of this study was to obtain information on the diversity of AM fungi associated with indigenous tree species in the forest restoration plot.

Materials and Methods

Among the planted tree species in forest restoration plot, 24 potential indigenous species were selected for study. All tree species are reported to be multipurpose and suitable for acceleration of the forest regeneration. Rhizosphere soil samples (about 500 g) of each indigenous species were collected and stored at 4°C until analyzed. AM spores were extracted from 100 g air-dried soil samples by wet-sieving and 50% sucrose centrifugation (Brundrett *et al.*, 1996). Spores were recovered by filtering through a 53 μm sieve onto filter paper. The intact spores on filter

paper were counted under a stereomicroscope (Olympus SZ40). Spores were mounted on microscopic slides in polyvinyl lactic acid (PVA), with or without Melzer's reagent (Morton, 1988) and identified according to morphological characteristics of the originally published species descriptions under a light microscope (Olympus CH30). Light microscopic photographs were taken under an Olympus BX61.

Results and Discussion

The results of our study on the AM fungal diversity in the forest restoration area of Doi Suthep-Pui National Park showed that all 24 indigenous tree species are associated with AM fungi. Spores of AM fungi were found in the rhizosphere soils of all individual tree species. This reflects the mycotrophic nature of the plant species studied and the ability of AM fungi in soils to associate a wide range of host species. It has been reported that many tree species are highly associated with AM fungi (Janos, 1980; Onguene and Kuyper, 2001). Twenty one AM species were identified based on morphological characteristics of their spores according to published descriptions (Table 1). The diversity of AM species was varied among the different tree species (Table 2). Most of the isolated species belonged to the family Glomaceae, all of which were Glomus (12 species, 49.3%). Abundant species present was G. multicaule (14.2%) (figure 1). Six species were in the family Acaulosporaceae, all of which were in the genus Acaulospora (43.6%). Abundant species present was A. elegans (39.2%) (figure 2). Three species were members of

Gigasporaceae and belonged to the genus Scutellospora (7.1%). Abundant species present was S. pellucida (5.5%) (figure 3). Species in the genera Archaeospora, Paraglomus, Entrophospora and Gigaspora were not found. AM fungi belonged to the genera Glomus and Acaulospora were dominant. This fact must be related to their sporogenous characteristics, i.e. Glomus and Acaulospora species usually take a short time to produce small spores, compared with the large spores of Gigaspora and Scutellospora species in the same environment (Hepper, 1984; Bever et al., 1996). A. elegans, G. multicaule and S. pellucida were the most commonly encountered species. This suggests that these species have a widespread and broad host range.

Conclusion

In the forest restoration area of Doi Suthep-Pui National Park, all surveyed indigenous tree species were associated with AM fungi. The AM fungal diversity in the plant rhizospheres was variable among the different tree species. Twenty one AM species were identified as 3 genera and 12 species of *Glomus*, 6 species of *Acaulospora* and 3 species of *Scutellospora*. *Glomus* and *Acaulospora* were the dominant genera. The present study obtains the information on the AM association of 24 potential indigenous trees used to restore tropical forest of Doi Suthep-Pui National Park.

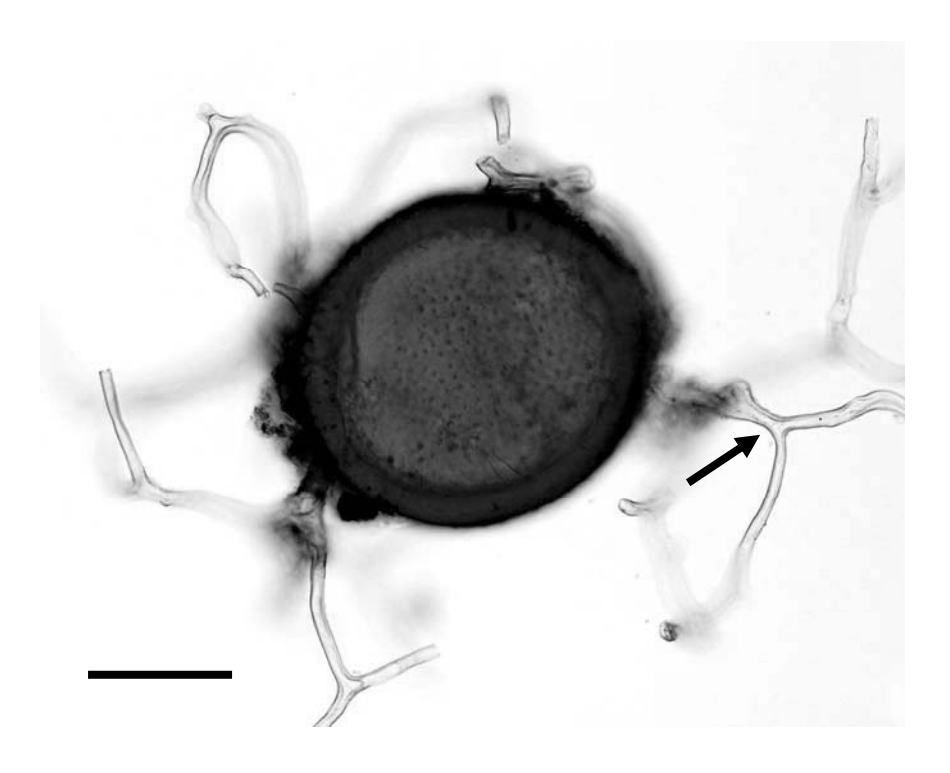
Acknowledgment

This research was partially supported by Pibulsongkram Rajabhat University. We thank Mr. Cherdsak Kuarak and volunteers for helping collect the samples.

References

1. Bever JD, Morton JB, Antonovics J, Schultz PA. Host-dependent sporulation and species diversity of arbuscular mycorrhizal fungi in a mown grassland. *J. Ecol* 1996, 84: 71-82.

- Brundrett M, Bougher N, Dell B, Grove T, Malajczuk N. Working with Mycorrhizas in Forestry and Agriculture. ACIAR Monograph 32, ACIAR, Canberra, Australia 1996, pp: 374.
- 3. Elliott S, Navakitbumrung P, Kuarak C, Zangkum S, Anusarnsunthorn V, Blakesley D. Selecting framework tree species for restoring seasonally dry tropical forests in northern Thailand based on field performance. *For. Ecol. Manage* 2003, 184: 177-191.
- 4. FORRU. How to Plant a Forest: The Principles and Practice of Restoring Tropical Forests. Forest Restoration Research Unit. 1st Edn., Biology Department, Science Faculty, Chiang Mai University, Thailand 2006, pp: 200
- 5. Goosem SP, Tucker NIJ. Repairing the Rainforest-Theory and Practice of Rainforest Re-establishment in North Queensland's Wet Tropics. *Wet Tropics Management Authority, Cairns* 1995, pp. 71.
- Hepper CM. Isolation and Culture of VA Mycorhizal (VAM) Fungi. In: VA Mycorrhizae. Powell, C.L. and D.J. Bagyaraj (Eds.), CRC Press, Florida, USA 1984, pp: 95-112.
- 7. Janos DP. Vesicular arbuscular mycorrhizae affect lowland tropical rain forest plant growth. *Ecology* 1980, 61: 151-162.
- 8. Koide RT, Mosse B. A history of research on arbuscular mycorrhiza. *Mycorrhiza* 2004, 14: 145-163.
- 9. Morton JB. Taxonomy of VA mycorrhizal fungi: Classification, nomenclature, and identification. *Mycotaxon* 1988, 37: 267-324.
- Onguene NA, Kuyper TW. Mycorrhizal associations in the rain forest of South Cameroon. For. Ecol. Manage 2001, 140: 277-287.



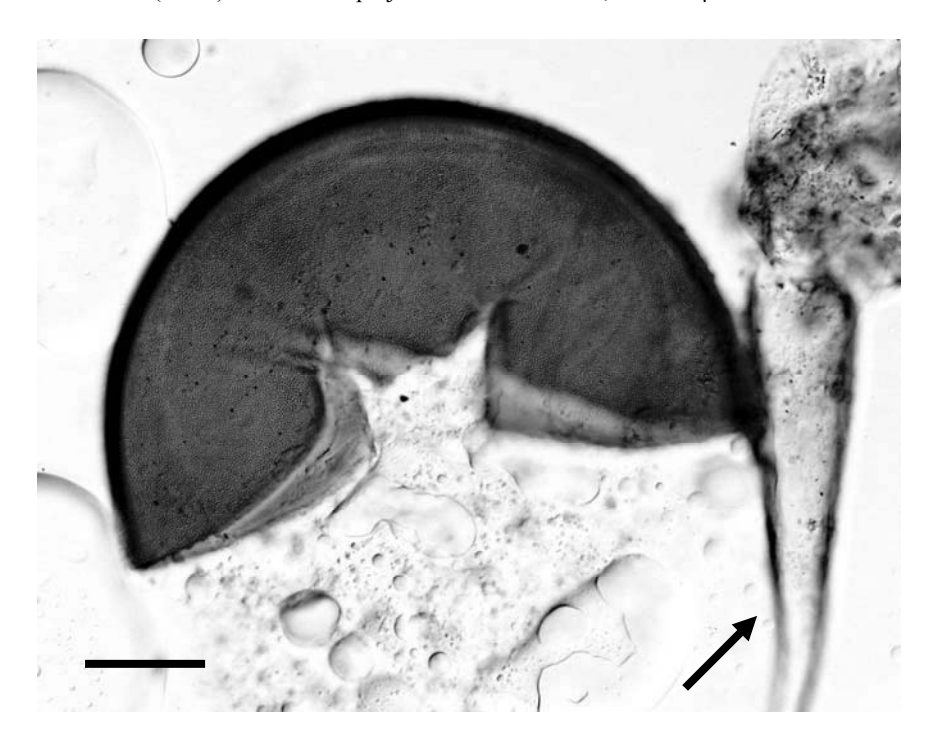


Fig. 2 Acaulospora elegans: Craked spore with sporiferous saccule (arrow) and crowded spines on the surface, bar = $50 \mu m$.

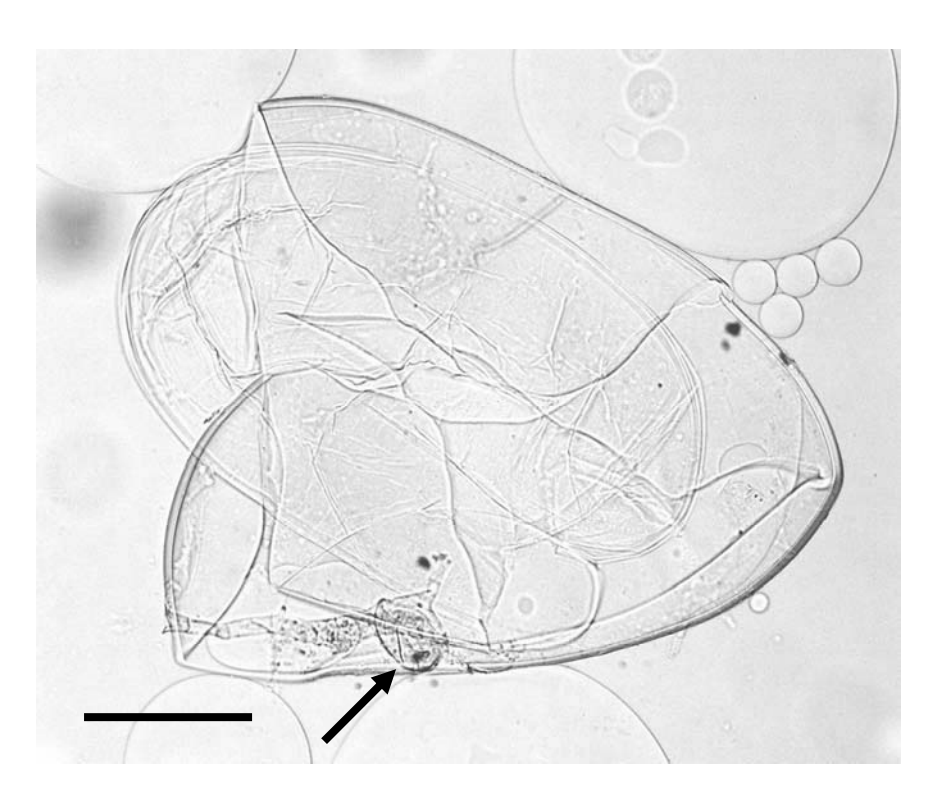


Fig. 3 Scutellospora pellucida: Cracked hyaline spore with hyaline bulbous subtending hypha, bar = $50~\mu m$.

Table 1 Diversity of AM fungi from the rhizosphere soils of 24 indigenous tree species in the forest restoration area of Doi Suthep-Pui National Park, northern Thailand.

Code of AM species	Genus	Species
	Acaulospo	ora -
1	•	A. bireticulata Rothwell & Trappe
2		A. elegans Trappe & Gerd.
3		A. foveata Trappe & Janos
4		A. laevis Gerd. & Trappe
5	2	A. mellea Spain & Schenck
6	2	A. scrobiculata Trappe
	Glomus	
7		G. aggregatum Schenck & Smith
8		G. ambisporum Smith & Schenck
9		G. clavisporum Trappe
10		G. coremioides Berk. & Broome
11		G. intraradices Schenck & Smith
12		G. microaggregatum Koske, Gemma & Olexia
13		G. microcarpus Iqbal & Bushra
14		G. mosseae (Nicol. & Gerd.) Gerd. & Trappe
15		G. multicaule Gerd. & Bakshi
16		G. rubiforme Gerd. & Trappe
17		G. sinuosum Gerd. & Bakshi
18		G. viscosum Nicol.
	Scutellosp	ora
19	_	S. gregaria (Schenck & Nicol.) Walker & Sanders
20	,	S. heterogama Walker & Sanders
21	Ä	S. pellucida (Nicol. & Schenck) Walker & Sanders

Table 2 Diversity of AM fungi found in the rhizospheres of 24 indigenous tree species in the forest restoration area of Doi Suthep-Pui National Park, northern Thailand.

Indigenous tree species	AM species*	
Acrocarpus fraxinifolius Wight ex Arn. (Caesalpinioideae)	3, 4, 14, 15	
Balakata baccata (Roxb.) Ess. (Euphorbiaceae)	12, 20	
Castanopsis acuminatissima (Bl.) A. DC. (Fagaceae)	1, 15	
Erythrina subumbrans (Hassk.) Merr. (Papilionoideae)	2, 7, 12, 19	
Ficus altissima Bl. (Moraceae)	2, 6, 10	
Ficus benjamina L. var. benjamina (Moraceae)	6, 19, 20	
Ficus glaberrima Bl. var. glaberrima (Moraceae)	16	
Ficus hispida L. f. var. hispida (Moraceae)	2, 5, 16, 17	
Ficus racemosa L. var. racemosa (Moraceae)	2, 8, 14, 16, 18	
Ficus subulata Bl. var. subulata (Moraceae)	2, 14, 16, 20	
Glochidion kerrii Craib (Euphorbiaceae)	21	
Gmelina arborea Roxb. (Verbenaceae)	2, 6, 13, 15	
Heynea trijuga Roxb. ex Sims (Meliaceae)	2, 3, 8, 10, 20	
Hovenia dulcis Thunb. (Rhamnaceae)	2, 7, 15	
Macaranga denticulata (Bl.) MA. (Euphorbiaceae)	9, 10, 16, 20	
Machilus bombycina King ex Hk.f. (Lauraceae)	2, 10, 16, 20	
Melia toosendan Sieb. and Zuc. (Meliaceae)	2, 9, 20	
Michelia baillonii Pierre (Magnoliaceae)	16, 17	
Nyssa javanica (Bl.) Wang. (Nyssaceae)	6, 15, 20	
Prunus cerasoides D. Don (Rosaceae)	7, 10, 13, 15, 16	
Rhus rhetsoides Craib (Anacardiaceae)	2, 6, 13, 16	
Sapindus rarak DC. (Sapindaceae)	2, 20	
Sarcosperma arboreum Bth. (Sapotaceae)	10, 11, 20	
Spondias axillaris Roxb. (Anacardiaceae)	15	

 $^{^{*}}$ Numbers in column refer to the codes of AM species in Table 1.

Some Hematological Values and Ultrastructure of Blood Cells in *Piper sarmentosum* Roxb. and *Tinospora crispa* Miers ex Hook. F & Thoms. Treated Diabetic Rats

Areeya Suchantabud^{1*}, Chusri Talubmook^{1,2}, Sanong Chomko¹, Nual-anong Narkkong³

¹ Department of Biology, Faculty of Science, Mahasarakham University,

Maha Sarakham 44150, Thailand

² Faculty of Environment and Resource Studies, Mahasarakham University, Maha Sarakham 44150, Thailand

³ Central Instrumentation Unit, Faculty of Science, Mahasarakham University,

Maha Sarakham 44150, Thailand

e-mail: areeya30@hotmail.com

Abstract

The present study was carried out to investigate the effects of the powder from *Piper sarmentosum* Roxb. leaves and *Tinospora crispa* Miers ex Hook. F & Thoms. stems on packed cell volume, hemoglobin concentration, red and white blood cell counts and ultrastructure of blood cells in streptozotocin-induced diabetic rats. The experiments were performed by daily oral administration of the powder the from *P. sarmentosum* and *T. crispa* at a dosage of 250 mg/kg to diabetic rats for eight weeks. The results showed that the packed cell volume, hemoglobin concentration and red and white blood cell counts in diabetic rats received the powder from *P. sarmentosum* and *T. crispa* were not different, but the hemoglobin concentration and red blood cell count were significantly higher than control. However, the white blood cell count was significantly less than controls. Furthermore, the length of the red blood cells in rats treated with the powder from *T. crispa* was longer than those treated with *P. sarmentosum*. However, they were not different from controls. In contrast, the width of the red blood cells in rats treated with *P. sarmentosum* and *T. crispa* were not different and were not different from controls.

The findings indicated that long-term administration of the powder from these plants changed some hematological values in diabetic rats compared with controls.

Background

Diabetes mellitus is a common metabolic disorder. It is often associated with several complications, such as cataract and retinopathy, gastrointestinal diseases with a high recurrence of pancreatitis, neuropathy, nephropathy, myocardial, and dermatitis, as well as various infectious diseases, both in human and in veterinary medicine. Hematological complications consist mainly of abnormalities in the function, morphology and metabolism of erythrocytes, leukocytes and platelets [1]. By the year 2025, the World Health Organization (WHO) predicts that 300 million people will have diabetes mellitus. Treatment of diabetes mellitus and its complications in the recent context have focused on the usage of plant extracts [2]. Piper sarmentosum Roxb. (Piperaceae, Thai name: Chaplu) The leaves of P. sarmentosum are used as food and traditional medicine in Thailand [3]. Tinospora crispa Miers ex Hook. F & Thoms. (Menispermaceae, Thai name: Boraphet), a plant used to treat diabetics, was able to reduce blood glucose level in moderately diabetic rats, and the hypoglycaemic effect was probably due to its

insulinotropic activity [4]. The effects of P. sarmentosum and T. crispa on hematological values and ultrastructure of blood cells have not yet been reported. Therefore, the purpose of the present study was conducted to examine some hematological values and ultrastructure of blood cells in diabetic rats treated with P. sarmentosum and T. crispa.

Materials and Methods

Extract Preparation

Fresh *P. sarmentosum* leaves and *T. crispa* stems were collected locally, Botanical identification was performed by Dr. Sanong Chomko in Department of Biology, Faculty of Science, Mahasarakham University. The plants were sliced into small pieces, air dried at ambient temperature and ground into powder form.

Animals

Thirty male albino Wistar rats weighting 200-250 g purchased from the Animal Center at Mahidol University in Nakhon-pathom were using in this study. They were acclimatized and housed in an air conditioned room at 22-28 °C for five days. The were fed with standard chow and watered ad libitum prior to the commencing experiments. The rats used in the present study were maintained in accordance with the guidelines of the Committee on Care and Use of Laboratory Animal Resource, National Research Council Thailand. The experiments performed on the rats were conducted in accordance with the advice of the Institutional Animal Care and Use Committee MSU.

Diabetes Induction

The rats were injected intraperitonealy with a single dose of 65 mg/kg streptozotocin (STZ, Sigma Chemicals, St. Louis, MO) freshly dissolved in 20 mM citrate buffer (pH 4.5). After STZ injection, they were provided with a 2% sucrose solution as their drink for 48 hours to alleviate the severity after initial hypoglycaemic phase. Blood glucose levels were assessed 48 hours after STZ injection to confirm the diabetic stage. Only rats with blood glucose at or above 200 mg/dl were used in the experimentation [5].

Experimental Design

The experiment consisted of 5 groups (6 rats per group); Group 1: Control given 2 ml distilled water, Group 2: Streptozotocin induced diabetic given 2 ml distilled water, Group 3: Diabetic rats treated with 0.25 mg/kg glibenclamide, Group 4: Diabetic rats treated with 250 mg/kg of *P. sarmentosum* powder and Group 5: Diabetic rats treated with 250 mg/kg of *T. crispa* powder.

The rats were treated once daily for eight weeks. At the end of the experiment the rats were anesthetized with ether and blood samples were drawn from the tail vein of each animal to determine the hematological values and ultrastructure of blood cells.

Hematological Values

The packed cell volume was determined by microhematocrit centrifugation, centrifuged at 1,500 rpm for 5 min. Hemoglobin concentration was measured using Sahli method. Total red blood cells and white blood cells were counted manually using hematocytometer. Red blood cells were diluted using Gower's solution but total white blood cells using Turk's solution [6].

Ultrastructure of Blood Cells

Ultrastructure of blood cells were studied using Transmission Electron Microscope (TEM). For TEM technique, blood samples were centrifuged in capillary tubes at 1,500 rpm for 15 min. Buffy coats were dropped in 2.5% glutaraldehyde in 0.1 M phosphate buffer, pH 7.2 overnight at 4 °C and then washed in the same buffer. They were postfixed with 1% osmium tetroxide for 2 h, rinsed by distilled water, dehydrated in 20%, 40%, 60%, 80%, 100% and 100% acetone and embedded in Epon resin. Lead citrate and uranyl acetate stained ultrathin sections on copper grid were examined with TEM (JEM 1230) [7].

Statistical Analysis

The results of hematological values were presented as the mean \pm standard error of the mean (SEM). Comparions were made between control and treatment groups using one-way analysis of variance (ANOVA) followed by Duncan's New Multiple Range Test. Values of p < 0.05 were regarded as statistical significant.

Results and Discussion

The results of hematological values as well as the the length and the width of red blood cells of rats in control and treatment groups are given in Table 1 and 2, respectively.

Table 1 showed that the packed cell volume from all experimental groups were not different. The hemoglobin concentration from diabetic rats treated with P. sarmentosum and T. crispa were not different and were not different from rats treated with glibenclamide but were significantly (p < 0.05) more than controls and diabetic controls. The red and white blood cell counts of rats treated with both types of the plant powders were not different but were significantly (p < 0.05) different from controls. However, the red blood cells count of the rats treated with plant powder was significantly greater than that in controls (p < 0.05), while the white blood cells count was significantly less than that in controls (p < 0.05).

Table 2 the length of the red blood cells from T. crispa treated rats was significantly (p < 0.05) longer than that from P. sarmentosum treated rats but it was similar to those from controls, diabetic controls and diabetic rats treated with glibenclamide. The width of red blood cells from P. sarmentosum treated rats was not different from controls, diabetic rats treated with glibenclamide and diabetic rats treated with T. crispa, but was significantly (p < 0.05) less than that from diabetic controls.

These results showed the hematological effect of powder from *P. sarmentosum* and *T. crispa* in diabetic rats. However, compare of hematological

values treated with extract from *Morus alba* in diabetic rats; Packed cell volume 47.17±1.02 %, Hemoglobin concentration 21.80±0.20 g/dl and RBCs 7.48±0.64 x10⁶cell/μl [6] were lower than rats treated with *P. sarmentosum* and *T. crispa*. Hemoglobin is a major constituent of erythrocytes which function in oxygen transport and can therefore be used to evaluate the physical condition of an animal [8]. In addition, male albino rats treated with 50 mg/kg *Teucrium polium* extract; RBCs 6.23±0.82 x10⁶/mm³, WBCs 15.35±3.50 x10³/mm³ and HCT 37.52±2.68 % [9].

TEM micrographs showed that the ultrastructure of red blood cells from the diabetic controls was clearly different from the controls (figure 1). The hemoglobin protein contents in the red blood cells of control rat were homogenous (figure 1 A-B), but the aggregation of hemoglobin was clearly found in the red blood cells of the diabetic controls shown by the electron loose and electron dense area (figure 2 A-B). The ultrastructure of red blood cells from glibenclamide treated *P. sarmentosum* treated were similar to control than *T. crispa* treated rats rats (figure 1 A-B, 3 A-B, 4 A-B, 5 A-B).

The ultrastructure of leukocyte i.e. lymphocyte, monocyte, neutrophil and eosinophil of all rat group were not different (figure 2).

Conclusion

In conclusion, the packed cell volume, hemoglobin concentration, red and white blood cell counts in diabetic rats received the powder from P. sarmentosum leaves and T. crispa stems were not different. Furthermore, the width but not the length of red blood cells in rats treated with the powder from P. sarmentosum and T. crispa were not different and not different from controls. The ultrastructure of red blood cells in controls and P. sarmentosum and T. crispa treated rats were not different but were different from diabetic controls. Moreover, the ultrastructure of white blood cells in rats treated with P. sarmentosum, T. crispa and glibenclamide and controls were not different. The findings indicated that long-term administration of the powder from two types of the plant changed some hematological values and ultrastructure in diabetic rats compared with controls.

Acknowledgment

The authors would like to thank the Development Research Division, Mahasarakham University, Thailand for partly research financial supports.

- 1. Comazzi, S., Spagnolo, V. and Bonfanti, U. Erythrocyte changes in canine diabetes mellitus: in vitro effects of hyperglycaemia and ketoacidosis. *J. Comp Clin Path.* 2004, 12: 199-205.
- 2. Kamalakkannan, N. and Mainzen, Prince P. S. Rutin improves the antioxidant status in streptozotocin-induced diabetic rat tissues. *J. Mol Cell Biochem.* 2006, 293: 211-219.
- 3. Peungvicha, P., Thirawarapan, S. S., Temsiririrkkul, R., Watanabe, H., Prasain, J. K. and Kadota S.. Hypoglycemic effect of the water extract of *Piper sarmentosum* in rats. *J. Ethnopharmacol.* 1998, 60: 27-32.
- 4. Noor, H. and Ashcroft, S. J. H. Pharmacological characterisation of the antihyperglycaemic properties of *Tinospora crispa* extract. *J. Ethnopharmacol.* 1998, 62: 7-13.
- 5. Talubmook, C., Forrest, A. and Parsons, M. Streptozotocin-induced diabetes modulates presynaptic and postsynaptic function in the rat ileum. *Eur. J. Pharmacol.* 2003, 469: 153-158
- 6. Chomko, S. and Talubmook, C. Effect of leaf extracts from *Morus alba* and *Annona squamosa* on haematological values in diabetic rats. *J. Sci and Technol MSU*. 2007, 26:167-173.
- 7. Ponsen, S., Narkkong, N-A. and Angwanich, W. Morphological and ultrastructural observations on the blood cells of sand lizards (*Leiolepis belliana* Rubritaeniata) mertens 1961. *J. Anim Vet. Adv.* 2007, 6(4): 522-527.
- 8. Chang, G-R., Mao, F. C., Yang, C-C. and Chan, F-T. Hematological profiles of the formosan black bear (*Ursus thibetanus formosanus*). *J. Zool. Studies*. 2006, 45: 93-97.
- 9. Khleifat, K., Shakhanbeh, J. and Tarawneh, K. The chronic effects of *Teucrium polium* on some blood parameters and histopathology of liver and kidney in the rats. *Turk J. Biol.* 2002, 26:65-71.

Table 1 Hematological values of controls, diabetic controls, diabetic rats treated with glibenclamide and diabetic rats treated with P. sarmentosum and T. crispa.

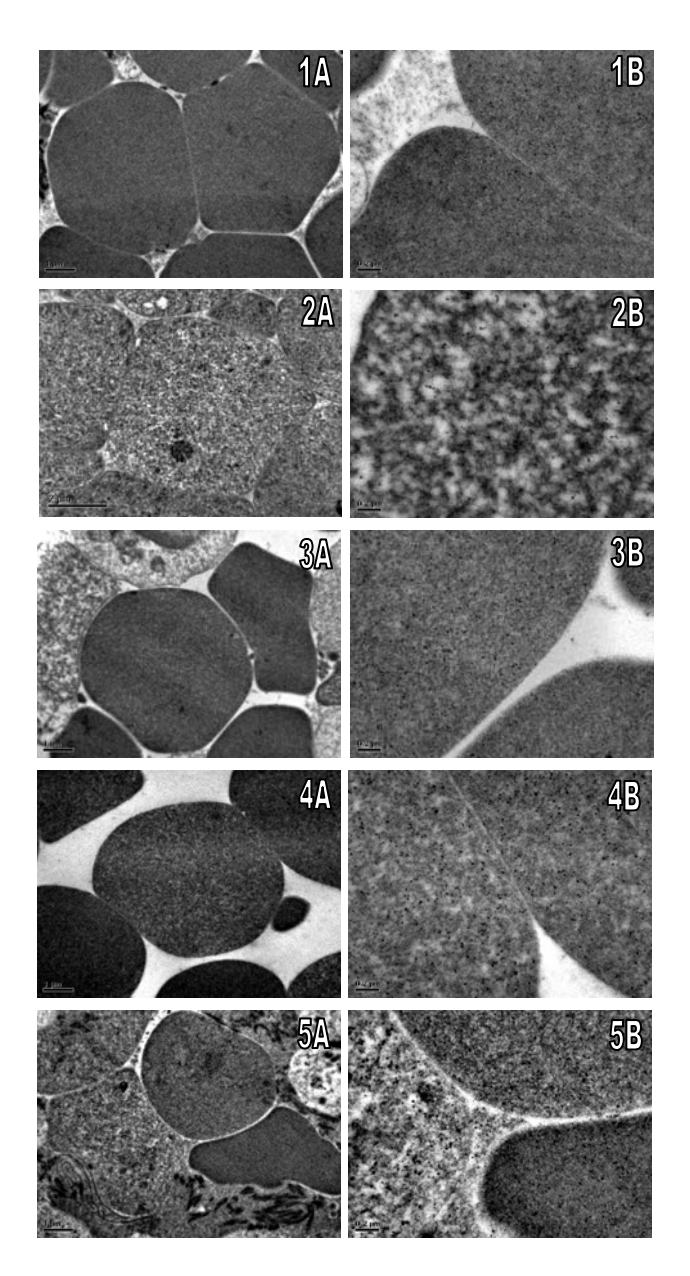
Group	Packed cell volume (%)	Hemoglobin concentration (g/dl)	Red blood cells (x10 ⁶ cell/μl)	White blood cells (x10 ³ cell/μl)
controls	52.00 <u>+</u> 1.37	23.00 ± 0.44^{a}	7.35 <u>+</u> 0.10 bc	9.40 <u>+</u> 0.92 bc
diabetic controls	51.20 <u>+</u> 0.96	23.00 ± 0.94^{a}	5.62 <u>+</u> 0.46 ^a	7.50 <u>+</u> 1.09 ab
glibenclamide	50.40 <u>+</u> 0.40	25.20 <u>+</u> 1.06 ^{ab}	6.97 <u>+</u> 0.18 ^b	10.02 <u>+</u> 0.70 °
P. sarmentosum	50.60 <u>+</u> 0.50	27.00 <u>+</u> 0.31 ^b	8.06 <u>+</u> 0.14 ^{cd}	6.58 <u>+</u> 0.42 ^a
T. crispa	49.60 <u>+</u> 0.24	26.20 <u>+</u> 0.37 ^b	8.82 <u>+</u> 0.25 ^d	5.67 <u>+</u> 0.17 ^a

Means \pm SEM within the same column followed by the different letters are significantly different at p<0.05.

Table 2 Length and width of the red blood cells in controls, diabetic controls, diabetic rats treated with glibenclamide and diabetic rats treated with P. sarmentosum and T. crispa (measured from the thick section).

Group (20 cells/ rat)	Length (µm)	Width (µm)
Controls (n=3)	5.40 ± 0.10^{ab}	4.52+0.11 ^a
diabetic controls (n=3)	5.62 <u>+</u> 0.10 ^b	$4.92 + 0.08^{b}$
Glibenclamide (n=3)	5.57 <u>+</u> 0.11 ^b	$4.72 + 0.11^{ab}$
P. sarmentosum (n=3)	5.17 <u>+</u> 0.12 ^a	$4.45 + 0.10^{a}$
<i>T. crispa</i> (n=3)	5.52 <u>+</u> 0.11 ^b	4.62+0.13 ^{ab}

Means \pm SEM within the same column followed by the different letters are significantly different at p<0.05.



 $\label{eq:Fig.1} \begin{tabular}{ll} Fig.1 Ultrastructrue of red blood cells wistar rats after 8 weeks; group 1 : controls, group 2 : diabetic controls, group 3 : glibenclamide, group 4 : P. sarmentosum and group 5 : T. crispa A; whole cell at 4,500x, B; high magnification at the same area of A (20,000x) \\ \end{tabular}$

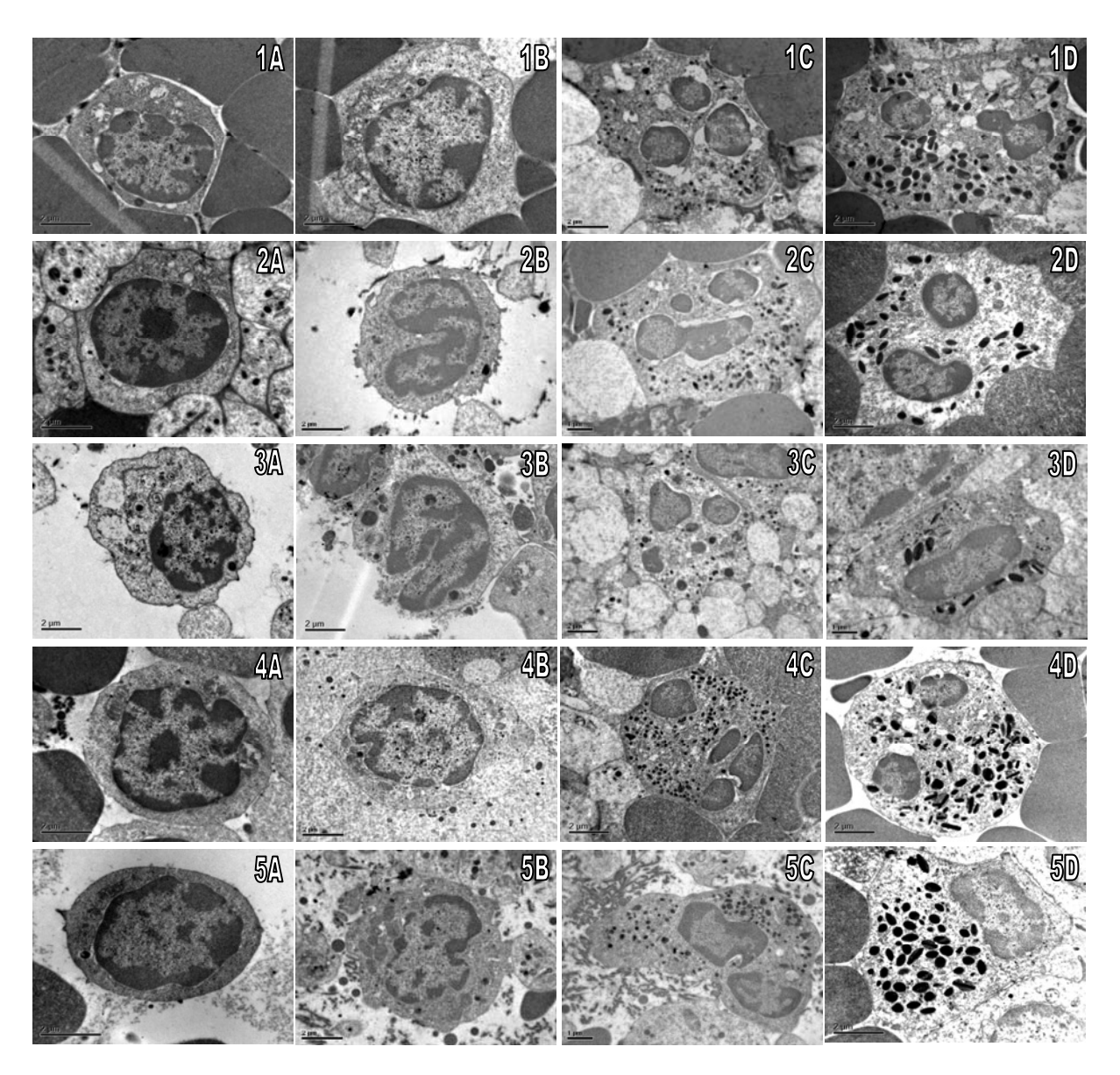


Fig.2 Ultrastructrue of white blood cells of wistar rats after 8 weeks; group 1 : controls; group 2 : diabetic controls; group 3 : glibenclamide; group 4 : P. sarmentosum and group 5 : T. crispa including A : lymphocyte, B : monocyte, C : neutrophil and D : eosinophil.

Hematological Values and Morphological Observation of Blood Cells in Balloon Frog, *Glyphogloossus molossus*

Siripan Ponsen¹, Nual-anong Narkkong², Supaporn Pamok¹, Kunyarut Sappaso² and Worapol Aengwanich¹ Stress and Oxidative Stress Research Unit, Faculty of Veterinary Medicine and Animal

Science Mahasarakham University, Maha Sarakham 44000, Thailand

² Central Instrumentation Unit, Faculty of Science, Mahasarakham University, Maha Sarakham 44150, Thailand

e-mail: siri.pan.p@hotmail.com

Abstract

Eighteen balloon frogs, *Glyphogloossus molossus* were collected from forest and rice field in Maha Sarakham Province, northeastern Thailand during March-May, 2007. Hematological values, morphological structures and blood cell sizes were determined under light and electron microscope examination. The mean of packed cell volume, hemoglobin concentration, total red blood cells, total white blood cells, mean corpuscular volume, mean corpuscular hemoglobin, mean corpuscular hemoglobin concentration, percentage of lymphocyte, monocyte, heterophil, eosinophil and basophil of balloon frogs were 26.94 ± 1.42 %, 8.62 ± 0.70 g/dL, $1.04\pm0.18 \times 10^6$ cells/µl, $1.37\pm0.16 \times 10^3$ cells/µl, 409.29 ± 78.17 fL, 142.11 ± 34.18 pg, 32.96 ± 13.15 g/dL, 41.62 ± 3.07 %, 22.77 ± 1.89 %, 26.27 ± 2.25 %, 1.07 ± 0.29 % and 8.27 ± 0.85 %, respectively. Moreover, the mean of erythrocyte length and width, erythrocyte nucleus length and width, diameter of lymphocyte, monocyte, heterophil, eosinophil, basophil, and thrombocyte of balloon frogs were 15.42 ± 1.04 and 11.47 ± 0.82 ; 6.06 ± 0.78 and 4.02 ± 0.45 ; 13.89 ± 3.34 , 8.56 ± 2.74 , 13.76 ± 3.59 , 15.00 ± 7.08 , 6.90 ± 2.03 and 12.29 ± 2.52 micrometers, respectively. Finally, the morphologic features of blood cell characteristics of balloon frogs were similar to those of other species of frogs.

Background

Balloon frogs, Glyphogloossus molossus is an important protein source for people in northeastern part of Thailand which are caught from forest and rice field for making the food. Balloon frogs are classified in kingdom Animalia, phylum Chrodata, class Amphibia, order Anura, family Microhylidae, species Glyphogloossus and genus spp. Glyphogloossus molossus. At beginning of rainy season, Asian painted frogs leave from their holes for breeding and people catch them for making food. At present, the habitats of balloon frogs have been on the decrease. Whereas, data regarding their blood cell characteristics, blood cell sizes and hematological values have not been reported. therefore, the objective of this study was to establish the blood cell characteristics, blood cell dimension and hematological values of balloon frogs. Basic knowledge from this study is important for hematological research, conservation, clinical diagnosis and in-depth study of this frog.

Materials and Methods

Animals: Eighteen balloon frogs were captured from forest and rice field in Maha Sarakharm Province, northeastern part of Thailand during March–May 2007, and then took to Laboratory of Faculty of Veterinary Medicine and Animal

Science, and Central Instrumentation Unit, Faculty of Science, Mahasarakham University.

Hematological techniques: 0.5 milliliter of blood sample were collected from heart using a 1 ml syringe, 26-gauge needle and 1.5 inch of length then placed in microtube with EDTA for determining hematological values. The samples were cooled to approximately 4 °C, using icepacks and transferred to the laboratory within 2 hours after blood collection. Differential white blood cell counts were performed on blood films prepared, fixed in 95% ethyl alcohol for 5 min and then were stained with Giemsa-Wright' stain and then took photos with camera under light microscope. Blood cell dimensions determined by using a stage and ocular micrometer. The packed cell volume (PCV) was determined after the blood had been transferred to microcapillary tubes and centrifuged at 2,500g for 5 min. Total white blood cell counts were determined manually with the improved Neubauer counting chamber after the blood was diluted with Natt and Herrick's solution. Total red blood cell counts were performed by diluting balloon frog blood with Grower's solution and then counted red blood cell in 5 red blood cells square of the improved Neubauer counting chamber (Campbells, 1995). The hemoglobin concentration was determined by the cyanomethemoglobin method (Ritchie et al, 1994).

Scanning electron microscopic (SEM) technique: Blood sample was dropped in 2.5% glataraldehyde in 0.1 M phosphate buffer, pH 7.2 overnight at 4 °C and washed in the same buffer. Samples were postfixed with 1% osmium tetroxide for 2 hours, rinsed with distilled water, dehydrated in 20%, 40%, 60%, 80%, 100%, 100% acetone and left to air dry. Gold coated blood films were examined under a SEM (JSM 6460LV).

Results and Discussion

The hematological values and blood cell sizes of balloon frogs are shown in Tables 1 and 2. Blood cell characteristics of ballon frogs examined under light microscopic and SEM are shown in figures 1 and 2.

Conclusion

Lastly, blood cell characteristics of balloon frogs were similar to Asian painted frog (Ponsen et al, 2007) and those of other species of frogs that reported by Desser (2001) and Wojtaszek and Adamowicz (2003).

Acknowledgment

We would like to thank to the Mahasarakham University Research and Development Unit, Mahasarakham University for support this project.

- Campbell TW. Avian Hematology and Cytology. *Iowa State University Press*, Ames, Iowa 1995.
- 2. Desser, SS. The blood parasites of anurans from Costa Rica with reflections on the taxonomy of their trypanosomes. *J. Parasitol* 2001, 87(1): 152-160.
- Ponsen S, Narkkong N-A, Pamok S, Sappaso K, Aengwanich W. Hematological values and morphological observation of blood cells in Asian painted frogs, Kaloula pulchra 1831. Proceeding in The First International Conference on Sustainable Animal Agriculture and Developing Countries (SAADC 2007) at Yunnan Agricultural 27th-30th University, China, September, 2007, 345-348.
- 4. Ritchie, BW, Harrison G.J, Harrison RL, Avian Medicine: Principle and Application. Wingers Publishing, Inc, Florida 1994.
- 5. Wojtaszek J, Adamowicz A. Haematology of the fire-bellied toad, *Bombina bombina* L. *Comp. Clin. Path* 2003, 12: 129-134.

Table 1. Hematological values (mean \pm SE) of balloon frogs (n=18).

Hematological value	Mean ± SE
PCV(%)	26.94 ± 1.42
HB(g/dL)	8.62 ± 0.70
RBC ($x10^6$ cell/ μ l)	1.04 ± 0.18
$WBC(x10^3 \text{ cell/}\mu\text{l})$	1.37±0.16
MCV (fL)	409.29±78.17
MCH (pg)	142.11±34.18
MCHC (g/dL)	32.96±13.15
Lymphocyte (%)	41.62±3.07
Monocyte (%)	22.77±1.89
Heterophil (%)	26.27±2.25
Eosinophil (%)	1.07 ± 0.29
Basophil (%)	8.27±0.85

PCV=packed cell volume; HB=hemoglobin concentration; RBC=red blood cell; WBC=white blood cell; MCV=mean corpuscular volume; MCH=mean corpuscular hemoglobin; MCHC=mean corpuscular hemoglobin concentration

Table 2. Cell sizes (mean \pm SE) of balloon frogs (n=18).

Blood cell size (µm)	Mean ± SE
Erythrocyte: length	15.42 ± 1.04
: width	11.47 ± 0.82
: nucleus length	6.06 ± 0.78
: nucleus width	4.02 ± 0.45
Lymphocyte	8.56 ± 2.74
Monocyte	13.89 ± 3.34
Heterophil	13.76 ± 3.59
Eosinophil	15.00 ± 7.08
Basophil	6.90 ± 2.03
Thrombocyte	12.29 ± 2.52

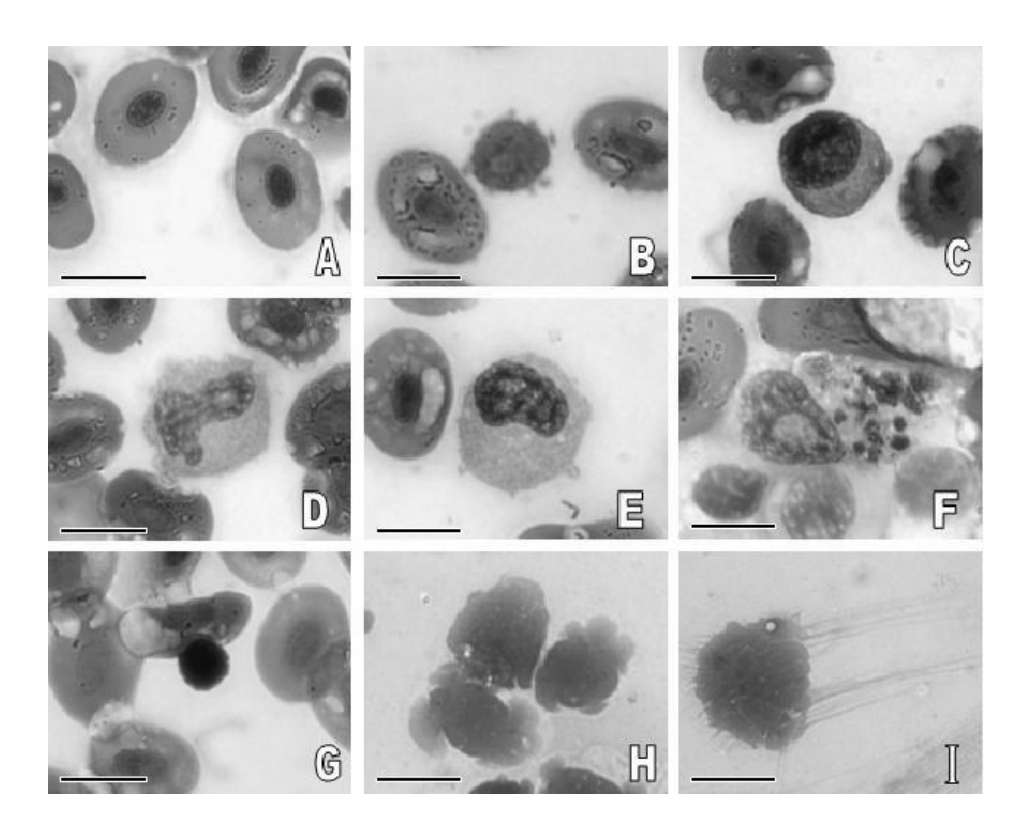


Fig. 1 LM micrographs of balloon frog blood cells (A, Erythrocyte; B, lymphocyte; C, monocyte; D-E, heterophil; F, eosinophil; G, basophil; H-I, thrombocyte; Geimsa-Wright's stain, bar = 10 μ m).

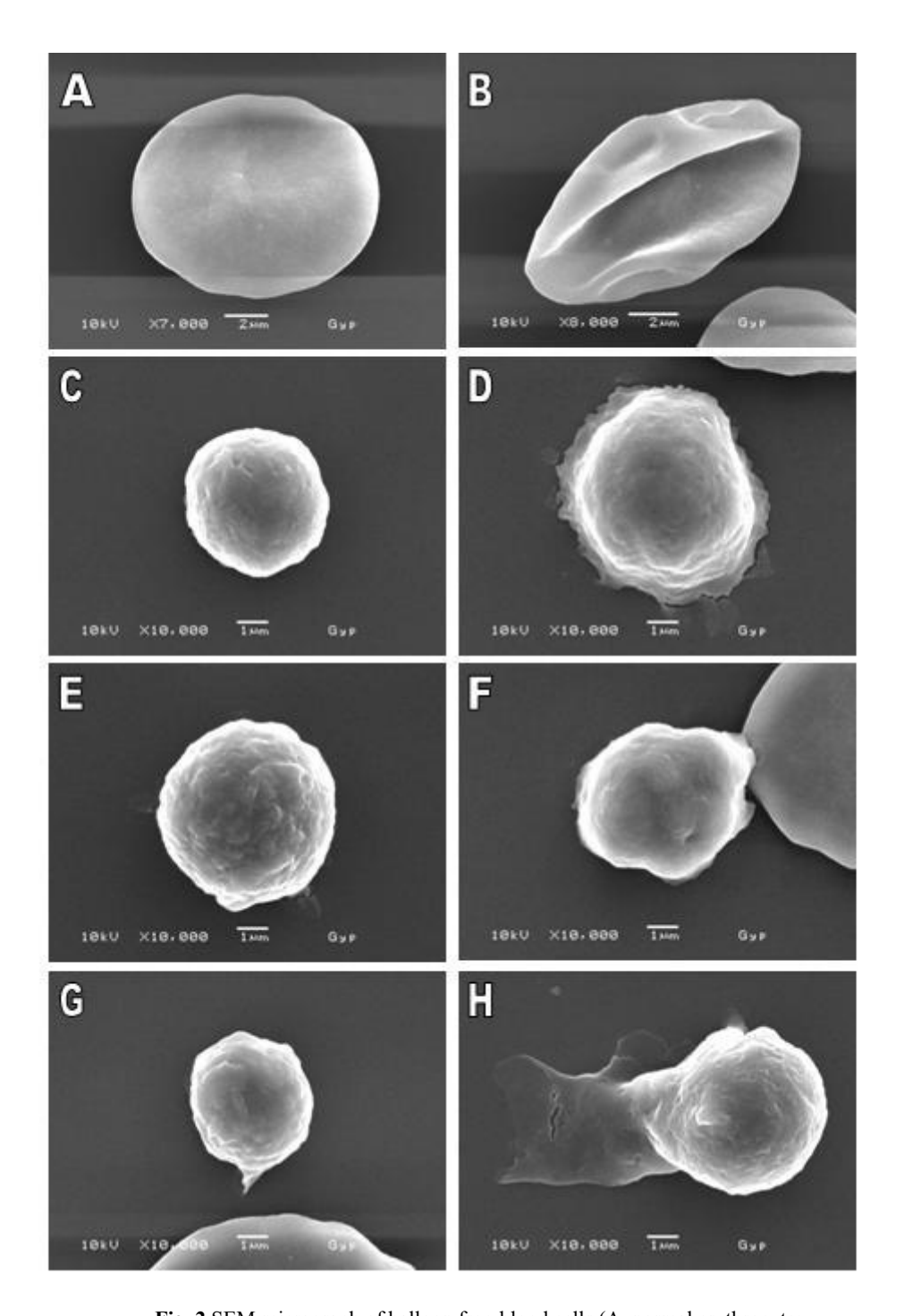


Fig. 2 SEM micrograph of balloon frog blood cells (A, normal erythrocyte; B, abnormal erythrocyte C, lymphocyte; D, monocyte; E, heterophil; F, eosinophil; G, basophil; H, thrombocyte; from A,B bar = 2 μ m and C-H, bar = 1 μ m)

Morphological Changes of Rice Starch during Grain Development

Pachongchit Poochinya 1*, Onanong Naivikul², Yupadee Poapun¹, Patcharee Umrung¹

- Scientific Equipment Center, Kasetsart University Research Development Institute
- ² Faculty of Agro-Industry, Kasetsart University

e-mail: psdpcc@ku.ac.th

Abstract

Microscopic examination of the developing rice grains provides information on morphology and composition, which influences processing behavior of the grains. PathumThani1 rice variety was studied. Maturation period of rice seeds was about 30 days after flowering. Scanning electron microscopy and light microscopy were used to examine development of rice grains in the early broom, milky, dough, yellow ripe, and mature stages. Starch granule size increased during grain development. The size of the granule increased most rapidly during 10-18 days after flowering. Starch was present essentially only in the endosperm cells of mature brown rice, where it existed as compound polyhedral granules 3 to 5 μ m in size. The cluster of starch granules within an amyloplast was spherical to ellipsoidal in shape. Rice starch was very tightly packed in the endosperm cells, and the starch granules had sharp edges.

Background

The rice spikelet consists of a single floret because the spikelet meristem is converted into a floret meristem after producing two pairs of sterile glumes. Rice florets comprise lemma, palea and three kinds of organs: two lodicules (pedals), six stamens and one pistil constituted by a single carpel (Itoh et al., 2005). Flowering in rice includes the opening of the palea and lemma, shedding of pollen by the anthers, and closing of the palea and lemma. The floret remains open for at least 30 min. Generally, florets open in the morning. It takes about 7 days for all spikelets in a panicle to open. Pollination takes place before or as the florets open, and fertilization is completed 30 min after pollination. Rice is essentially selfpollination. After fertilization, the rice caryopsis develops much faster in the longitudinal than in the transverse axis. It attains full length by 4 days after flowering (DAF), maximum width by 14 DAF, and maximum thickness by 21 DAF. The consistency of the endosperm goes through progressive stages, termed milky, dough, yellow, and mature (Juliano, 1985). During grain development, produced from photosynthesis is then transported in the phloem to the developing grains. Starch accumulates in the rice grain during the grainfilling period. Its deposition involves a suite of enzymes and several processes. (Ishimaru et al., 2003; Fitzgerald, 2004).

The aims of this study were to establish the pattern of starch development in the early broom stage, milky, dough, yellow ripe, and mature stages.

Materials and Methods

Sample

Samples of developing rice grains (*Oryza sativa* L., variety Pathum Thani 1) were collected from 4 to 28 days after flowering at 4-day intervals from Chachoengsoa Service Center for Crops and Production Resources, Chachoengsoa Province, Thailand. The grains were cooled to 0 ° C in an ice bath immediately after sampling and were stored at -20 ° C until used for analysis.

Sample Preparation for Electron and Light Microscopic Studies

Early broom and milky stages of rice seeds were cut into halves with a razor blade. Dough and mature stages, rice grains were manually snapped in two parts in the transverse direction. The fractured grain was mounted on aluminum stub using double-sided adhesive tape, with the broken surface oriented upwards. All specimens were stored in desiccator about a week. The specimens later were sputter coated with gold and viewed under a JSM 5600 LV (JEOL, Japan) scanning electron microscope at an accelerating voltages of 10 kV. For light microscopy, the grains were viewed under ZEISS stereoscopic microscope.

Results and Discussion

The developing grains grew very rapidly during the first ten days after flowering. Between 4 and 10 days after flowering the grain was sometimes called 'Water-ripe' or 'Pre-milk'. Milky stage, the grain started to fill with a white, milky liquid. The panicle looked green and started to bend. Dough stage, the milky portion of the grain first

turned into a soft dough and later a hard dough. The grains in the panicle began to change from green to yellow. Mature stage, the individual grain was mature, fully development, hard and had turned yellow (figure 1). Pigments in coloured rices were in the pericarp or the seed coat. The green colour was dued to chloroplasts in the 'cross cell' layer. Starch granules were first noticed in the endosperm cells of the four-day grain. The size of the granule increased most rapidly during the period 10-18 days after flowering. Individual starch granules increased in size from 3 to 5 m during grain development (figure 2).

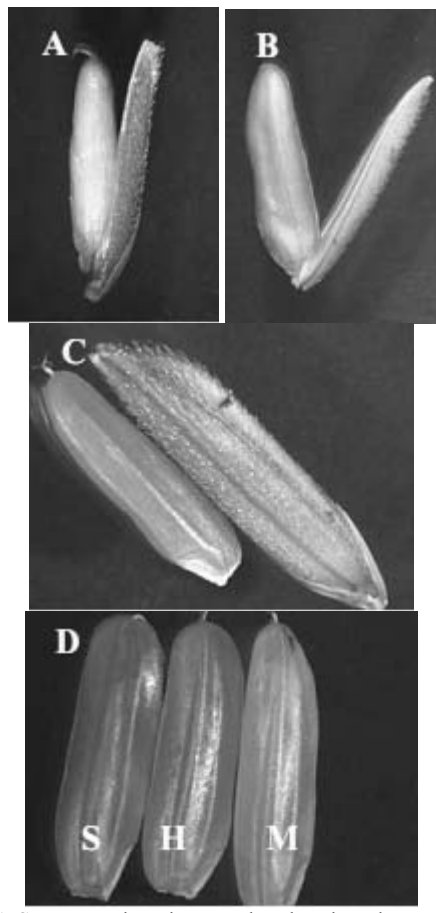


Fig. 1 Stereoscopic micrographs showing the stages of grain development. A: Early broom (4-10 DAF), B: Milky stage (14-15 DAF), C: Soft dough stage (17-18 DAF), D: Soft dough stage, S, (17-18 DAF) Hard dough stage, H, (20-23 DAF) and Mature stage, M, (28-30 DAF).

Mature grain became hardened and translucent as it lost moisture. The starch granules had sharp edges (figure 3).

Conclusion

Starch granules of rice were small, about 3-5 μm in diameter, and each granule was angular. The granules were compound. Each compound starch granule was polyhedral and contained many individual granules. Starch accumulated in the rice grain during the grain-filling period. Its deposition involved a suite of enzymes and several processes. During starch synthesis, sucrose produced from photosynthesis was transported in the phloem to the developing grains. The first process was the acquisition of the precursor sugars. The second process was the synthesis of the amylose and the amylopectin. The third process was the starch granules formation. The fourth process was the compound starch granules formation. The pattern of the developing rice grain in the early broom, milky, dough, yellow ripe, and mature stages were established in series of the starch synthesis. Starch granules size increased during grain development. The size of the granule increased most rapidly during the period 10-18 days after flowering. The cluster of starch granules within an amyloplast is spherical to ellipsoidal in shape. Rice starch was very tightly packed in the endosperm cells and the starch granules had sharp edges.

Acknowledgment

Chachoengsoa Service Center for Crops and Production Resources, Chachoengsoa Province, Thailand, is gratefully thanked for voucher specimen of Pathum Thani 1 rice variety.

- 1. Fitzgerald, M. Rice: Chemistry and Technology Third Edition. *American Association of Cereal Chemists, Inc. St. Paul, Minnesota* 2004, 109-162.
- 2. Ishimaru, T., Matsuda T., Ohsugi R. and Yamagishi T. Morphological development of rice caryopses located at the different positions in a panicle from early to middle stage of grain filling. *Functional Plant Biology* 2003, 30: 1139-1149.
- 3. Itoh, J.I., Nonomura K.I., Ikeda K., Yamaki S., Inukai Y., Yamagishi H., Kitano H. and Nagato Y. Rice plant development: from zygote to spikelet. *Plant Cell Physiology* 2005, 46(1): 23-47.
- 4. Juliano, B.O. and Bechtel D.B. Rice: Chemistry and Technology Second Edition. *American Association of Cereal Chemists, Inc. St. Paul, Minnesota*, 1985, 17-58.

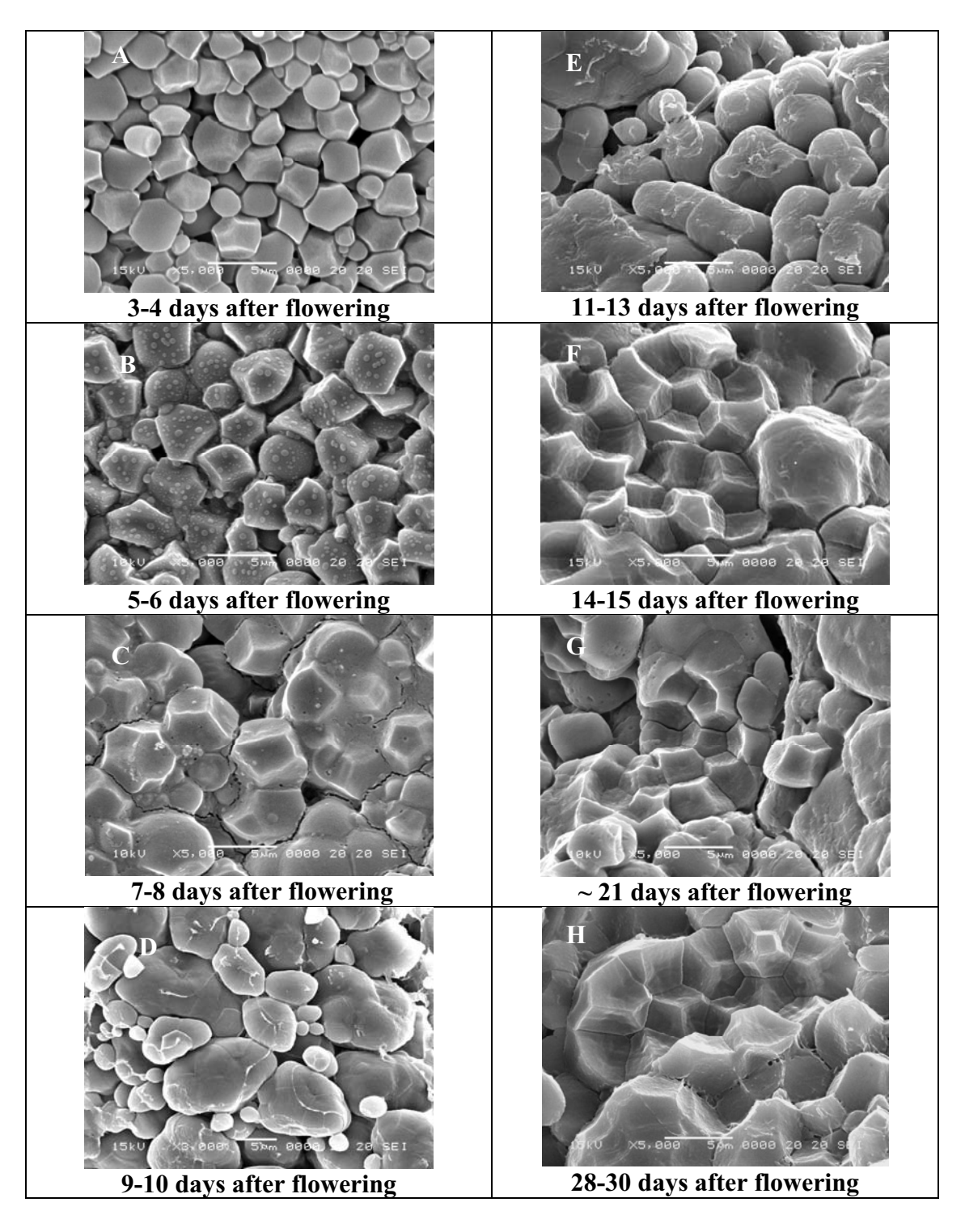


Fig. 2 Scanning electron micrographs of starch granules showing the pattern of starch granule formation from individual starch granule to compound starch granule in the amyloplast.

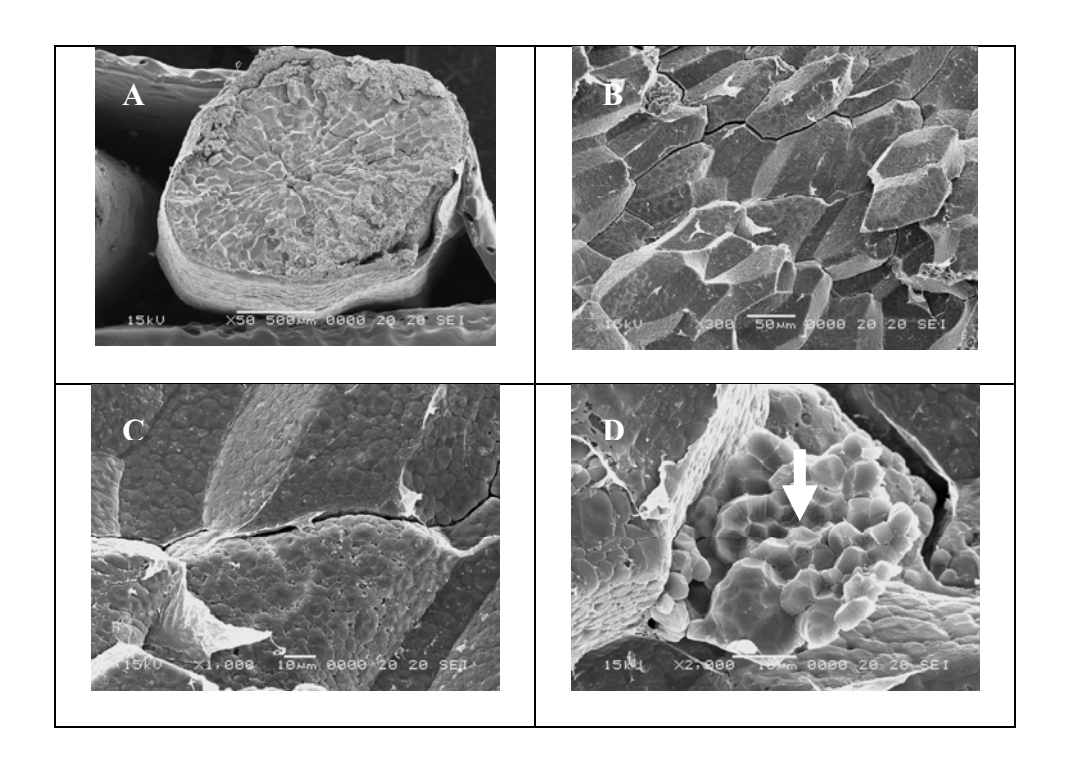


Fig. 3 Entire fracture face of the mature grain showing the starchy endosperm cells elongated radially on cross-sectional view (A) and filled with compound starch granules (B,C). D, the compound amyloplasts broken open, clearly revealing at least 16 single granules (arrows) inside the compound structure.